Title
Development of Ferroic MEMS Devices for Single-Cell Manipulation and Implantable Communications

Author
Estrada, Victor Manuel

Publication Date
2023

Peer reviewed|Thesis/dissertation

UNIVERSITY OF CALIFORNIA

Los Angeles

Development of Ferroic MEMS Devices for Single-Cell Manipulation and Implantable Communications

A dissertation submitted in partial satisfaction of the

requirements for the degree Doctor of Philosophy

in Mechanical Engineering

by

Victor Manuel Estrada

2023

ABSTRACT OF THE DISSERTATION

Development of Ferroic MEMS Devices for Single-Cell Manipulation and Implantable Communications

by

Victor Manuel Estrada

Doctor of Philosophy in Mechanical Engineering

University of California, Los Angeles, 2023

Professor Gregory P. Carman, Chair

This dissertation focuses on the design, fabrication, and testing of two microelectromechanical (MEMS) devices that utilize ferroic materials for applications in biomedical engineering: a magnetic single-cell capture-and-release platform and a 400 MHz multiferroic implantable antenna.

Ferroic materials are a class of materials that exhibit spontaneous polarization, magnetic moment, or mechanical strain. These unique electrical, magnetic, and mechanical properties make them desirable for various applications. For instance, in electronics, ferroic materials are used in various devices such as sensors, actuators, and data storage devices. In recent years, a large amount

of research has been conducted on the miniaturization of ferroic devices due to the benefits of having a small form factor. Miniaturized devices often have improved performance, reduced costs, and increased portability. In the biomedical industry, miniaturization has led to developing smaller and more compact medical devices such as implantable sensors, drug delivery systems, and wearable monitoring devices. These devices are more convenient for patients and provide a more cost-effective and accessible solution to healthcare challenges.

Chapter one of this dissertation introduces the concept of ferroic materials and the mechanism behind their properties. I first present and discuss ferromagnetic materials and the physics behind them. Then I discuss their applications and, more specifically, their application in the biomedical industry. I then briefly cover the physics and applications of ferroelectric and ferroelastic materials. To conclude this chapter, I discuss the emerging field of multiferroic composites and their applications.

The second chapter explores the creation of our platform for capturing and releasing single cells using magnetism. The chapter starts by highlighting the significance of cell sorting and the necessity for effective single-cell capture, and the importance of deterministic single-cell release. Next, a comprehensive examination of existing devices aimed at high-throughput single-cell capture and manipulation is conducted, along with an evaluation of their drawbacks. Our platform is then introduced, outlining its design and how it overcomes the limitations of previous devices. The theoretical validation of each component is also described and performed using finite element and finite difference methods. The microfabrication process used to make our platform is then outlined. Next, I describe how we experimentally verified the platform's capability to magnetize and demagnetize individual capture sites using magnetic force microscopy. I then present the results from our experiments, where we demonstrate the capture and deterministic release of

superparamagnetic beads and then successfully demonstrate the capture of single T-cells and their subsequent individual release.

Chapter three addresses the development of our 400 MHz multiferroic implantable antenna. This chapter begins with a brief introduction to implantable antennas and the challenges they currently face as a technology. I then describe multiferroic antenna technology and its benefits and how it can address the challenges described previously. These benefits include its ability to be miniaturized without compromising efficiency and its compatibility with implantable antennas. Next, I describe our multiferroic antenna design and its operation principle. Given that my work primarily revolved around the microfabrication of this device, the majority of the rest of this chapter revolves around the microfabrication process and the challenges that were faced during the design of this fabrication process. Following this, I show some fabricated devices and discuss the experimental material characterization of the different components of the antennas. In closing, I present the experimental results from the fabricated antennas. In particular, I discuss the S11 reflection coefficient and the S21 transmission coefficient response as they vary with input signal frequency.

Lastly, the dissertation concludes with a summary of both projects discussed, and I outline the potential future work that could be conducted to further improve these devices.

The dissertation of Victor Manuel Estrada is approved.

Kang Lung Wang

Dino Di Carlo

Robert N. Candler

Abdon E. Sepulveda

Gregory P. Carman, Committee Chair

University of California, Los Angeles

2023

To my family and friends to whom I owe everything.

Table of Contents

List of Figures

no discernable poles. (b) Finite Element model of the magnetic field magnitude and direction produced around a current-carrying wire. (i) Field produced around a copper wire using the magnetizing current of 2 amps. It can be observed that on the top surface of the wire, where the capture site would be, the field produced is 490 Oe which is sufficient to magnetize the capture site to saturation. (ii) Field produced around the copper wire using the demagnetization current of -.5 Amps. It can be observed that the field strength at the top surface is -122 Oe which is close to the measured coercivity of the capture site. (c) Microscope image of the capture site with arrows showing the direction of the current pulse and the corresponding magnetic field direction surrounding the wire. (d) Results from the MFM test. (i) Capture site magnetized using a 2-amp current pulse. We can clearly see that the left and right edges of the rectangular capture site are the brightest and darkest areas of the image, which correspond to the magnetic poles of the structure. (ii) Capture site demagnetized using a negative 1-amp current pulse. We can see no discernable magnetic poles, meaning the structure was successfully demagnetized. (iii) Remagnetization of the capture site in the opposite direction. Here we see that the location of the bright and dark areas of the MFM measurement have switched compared to (i) after applying a negative 2-amp current pulse. 56

Figure 2-19 (a) Microscope image showing magnetic beads captured at each captured site in a 3x3 section of the larger 5x5 array. The image on the left shows a group of beads at each magnetized capture site. The inset more clearly shows the beads that are attached to capture site 23. The image on the right shows the results of demagnetizing the capture sites starting from the bottom right to the bottom middle to the bottom left. As can be seen, the beads are completely released and dragged away by the fluid in the channel upon site demagnetization. (b) Time-lapse images of

List of Tables

ACKNOWLEDGEMENTS

As my time as a Ph.D. student comes to an end, I want to acknowledge how fortunate I was to end up at UCLA and to be able to study for a doctoral degree. I want to take this opportunity to thank everyone who played a role in my success at UCLA. I want to first thank Dr. Yitshak Zohar and my colleagues Meagan Tran and Tim Frost at the University of Arizona during my time as an undergraduate. They taught me the basics of scientific research and the hard work required to be successful in a lab. In particular, I want to thank Meagan because, without her, I would not have known about opportunities like the TANMS Research Experience for Undergraduates (REU) summer program, which I attended in the summer of 2017. During that summer program, I worked for eight weeks alongside three other students under Professor Sepulveda on a research project related to modeling a multiferroic device aimed at controlling the position of magnetic beads. This project introduced me to the field of multiferroics and introduced me to many of my future colleagues. In 2018, as my time as an undergraduate student at the University of Arizona drew to a close, I wondered where I wanted to go next. I applied to the Mechanical Engineering graduate program at UCLA, and thankfully I was accepted. However, since I didn't have any funding, it would be impossible for me to go there. Thankfully I gave Maria del Pilar O'Cadiz a call who was the education director of TANMS at the time, and she spoke to Professor Carman; they were able to offer me the TANMS doctoral fellowship, which allowed me to finalize my decision and commit to coming to UCLA for my doctoral degree. Without the help of Pilar, I would have never come to UCLA, she gave me the opportunity to show that I deserved to come to such a prestigious school, and for that, I'll always be grateful.

During my five years at UCLA, I met many people that were essential to my success. First and foremost, I want to thank Professor Abdon Sepulveda for taking a chance on me and taking me on as his student. He believed in me when no one else did, and I'll never be able to repay him for that. I want to also acknowledge my colleague and closest friend during my time at UCLA, Ruoda Zheng. He is one of the smartest and most humble people I have ever met. We collaborated on every project, and we made a great team. With his amazing analytical skills and my experimental skills, we were able to overcome many challenges that others struggled with. We, of course, had our disagreements, but we worked through them all and learned from our mistakes. I also want to thank Professor Greg Carman. As my co-advisor, he offered a lot of great advice over the years. At times we had disagreements related to my research, but I soon learned that all of his criticisms came from a good place. He pushed us because he held us to a high standard, and his advice on research methodology and presentation skills will be something I will keep with me forever. Finally, I want to thank my lab mates Emily, Shreya, John, Malcolm, Michael, Paymon, Adrian, Jesse, and Matthew. Our discussions and collaborations allowed me to learn about many different aspects of physics, material science, and multiferroics. Also, your friendship got me through some of the hardest times during this Ph.D.

I also need to thank those outside of UCLA that supported me during these last five years. I want to thank all of my friends who allowed me to relax and forget about my lab work whenever I was hanging out or talking to them. In particular, I want to thank my friends Sebastian, Cairo, Adolfo, Foxy, and Joe, as well as the whole Big Baller crew. Most importantly of all, I need to thank my father, mother, sister, and grandmother for their patience and support over these last five years. I apologize for not being able to help financially whenever it was needed, but God willing,

that will not happen again. I can never repay all that you provided me, but I hope I can make you proud with this accomplishment.

VITA

Education:

2018-2020 M.S. in Mechanical Engineering

University of California, Los Angeles

2014-2018 B.S. in Mechanical Engineering

The University of Arizona

Employment History:

2018-2023 Graduate Student Researcher

Translational Applications of Nanoscale Multiferroic Systems (TANMS)

2021-2023 Microfabrication Contractor

Efficient Power Conversion Corporation

2020-2021 Microfabrication and Testing Assistant

Forcyte Biotechnologies, Inc

Publications:

*[1] **Victor Estrada**, Ruoda Zheng, Yilian Wang, Hiromi Miwa, Michael Bogumil, Dino Di Carlo, Gregory P. Carman, and Abdon E. Sepulveda. "Arrayed Single Cell Capture and Release using Localized Oersted Fields", submitted to Advanced Healthcare Materials. (2023)

*[2] Ruoda Zheng, **Victor Estrada**, Jin-Zhao Hu, Nishanth Virushabadoss, Rashaunda Henderson, Gregory P. Carman, and Abdon E. Sepulveda. “A Lamb Wave Magnetoelectric Antenna for Implantable Devices”, to be submitted to Appl. Phys. Lett. (2023)

*[3] Maite Goiriena-Goikoetxea, **Victor Estrada**, Zhuyun Xiao, Rachel Steinhardt, Nobumichi Tamura, Rajesh Chopdekar, Alpha T. N'Diaye, Abdon Sepúlveda, Darrell G. Schlom, Rob Candler and Jeffrey Bokor. “Imaging of voltage-controlled switching of magnetization in highly magnetostrictive epitaxial Fe-Ga microstructures on PMN-PT”, submitted to Small. (2023)

[6] Timothy Frost, **Victor Estrada**, Linan Jiang, and Yitshak Zohar. (2019). Convection–diffusion molecular transport in a microfluidic bilayer device with a porous membrane. *Microfluidics and Nanofluidics*, *23*(10).

*First Author or Co-first Author

Presentations:

[1] **Victor Estrada**, Ruoda Zheng, Gregory P. Carman, Abdon E. Sepulveda. “Magnetic Single Cell Capture and Release”, Poster presentation at TANMS Annual Research and Strategy Meeting. (February 2022)

[2] **Victor Estrada**, Ruoda Zheng, Gregory P. Carman, Abdon E. Sepulveda. “Magnetically Activated Cell Capture and Release using Spin-Orbit Torque”, at Conference on Magnetism and Magnetic Materials. (November 2019)

Chapter 1. Introduction

1.1 Ferroic Materials

Ferroics are a class of materials that include ferromagnetic, ferroelectric, and ferroelastic materials. Ferromagnetic materials are those that exhibit spontaneous and switchable magnetization even in the absence of an applied field. Similarly, ferroelectric and ferroelastic materials are those that exhibit spontaneous and switchable electric polarization and spontaneous mechanical deformation, respectively. These unique properties have caused them to garner a lot of attention in the scientific community. They have been used in a variety of applications ranging from microscale sensors and actuators to large medical imaging systems. In the following sections, I will delve into ferromagnetic and ferroelectric materials and their role in biomedical engineering. I will briefly discuss the physical principles behind their properties and how they have been used in the biomedical industry.

1.1.1 Ferromagnetic Materials

Ferromagnetism is a property of certain materials that are characterized by a high magnetic permeability and spontaneous magnetization. Magnetic permeability is a measure of the magnetization of a material given an applied magnetic field. Spontaneous magnetization refers to the ability of the material to be magnetized even under the influence of no applied magnetic field. Examples of such materials include transition metals such as iron, nickel, and cobalt and their alloys, as well as rare earth metal compounds such as neodymium iron boron.

In an attempt to briefly describe the physics of ferromagnetism, I will cover some of the more basic principles that govern these materials. A lot of detail is omitted for the sake of brevity, but this information should be sufficient to understand the concepts in the following chapters.

In ferromagnetic materials, the magnetic dipoles of neighboring atoms tend to align parallel to each other regardless of the direction of the applied external field. This phenomenon is caused by the strong exchange interaction that exists between them[1]. Given the fact that this exchange interaction has a limited spatial range, the atomic magnetic dipoles within a material will arrange themselves into larger magnetic domains, each with a different magnetization direction. These magnetic domains are microscopic areas within which the magnetic moments are aligned parallel to each other. In an unmagnetized or demagnetized ferromagnetic material, these magnetic domains each point in different directions resulting in a material that has negligible net magnetization. This is why, for example, an iron nail will not magnetically attract other iron nails until it is magnetized through the application of an external magnetic field.

I Magnetic Hysteresis

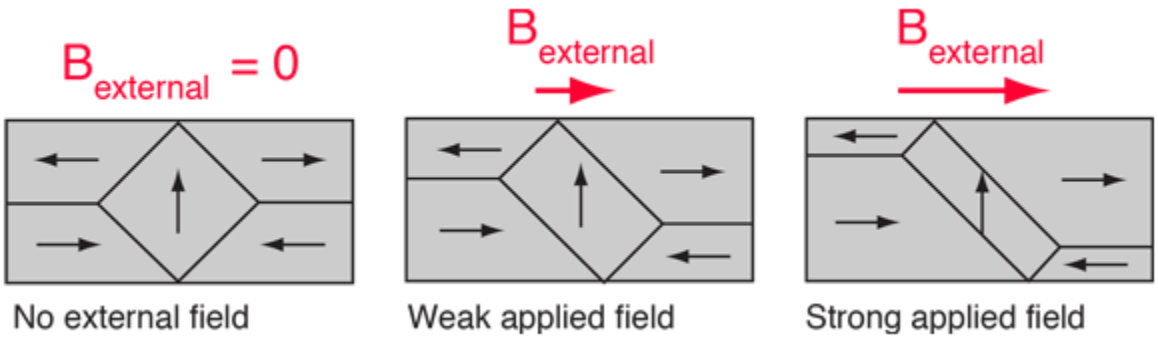

Figure 1-1 Schematic of magnetization process in ferromagnetic materials. An initial net zero magnetization with magnetic domains canceling out. A weak external field is then applied, and magnetic domains aligned with the external fields grow at the expense of the size of other domains. Finally, with the application of a strong electric field, the domains continue to grow in size. Adapted from [2]

One of the ways of characterizing magnetic materials is by analyzing their magnetic hysteresis. In other words, analyzing the process of magnetizing and demagnetizing these

materials. I will describe this process in simple terms in hopes of more clearly illustrating the behavior of the materials.

As described above, a ferromagnetic material that is demagnetized is one where the magnetic moments of the magnetic domains sum up to a zero net magnetization. If we want to magnetize this material, we must subject it to an external magnetic field. Upon the application of said external field, the domains whose magnetization more closely aligns with the direction of the applied magnetic field will grow in size. As the external field strength is increased, these domains will keep growing, overtaking the domains whose magnetization is not aligned with the applied field. At a certain point, all of the magnetic moments within the material will be aligned with the direction of the applied field in a state that can be called single domain. When this state is achieved, the material can be said to have reached saturation magnetization, and the field required for a material to reach this point is known as the saturating field. Each material has a different saturation magnetization and different field strength requirements to reach it.

Once a material has reached its saturation magnetization, it will remain in this state for however long the applied field is still acting upon it. However, upon the reduction in strength of this applied field, the material will begin to demagnetize through the growth of domains that are not in the direction of the originally applied field. This process will continue until the applied field is completely removed. Interestingly, upon complete removal of the applied field, the material still exhibits some net magnetization, known as its remnant state. This is a defining property of ferromagnetic materials. This phenomenon is why if you rub an iron nail with a permanent magnet, the nail itself will act like a magnet, even upon the removal of the permanent magnet. The degree to which a ferromagnetic material can retain magnetization upon removal of an applied field depends on many factors which will not be covered here.

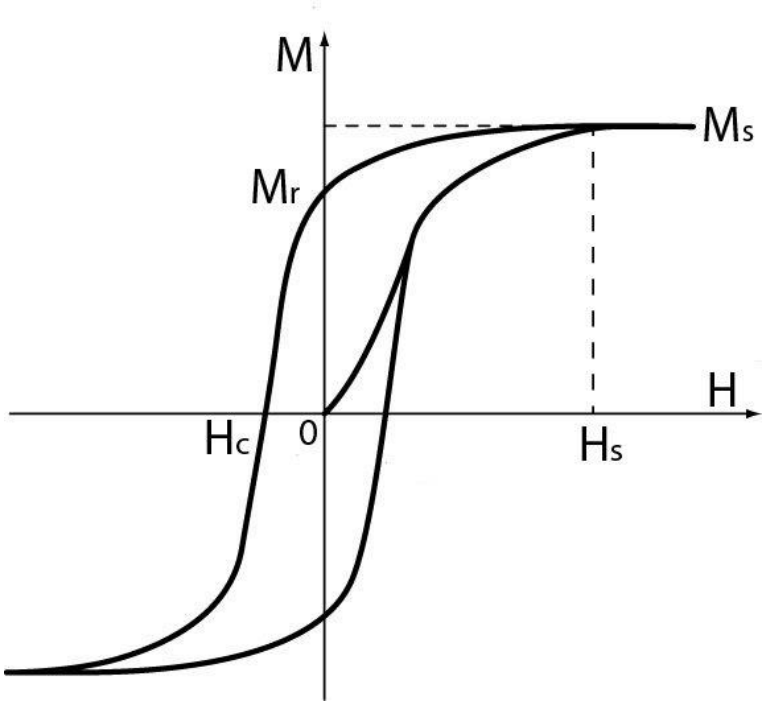

Figure 1-2 Example of an M-H curve showing the hysteretic behavior of magnetic materials. Image depicts the saturating field H_s and its corresponding saturation magnetization M_s. Upon removal of the applied field; the magnetization goes to its remnant state M_r. To demagnetize the material from its remnant state, a field of the magnitude of the coercive field H_c must be applied in the opposite direction to the original magnetization direction.

Upon reaching the remnant state described above, the ferromagnetic material will retain its magnetization indefinitely unless acted upon by external energy in the forms of mechanical or thermal, and electromagnetic energy. Assuming no mechanical or thermal energy acts to alter its magnetic state, we again need to apply an external magnetic field to the material to demagnetize it. By applying a field in the exact opposite direction to the original magnetizing field, magnetic domains aligned with this new direction will begin to grow, overcoming the predominant domains in the remnant magnetization direction. As this applied field continues to increase in the opposite direction, there will come the point where the net magnetization of the material reaches zero. At this point, the material is said to be demagnetized, and the field strength required to achieve this state is known as the coercive field. This coercivity depends on both material and geometric

factors[3]. The materials, which are commonly referred to as permanent magnets, exhibit very large coercivities meaning that they require very large fields to demagnetize them, making them very stable. Materials with a large coercivity are known as magnetically hard, and materials with a very low coercivity are known as magnetically soft. They each have applications where they are useful. For example, magnetically hard materials are used whenever a material that can be magnetized indefinitely is needed, such as in the case of electric motors and magnetic memory storage devices. On the other hand, magnetically soft materials are used in applications where magnetic switching is needed, such as transformer cores and magnetic shielding devices.

If we further increase the applied field past the coercivity, we then begin magnetizing the ferromagnetic material in the opposite direction to the original magnetization direction. This process again continues until the material is saturated at the same saturation field described above. This process can be repeated and will thus create a hysteretic loop that will describe the magnetization of the material as it corresponds to an applied magnetic field. The area within this hysteresis loop describes the amount of magnetic energy that can be stored in the material.

II Basics of Micromagnetics

In the previous section, I described the general principles behind the magnetization and demagnetization of a ferromagnetic material. However, to accurately model the magnetization process of microstructures such as the ones that will be discussed in the following chapters, we need to introduce the concept of micromagnetics[4]. This field of study is important when one wants to understand the dynamic behavior of the magnetic moments within a magnetic microstructure. In this section, I will again only cover the basics since this topic could be expanded indefinitely. In 1955, the Landau-Lifshitz-Gilbert equation of micromagnetics was created[5]. This

phenomenological equation describes the dynamics of magnetization. The equation is written as follows:

$$\frac{d\boldsymbol{m}}{dt} = \mu_0\gamma\left(\boldsymbol{m} \times H_{eff}\right) + \alpha(\boldsymbol{m} \times \frac{\partial \boldsymbol{m}}{\partial t})$$

Where m is the normalized magnetization, μ_0 is the vacuum permittivity, γ is the gyromagnetic ratio, and α is the Gilbert damping factor. This equation describes the dynamic precessional motion of magnetic spins under the influence of an effective magnetic field. This effective field is made up of multiple terms, as shown below:

$$H_{eff} = H_{MCA} + H_{ext} + H_{ex} + H_{Demag} + H_{ME}$$

Where H_{MCA} is the magneto-crystalline anisotropy field, H_{ext} is the external field applied, H_{ext} is the exchange field, H_{ext} is the demagnetization field, and H_{ME} is the magnetoelastic field. Other terms can be added to account for other phenomena that influence magnetization. Below I will briefly discuss the role of each field in the effective field equation above.

The first term H_{MCA} is the field arising from magnetocrystalline anisotropy that accounts for the influence that the crystal structure of the magnetic material has on the preferred directions of magnetization. In certain crystalline materials, there are preferred directions of magnetization, while in materials that are polycrystalline or amorphous, this term becomes less significant as the different crystal directions typically average to zero.

The second term H_{ext} is the field that is applied to the structure. This magnetic field could be generated by external magnets or electric currents. The application of an external field on a ferromagnetic material will cause the magnetic moments within the material to tend to align parallel to it.

The third term H_{ex} is the field produced by the exchange interaction between atoms and their nearest neighbors. This field tends to cause the orientation of two neighboring spins to align parallel to each other. As described previously, this exchange interaction is the main reason for the parallel arrangement of magnetic moments within magnetic domains.

The fourth term H_{demag} is the demagnetization field. This field arises from the fact that a fully magnetized magnetic structure produces a lot of magnetic field lines outside of it. This is an energetically unfavorable state given the amount of energy stored in this stray magnetic field; therefore, there exists a demagnetization field that acts to demagnetize the structure and return the magnetic state to a more energetically favorable state. This demagnetization effect is evident in the edges of ferromagnetic films, where one can observe that the spins tend to align along the edge of the film rather than perpendicular to it. This occurs since spins aligned along the edge produce less of a stray field outside of the film. This demagnetization field gives rise to shape anisotropy in which the shape of the magnetic microstructure plays a very important role in the distribution of spin directions, for example, in the case of a micron-sized circular ferromagnetic microstructure. The circular shape itself would cause the magnetic state within the film to be in a vortex state to reduce the number of stray field lines produced.

Lastly, the fifth term H_{ME} is that of the magneto-elastic field. This field accounts for the phenomena where the application of a mechanical strain onto a ferromagnetic material will change its magnetization. The degree to which this influences the magnetization of a material is related to its magnetoelastic coupling coefficients. Depending on the sign of these coupling coefficients, the magnetization may tend to align parallel or perpendicular to the direction of the applied strain. As will be discussed in Chapter 3, using this mechanism, one can use acoustic resonance to generate magnetic oscillations within the magnetic material.

Other terms can be included in the H_{eff} equation to account for other observed phenomena such as spin transfer torque, spin-orbit torque, perpendicular magnetic anisotropy, and Dzyaloshinskii-Moriya interactions. However, for the sake of brevity and relevance to the devices presented in the following chapters, I only discussed the most pertinent components.

Using the LLG equation with the correct effective field components, one can predict the magnetization dynamics of a magnetic structure under the influence of an external field, a particular geometry, and strain. This model allowed us to optimize the design of the devices discussed in Chapter 2 and Chapter 3.

III Ferromagnetic Materials in Biomedical Applications

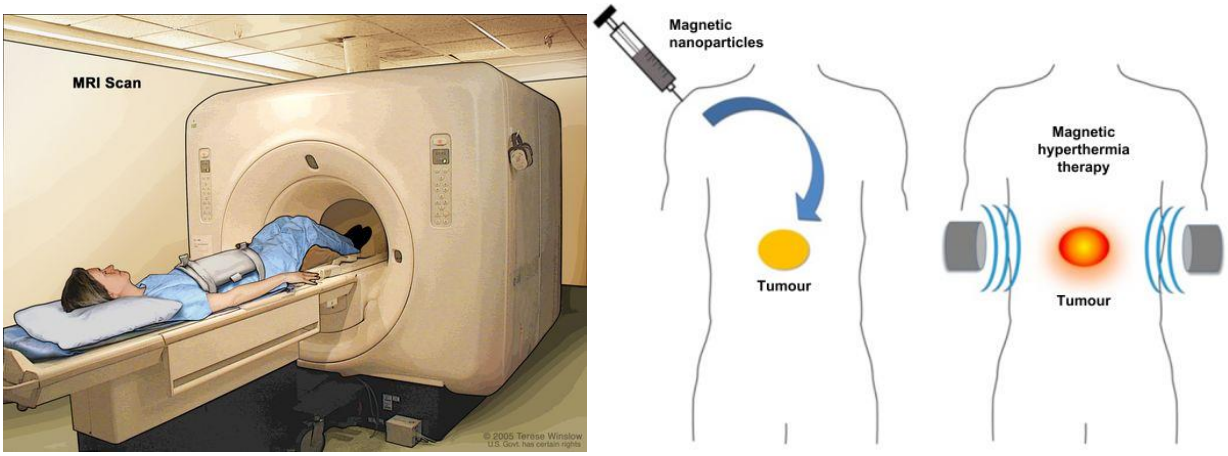

Figure 1-3 Applications of ferromagnetic materials in biomedical applications. (a) Magnetic Resonance Imaging Scanner. (b) Magnetic nanoparticles are injected into the body and excited with external magnetic fields to generate heat at the specific location of a tumor. Adapted from [6], [7]

Now that the physics and general mechanism of ferromagnetic materials has been outlined, I will describe some interesting applications of these materials. It is well known that ferromagnetic materials have been in use for thousands of years as tools for navigation. However, it wasn't until the early 19th century, when electromagnetism was better understood, that these materials began

to be used in more complex applications, such as the creation of electromagnets[8]. In the decades that followed, our understanding of ferromagnetic materials and electromagnetism as a whole paved the way for the creation of many new devices, such as the telegraph, electric motors, loudspeakers, etc. Today we see the use of electromagnetic equipment in basically every facet of our lives. However, one interesting application space of ferromagnetic materials that has garnered a lot of attention has been the biomedical industry[9]. As you may know, ferromagnets are commonly used in permanent magnet-based magnetic resonance imaging systems (MRI), where a strong ferromagnetic structure is used to magnetize the dipoles in our body. Interestingly, much of the work currently conducted on the use of ferromagnets in the biomedical industry today is in the application of these materials on the micro and nanoscale. For example, magnetic particles, such as iron oxide nanoparticles, are used in the medical industry for a variety of applications, including magnetic resonance imaging (MRI), drug delivery, and cancer therapy[10]. In MRI, these magnetic particles are used as contrast agents to enhance the visibility of certain tissues or abnormalities in the body. They are typically administered intravenously and then accumulate in the area of interest, such as tumors, where they create a stronger magnetic signal that can be detected by the MRI scanner. In drug delivery, magnetic particles can be coated with drugs and then directed to specific areas of the body using an external magnetic field. This allows for targeted delivery of the drug, reducing side effects and increasing its effectiveness[11]. Magnetic particles are also being investigated for use in cancer therapy, particularly in hyperthermia treatment. When exposed to an alternating magnetic field, the particles generate heat, which can be used to destroy cancer cells in the body. This is known as magnetic hyperthermia. Additionally, magnetic particles can be functionalized with antibodies or peptides to target specific cancer cells and then be remotely triggered to release drugs via magnetic field[12], [13]. Another application of magnetic

materials, and one that I will be discussing in depth in the following chapter, is that of using magnetic particles to manipulate the position of single cells[14]. In summary, ferromagnetic materials play a very important role in many facets of our daily lives, and recently they have become increasingly popular in the biomedical industry. As our understanding of ferromagnetic materials continues to develop, we will see new, more creative uses for these materials in medicine and other fields.

1.1.2 Ferroelectrics and Ferroelastic

Given the fact that my work consisted primarily of fabricating and using ferromagnetic microstructures, I will not cover either ferroelectric or ferroelastic materials in as much depth. However, I will cover some of the basics behind the physics and some of the applications for these materials:

1.1.3 Ferroelectric Materials

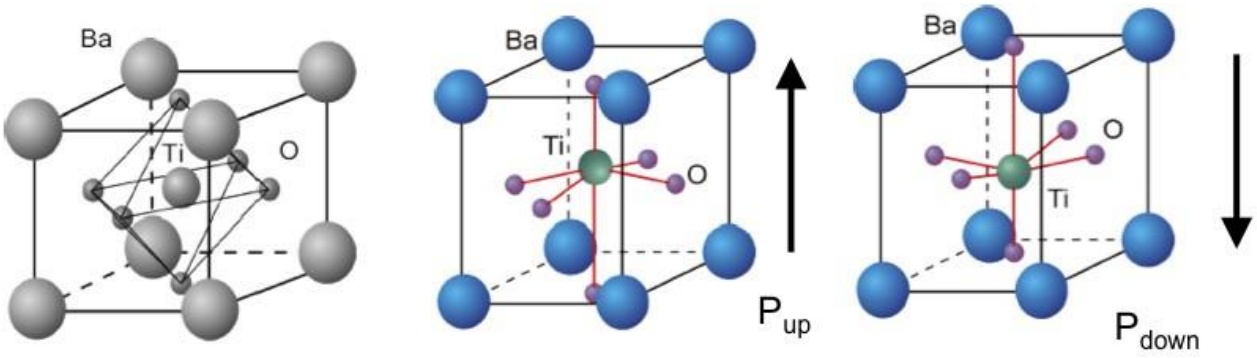

Figure 1-4 Ferroelectricity in $BaTiO_3$ crystal and the correlation between the displacement of its Titanium atom and the polarization of the material. Adapted from [15]

Ferroelectricity is a property of certain materials to exhibit a spontaneous electric polarization that is reversible upon the application of an external electric field. These materials are analogous in many ways to ferromagnetic materials, with the main difference being that instead of magnetization, these materials exhibit electric polarization. Similar to ferromagnetic materials,

ferroelectric materials also exhibit a hysteresis loop relating polarization and applied electric field. These materials have saturation polarization, which is the maximum amount of electrical polarization allowable within the material regardless of the electric field applied. Upon removal of the saturating electric field, the polarization will reduce to a non-zero value known as remnant polarization. To reduce this remnant polarization down to zero, an electric field in the opposite direction must be applied of a magnitude known as the electric coercivity. In addition to these properties, ferroelectric materials also are defined by the fact that their constant dielectric changes with temperature. This relation is known as the Curie-Weiss law. Finally, in a similar fashion to ferromagnetic materials, the spontaneous polarization of ferroelectric materials is dependent on temperature. At a certain temperature known as the curie temperature, the polarization is reduced to zero.

The properties of ferroelectric materials arise due to the arrangement of ions in the crystal structure of the material. In specific, these materials must be non-centrosymmetric to exhibit these properties. Examples of these materials include lead zirconate titanate (PZT), lead magnesium niobate – lead titanate (PMN-PT), and barium strontium titanate (BST).

The uses of these materials in the biomedical industry are plentiful, but they typically do not utilize their ferroelectric properties but rather just their piezoelectric properties which I will discuss in the following section. However, ferroelectric materials have found great usage in electronics and computer memory and logic devices where their spontaneous polarization can be used as an on or off state[16].

I Piezoelectrics

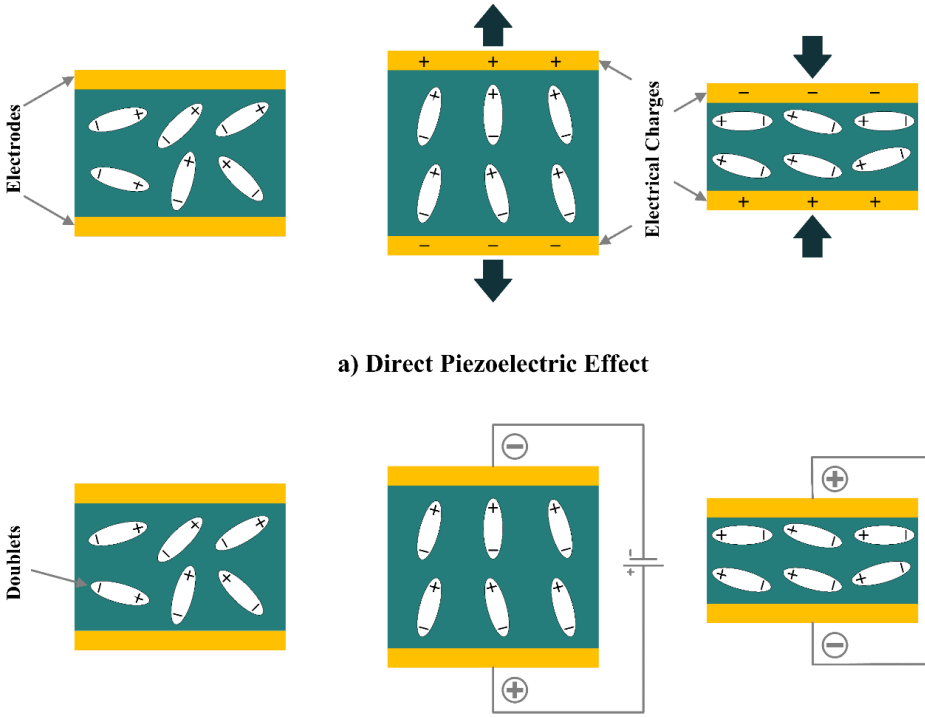

Figure 1-5 Mechanisms of piezoelectricity. (a) Direct piezoelectric effect, where mechanically deforming the piezoelectric material creates charges on the adjacent electrodes. (b) Converse piezoelectric effect where applying an electric field through the piezoelectric cause it to mechanically deform. Adapted from [17]

All ferroelectric materials belong to another larger class of materials known as piezoelectrics. These are materials that have electric polarization induced by mechanical strain, with the polarization being proportional to the strain and changing signs with it. In the same manner, mechanical strain in the material can be induced by an applied electric field, where the strain is proportional to the applied field and changes signs with it. Interestingly, these materials were discovered much earlier than ferroelectrics. They were discovered by Paul Jacques and Pierre Curie in 1880[18].

As described previously, these materials can be used in two different forms. The direct effect is when you subject a piezoelectric material to mechanical stress to generate an electric polarization within it. The converse effect is where you subject the piezoelectric material to an electric field to generate mechanical strain in the material. Both of these behaviors are described in the piezoelectric equations shown below:

$$D = dE + \varepsilon^T E$$

$$S = s^E T + dE$$

Where D is the electric displacement, T is the stress, E is the electric field, S is the strain, d is the piezoelectric coefficients, s is the material compliance, and ε is the electric permittivity. The superscripts on ε^T and s^E indicate that these parameters were measured while holding the stress and electric field constant, respectively. Using these equations and the correct material properties, one can predict the amount of polarization that can be generated given a certain mechanical strain or vice versa.

II Piezoelectrics in the medical industry

There currently exist many devices that use piezoelectric materials in the medical industry[19], [20]. One of the most common applications is that of ultrasound scanners[21]. In these devices, a piezoelectric material is used to generate ultrasonic vibrations at frequencies of approximately 5 MHz. These vibrations then travel within the patient and reflect after interacting with different tissues within the body of the patient. These reflected vibrations can be subsequently analyzed by piezoelectric sensors, and their response will correspond to an image of the tissues within the body of the patient. Besides this, other common uses of piezoelectric materials in the medical industry include precision surgical tools and dental scalers.

Although the uses described above are mature technologies, there is currently a lot of research into using these piezoelectric materials at the microscale for biomedical applications. I'll introduce some interesting applications. Piezoelectric materials have recently been used as energy harvesters in implantable devices[19], [22]. Given that implantable medical devices require electrical energy to power them, they typically use a battery to provide this energy. However, since the lifetime of a battery is limited, this would require a future surgical procedure to replace it, or it would require a complex wireless energy transfer system to charge the battery within the patient. Instead, one can utilize piezoelectric energy harvesting to convert mechanical energy from within the human body to electrical power that can be used to charge or power these implantable medical devices. Another medical use for piezoelectric materials is to use them for pressure or acoustic sensors within the body[23]. These devices can be easily miniaturized and designed to be sensitive to pressure changes at various scales. For example, pressure changes in the heart and the lungs and higher-pressure systems such as within the human cranium. These miniaturized sensors convert the surrounding pressure into some sort of mechanical deformation of a piezoelectric film, and this, in turn, gets converted into a detectable electrical signal. Besides these applications, there is a plethora of other interesting devices being developed for use in the medical industry. Many of the challenges today reside in finding biocompatible piezoelectric materials with high sensitivity and high reliability[24].

1.1.4 Ferroelectrics

As described previously, most of the work to be discussed in this dissertation is related to the use of piezoelectric and ferromagnetic materials. For this reason, I will not delve into detail describing the intricacies of ferroelastic materials. I will only briefly mention their behavior and some of their uses.

Ferroelastic materials are analogous to ferromagnetic and ferroelectric materials in that it exhibits a nonlinear stimulus-response. In the case of ferroelastic materials, they exhibit a nonlinear stress-strain relationship. They show a spontaneous mechanical deformation that can be reversed through the application of stress. In simple terms, these materials can be deformed through the application of some stress, and upon the removal of said stress, the material will retain that deformation.

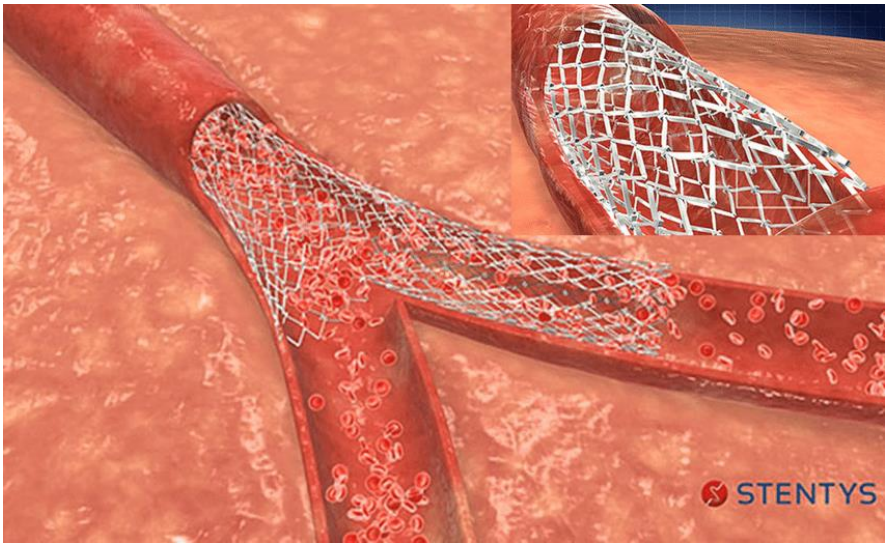

Figure 1-6 Ferroelastic Nitinol used for biomedical applications. In this diagram, Nitinol stents are used to hold open arteries. Adapted from [25]

An example of one such ferroelastic material that has been used extensively in the biomedical industry is Nitinol[26]. Nitinol is an alloy formed of Nickel and Titanium. This material exhibits exceptional mechanical properties such as superelasticity, which allows it to deform elastically a lot more than other metallic materials. Additionally, Nitinol exhibits a shape memory effect in which it can be deformed into a new shape through the application of stress, and then by heating, it can recover its original shape. Nitinol is also highly biocompatible, meaning that it can be used within the human body without detrimental effects. This material has been used in many ways in the biomedical industry. One of its most prominent applications of it is its use in

stents[27]. By first cooling the material and deforming it into a small form factor, it can be introduced into the diameter of a catheter which is subsequently introduced into an artery. Once inside, the heat within the body will allow the material to grow back into its original larger diameter and hold open the artery.

1.1.5 Multiferroics

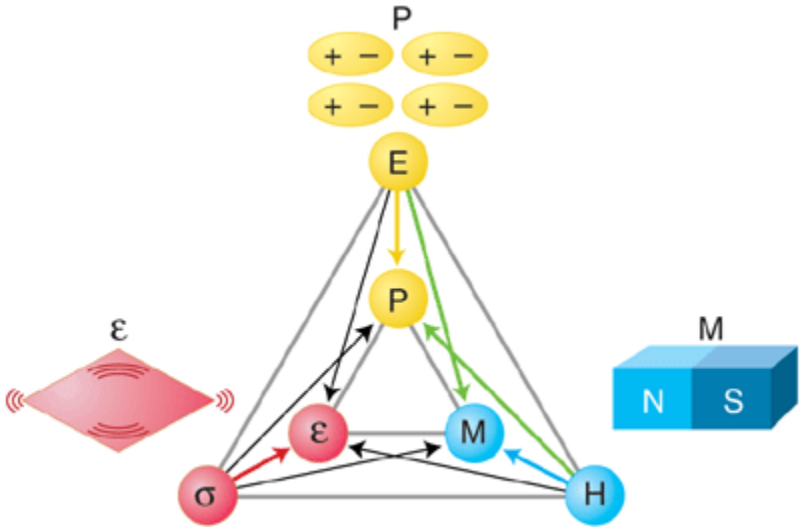

Figure 1-7 Multiferroic Coupling. This diagram shows the three ferroic material categories and their stimulus-response relationships. Additionally, the diagram shows the coupling that can exist between any two ferroic properties within a multiferroic material. Adapted from [28]

Now that I've discussed the background and the applications of ferromagnetic, ferroelectric, and ferroelastic materials, I would like to discuss a newly emerging class of materials that hold great promise for many industries, including the biomedical industry. These materials are known as multiferroics. These materials are those that simultaneously exhibit two or more ferroic properties, with the most commonly exhibiting both ferroelectricity and ferromagnetism. Although single-phase multiferroic materials exist, like TbMnO3 and BiFeO3[29], these materials are quite rare and often exhibit minuscule magnetoelectric coupling, which is not useful for practical applications. To address this, composite multiferroic materials were created. In these

materials, ferroelectric materials are deposited in composite structures alongside ferromagnetic materials. These distinct ferroic materials are typically mechanically coupled at their interface. By mechanically coupling the two separate ferroic phases, one can preserve both of their intrinsic properties leading to large magnetoelectric coupling[30]. The main benefit of these materials is that they allow for the control of magnetism through the use of electric fields. This is beneficial because classical approaches to control magnetism revolve around using electric currents to generate magnetic fields. As one miniaturizes devices, electric currents become increasingly inefficient to produce due to the increase in resistive losses. In contrast, multiferroic composites can be easily miniaturized since they only require electric fields to control magnetism, and electric fields can easily be scaled down in size without compromising efficiency. For this reason, there has been a growing interest in creating micro and nanoscale devices using multiferroic materials. These materials have primarily been studied for uses in computer memory applications, given their highly efficient control of magnetization at the micro and nanoscale. However, there has been some recent work on using these materials for biomedical applications. One such application is in the field of implantable communications devices. Given their outstanding miniaturization capabilities and their ability to control magnetization, researchers have designed small magnetic antennas that are biocompatible and emit strong magnetic signals which do not interact with the human body as much as electromagnetic signals emitted from traditional electrically small antennas[31]–[33]. The operation principle of these devices will be outlined more in-depth in chapter 3, but in summary, by applying an alternating voltage to a piezoelectric film, one can cause it to vibrate mechanically. If this piezoelectric film is then bonded to some ferromagnetic material that exhibits strong magnetoelastic properties, these vibrations will, in turn, cause the magnetization of the ferromagnetic layer to oscillate. These magnetization oscillations will then

emit magnetic fields from the device that can be detected at some distance away from the device. These devices hold a lot of promise and aim to replace the current inefficient implantable antenna technology available.

These devices have also recently been used in cell sorting and manipulation devices[34]. The goal of these devices is to capture an array of individual cells for single-cell analysis procedures. In these multiferroic devices, microscopic magnetic patterns are deposited onto a piezoelectric substrate. These magnetic patterns can be magnetized and will attract and capture any magnetically labeled cell that approaches them. Once captured, these cells can be examined. Then by applying a voltage onto the piezoelectric substrate, one can transfer the piezoelectric strain produced in the substrate onto the ferromagnetic structures, thereby changing their magnetic state. If this process is carefully tuned, one can magnetize and demagnetize the magnetic capture sites. By selectively demagnetizing these capture sites, one can release specific cells of interest for downstream analyses. These devices are still in the research and development phase but hold a lot of promise and will soon benefit the field of single-cell analysis. In chapter 2, I will discuss the work that went into designing a similar device that aims to achieve the same goal of single-cell capture and release by controlling magnetism on the microscale.

In summary, ferroic and multiferroic materials offer unprecedented benefits that other types of materials do not. Current research into these materials and their applications will soon revolutionize many industries ranging from computer memory applications to miniaturized communications devices and biomedical applications such as cell sorting.

Chapter 2. Magnetic Single-Cell Capture and Release Platform

2.1 Introduction

Cell sorting is defined as the process of separating a heterogenous mixture of cells into groups that exhibit one or more homogenous characteristics. These characteristics can include size, shape, surface protein expression, or a variety of other intracellular and extracellular properties [35]. Cell sorting is an indispensable technique for multiple biomedical applications, including drug discovery, personalized medicine, cancer research, etc. [36]. There is an astoundingly large variety of different approaches to cell sorting. Currently, the most commonly used approaches are Fluorescence Activated Cell Sorting (FACS) and Magnetically Activated Cell Sorting (MACS). The development of FACS dates back to the late 1960s when Herzenberg et al. developed the first cell sorting system based on manipulating the position of cells labeled with specific fluorescent biomarkers through the use of an electric field [37]. This system was promptly commercialized by Becton Dickinson in the 1970s and has since become the most popular system for cell sorting due to its high throughput and single-cell analysis capabilities. Even though FACS is the most mature and popular cell sorting system around today, it suffers from a number of limitations. These limitations include its use of expensive and complicated equipment, the production of biohazardous aerosols, and the inability to obtain time-dependent information on the sorted cells [38][4]. MACS, on the other hand, was developed in the late 1980s and early 1990s by James Miltenyi when he created the idea of using a magnetic mesh to trap immunomagnetically labeled cells flowing through a column [39]. Miltenyi also promptly commercialized this system with his company Miltenyi Biotec and today, it stands as the main competitor to the FACS systems. MACS have garnered a lot of popularity because of their extremely high cell sorting throughput and their versatile and simple-to-use platforms. However, MACS systems also suffer from some significant

limitations; these include the fact that they are not designed to sort out single cells but rather bulk populations. Additionally, these systems often produce large magnetic forces on the captured cells, which can damage them and mechanically alter cellular functions and viability. These two approaches represent the most mature and commonly used cell sorting systems in laboratories presently, but their limitations render them unsuitable for a variety of applications that are of great interest to researchers today. An example of one such field of interest is the study of the transient behavior of single cells. This type of experiment cannot be conducted using FACS or MACS systems. For this reason, new cell sorting platforms with capabilities more tailored to these single-cell experiments are needed now more than ever.

2.1.1 Single Cell Sorting

Throughout the history of biology and medicine, it has been commonly accepted that the average behavior of a group of genetically identical cells is representative of the behavior of an individual cell within that group. However, with the development of single-cell analysis tools, this belief has been dispelled. It is now well understood that no two cells can be exactly identical, even within the same cell type [40]. There are phenotypic differences in cell morphology, quantitative variations in receptor numbers, and at the molecular level, variations in protein numbers [41]. The influence of these small variations can change the response of an individual cell compared to the average response. For example, certain individual cells have been shown to exhibit drug-resistant properties even when a drug is efficacious on the average population. These small variations in cell phenotypes can also account for the differences in cell proliferation rates and stress tolerance. Elucidating the mechanism behind how these variations lead to different cell behaviors will lead to significant improvements in a number of different biomedical endeavors, such as drug discovery and the development of new cancer treatments.

Given the importance of understanding the behavior of single cells, we must now focus on developing platforms that allow us to isolate these individual cells from their natural heterogeneous environments. Additionally, we must develop platforms that can allow us to isolate large numbers of individual cells in order to obtain statistically significant data.

2.2 Literature Review

Recently, microfluidic cell sorting has garnered a lot of interest due to the inherent benefits of using a microfluidic platform for single-cell sorting and manipulation experiments. These benefits include low-cost platform fabrication, small device dimensions comparable to those of single cells, low volume of reagent usage in experiments, special flow characteristics that allow for predictable cell trajectories, and the ability to sustain a cell culture within devices for a prolonged period of time. These benefits make microfluidic platforms ideal for single-cell sorting experiments [42].

The following section will focus on the different microfluidic single-cell sorting approaches that have been reported in the literature. Even within the subset of microfluidic approaches, there is a large amount of variation when it comes to the operating principles behind each device [43]. Here I will review the main types of mechanisms that have been reported and discuss the benefits and drawbacks of each.

2.2.1 Non-microfluidic Devices for Single Cell Manipulation

Prior to discussing the different types of microfluidic approaches, I will briefly mention some of the more commonly used non-microfluidic single-cell analysis tools reported in the literature. These include:

I Optical microscopy

Microscopes have been used since their invention to optically investigate single cells. Microscopy is well-suited for intracellular localization- and time-dependent studies [44]. The main drawback of using microscopy for single-cell analysis is its extremely low throughput since only a single cell can be investigated at a time. In order to draw any statistically meaningful conclusion, you have to obtain data on a large number of single cells, and this becomes unreasonably time-consuming using classical microscopy. In order to address this limitation, Automated Microscopy (AM) or High Throughput Microscopy (HTM) has been developed [45]. Here, arrays of single cells are fixed to specific locations, and an automated microscopy system captures images at given time intervals and at specific locations. The main limitations of AM are still its relatively low throughput compared to other single-cell sorting systems and unnecessarily large containers for single cells (single wells in 96/384 well plates), as well as the large amounts of data that are generated from these experiments.

II Micropatterned Substrates

A commonly used method of cell isolation is using substrates such as glass or silicon with functionalized surfaces that enable the capture or adhesion of specific cells only at precise locations. These patterned substrates can trap the cells at these specific locations using either physical or chemical mechanisms.

Patterned substrates that use physical boundaries to isolate the individual cells from their neighbors are known as microwell devices [46], [47]. These devices are created using standard photolithography and etching protocols to create single-cell-sized well structures where arrays of individual cells can be mechanically trapped at particular positions for prolonged periods of time. These devices are designed to function in the same way as standard macroscale plastic multi-well

plates but have the added benefit of lowering the volume of reagents necessary per individual well and increasing the number of experiments that can be performed per cm^2. The design of these wells can be modified in a number of ways by varying parameters such as well size, shape, and number of wells to better suit the experiment at hand. There aren't many drawbacks to this type of device given their simple operating procedure, but they are limited to only a certain type of experiment where only cell isolation is necessary. These devices are not suited for cell sorting processes since these wells cannot separate different cell types.

The next type of micropatterned substrate devices are those where the surface chemistry is modified to allow the adhesion or repulsion of certain cells at specific locations [48], [49]. This is done using cytophilic or cytophobic compounds like fibronectin or PEG, respectively. By coating the substrate with these compounds and patterning the coating into small single-cell-sized islands using photolithography, one can make sure that cells attach only in predetermined positions. Similarly to microwell devices, these devices allow us to organize groups of cells into arrays of predetermined size and spacing. After capturing cells at specific locations and conducting experiments on them, it is often desirable to release these captured cells for downstream analysis. There are multiple examples of devices that allow for the release of captured single cells using a variety of stimuli, such as mechanical vibration, localized heat, and chemical release methods. These devices can be successfully used for the selective capture and release of individual cells, but they suffer from the limitation that they are typically designed for the capture of only one specific type of cell and have to be modified to accommodate other cell types. The throughput of these devices is also very low, so it is difficult to use them in any sort of clinically relevant cell sorting procedure.

2.2.2 Microfluidic Devices for Single-Cell Analysis

As described above, microfluidic platforms are well suited for single-cell sorting experiments due to their low-cost fabrication, small dimension, low volume of reagent usage, laminar flow characteristics, and the ability to sustain cell cultures. Given these advantages, researchers have developed numerous single-cell sorting devices that incorporate microfluidic channels. These devices can generally be categorized as either passive or active devices.

I Passive Devices:

Passive single-cell sorting devices utilize inherent properties of the flow within the microfluidic channel or properties of the cells to separate the cells into different groups. By carefully designing the channel geometry, one can separate cells based on their size, density, mechanical properties, etc. Examples of the mechanisms these devices use are microfiltration, droplet encapsulation, and hydrodynamic trapping.

i Microfiltration

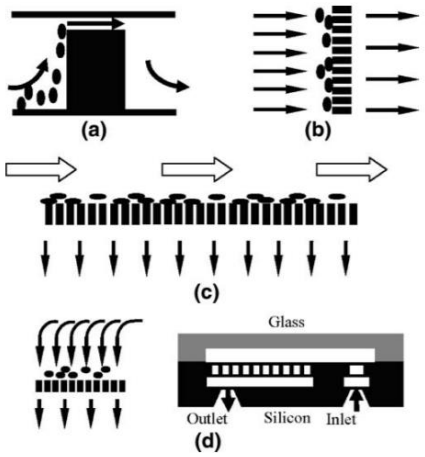

Figure 2-1 Examples of three different microfilter geometries. (a) Weir-based design. (b) Pillar-based design. (c) Pillar filter in crossflow configuration. (d) Dead-end membrane filter. Figure adapted from [8]

Microfiltration is the simplest microfluidic sorting mechanism that is commonly used. As the name suggests, cells flow through some sort of obstructing structure that only allows cells of a particular size to pass through, while bigger cells get trapped in the filtering structure [50]. This type of device only works when the desired cells to be captured are of a significantly different size than the unwanted cells. These devices have been shown to work using various filter structures such as weir, pillar, cross flow, and membrane filters [51]. Ji et al. [52] have compared the efficacy of each of these structures for sorting white blood cells from red blood cells. In their study, they concluded that the crossflow design outperforms the other microfilter types by demonstrating a whole blood handling capacity of >300ul while an average efficiency of >70-80% in trapping WBC and letting RBCs pass through.

Even though these systems offer relatively high throughput in the specific applications they are used, they are limited by one main flaw: they suffer from clogging issues, which render them unusable for long-term sorting. Additionally, high pressure and shear forces at the filtering locations can induce significant forces onto the cells, thereby damaging them or changing their behavior [53].

ii Hydrodynamic Trapping

Hydrodynamic single-cell trapping consists of using microfabricated structures to immobilize single cells at particular locations as they flow within a microfluidic channel [54]. These systems are similar to the microfilters described above but mainly differ in that microfilters are not designed to control the spatial distribution of the filtered cells.

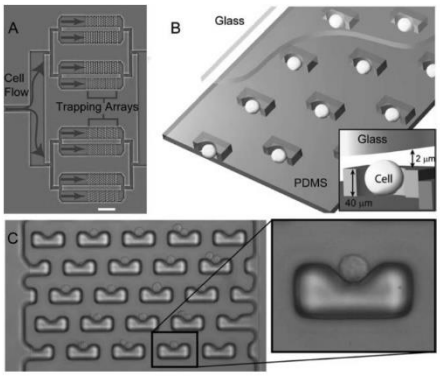

Figure 2-2 U-shaped PDMS microstructures used to isolate single cells at particular positions. (a) Photograph of the fabricated device with flow directions depicted. (b) Schematic of capture sites (c) Experimental image showing capture sites loaded with single cells. Adapted from [55].

There are currently many different hydrodynamic trap designs reported in the literature, an example of one of the earliest hydrodynamic single-cell trapping systems was developed by DiCarlo et al. in 2006 is shown in Figure 2-2, where they designed U-shaped microstructures within a microchannel to capture single cells [55]. The traps were carefully designed to allow for fast single-cell loading. The figure above shows the geometry and an experimental demonstration of the captured single-cell array. In this particular study, Di Carlo et al. studied the temporal behavior of the captured cells by quantifying their adherence, division, and death over time.

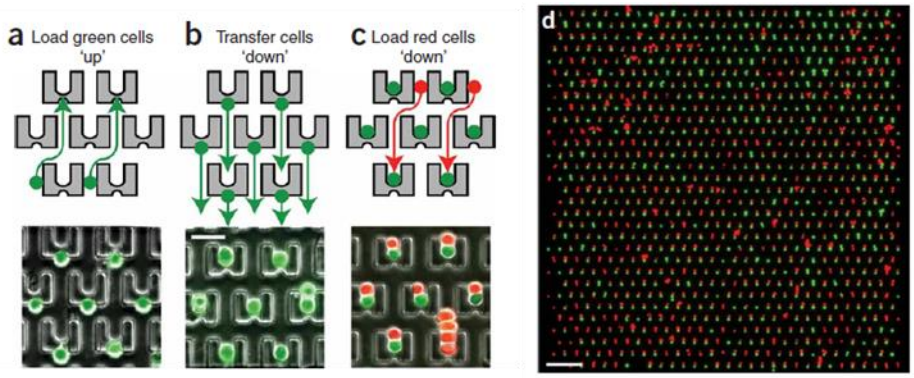

Figure 2-3 Microstructures Used for capturing pairs of single cells at specific locations and investigating cell interaction and fusion. (a)(b)(c) Device operation procedure consists of first loading the initial cell type by flowing the cells in the upwards direction and then loading them into the trapping sites by flowing them downward. The secondary cell type is then flowed downwards, and they are subsequently captured at each capture site alongside one of the initial cells. (d) Image of the array. Adapted from [56]

Another creative example of hydrodynamic traps was developed by Skelley et al., where they used microfabricated structures to trap a large array of pairs of single cells [56]. The operation consisted of three steps: an initial loading of the first cell type, a reverse of the flow to place these initial cells within the traps, and the loading of the second cell type. This device allowed the researchers to study the efficacy of chemical and electrical fusion between the pairs of captured cells.

Hydrodynamic single-cell trapping devices are simple, cost-effective, and high throughput systems for single-cell isolation. They also allow for temporal studies of the captured cells, given that they are compatible with cell culturing protocols. The only drawbacks to using these systems are the fact that retrieval of the captured cells is not possible and that shear forces on the cells from the flow may damage them [53].

iii Microdroplet Encapsulation

Another widely used technique for single-cell isolation and single-cell studies is the use of microfluidic systems to encapsulate single cells within microdroplets. Microdroplet generators generally consist of two immiscible flows coming together at a junction where one of the liquids will be separated into small droplets by the balance of shear and surface tension forces exerted between the two fluids [57]–[59]. This technology is very mature and can be tuned to produce thousands of droplets per minute with a high degree of control of the droplet size. In order to encapsulate single cells in these droplets, the flow containing cells and media will be separated into microdroplets using an oil-based continuous phase flow. The figure below demonstrates this mechanism:

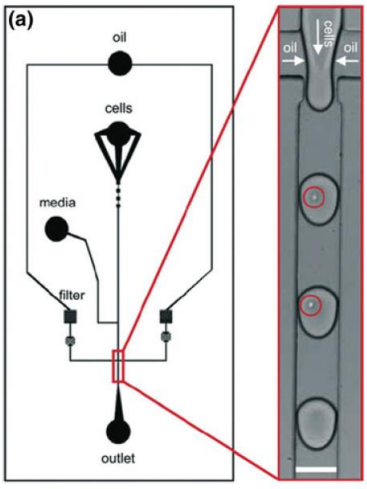

Figure 2-4 Microfluidic single-cell encapsulation device. (a)The layout of microfluidic channels and experimental image of single cells encapsulated within an oil-based flow. Adapted from [58]

These microdroplets isolate single cells from other cells and can act as small reaction chambers without the need to worry about cross-contamination. The small volume of reagents per droplet also makes these systems extremely efficient compared to other single-cell isolation systems where a large volume of reagents is wasted. Once encapsulated, these cells can also be

manipulated using a variety of means, such as magnetic, electrical, and optical forces, which is useful for cell sorting and categorization.

Even though these systems offer very high throughput and are very versatile, they still suffer from a number of issues. Primarily, the number of cells encapsulated per droplet follows a Poisson distribution meaning that a large portion of droplets will have more than one cell or have none at all, thus requiring a further purification step to identify those droplets with only single cells.

iv Inertial Cell Sorting

Inertial cell sorting refers to the usage of the inherent properties of the flow within a microchannel to manipulate the positions of cells or particles flowing within the channel. As particles flow within a microchannel, they are subjected to a number of forces that determine their dynamic behavior. These forces include Stokes Drag, wall lift, inertial lift, and Dean drag. Stokes drag is the force that moves the particles along the streamlines of the flow and is proportional to the velocity and viscosity of the fluid and the dimensions of the particle. Particles flowing in a microchannel are also subjected to lift forces when flowing near channel walls; these forces push the particles away from the channel wall toward the center of the channel. Inertial lift is a force that occurs when the particle Reynold's number is on the order of 1; these forces push particles in the direction of the shear flow gradient and towards the wall. When the channels are curved, the flow itself is subjected to inertial disturbances that produce flow perpendicular to the direction of the channel. This is known as Dean's Flow and also works to move particles away from the center

of the channel. By carefully designing the geometry of the channel and tuning parameters such as the flow rate, viscosity, and particle dimensions, one can tune the forces described above so that they create stable positions at particular locations across the cross-section of the channel. One can use this method to continuously separate cells of different sizes into different positions within the microchannel.

While cell sorting systems that use this mechanism have high throughput and are label-free, they are limited by the fact that the channel and flow characteristics are predetermined for a specific type of sorting process and have to be completely redesigned to sort out different cell types.

v Deterministic Lateral Displacement

Deterministic Lateral Displacement (DLD) is a size-based cell sorting method that uses a microfluidic channel with an array of obstacles placed within it[60]. These obstacles are carefully spaced out, and the position of every subsequent row of obstacles is shifted by a certain distance so that the flow interacting with the obstacles will create specific streamlines that constrict between the obstacle structures and subsequently expand after the obstacles. This can be used to sort cells based on size because the dimensions of the particles will dictate their trajectories as they flow through the channel. Small particles will tend to follow their original streamline, which will zigzag around the obstacles but generally moves down the channel with minimal lateral displacement. In contrast, at the regions between the obstacles where streamlines are constricted, large particles will change streamlines due to the fact that adjacent streamlines are now flowing through the particle's

center of mass. This change in streamlines causes a small lateral displacement which is amplified by the repeated interactions between these large particles and the obstacles. The transition between these two different trajectory behaviors occurs when the particle reaches a critical diameter (D_c) below which the cell will not be laterally displaced. This critical diameter can be carefully tuned by modifying parameters such as flow rate, obstacle spacing, array inclination, and fluid properties.

DLD systems have been widely used to separate many types of cells, including DNA fragments, oil droplets, blood, circulating tumor cells (CTCs), and many other bioparticles. There are a lot of benefits to these systems, including the fact that they are label-free, highly tunable, simple to operate and have a relatively high throughput. However, it still has many challenges to overcome before it reaches widespread adoption. These challenges include problems with clogging, high pressure gradients affecting cell viability, and the fact that each DLD platform is only designed for a specific sorting protocol, and the whole geometry has to be modified for other particle protocols.

II Active Devices:

Active cell manipulation processes are those that use external stimuli to exert forces on particles flowing within a microchannel. These systems are typically much more complex than the passive systems described above. However, they offer the benefit of providing a very high degree of spatial and temporal control over single particles. This is useful for many applications, such as single-cell analysis and cell-cell interaction experiments.

i Optical Systems:

Optical tweezing was discovered in the 1970s by Ashkin et al. at Bell Laboratories [61], [62]. They discovered that a focused laser beam would produce forces on micron-sized particles and cause them to move. The forces produced by the laser can be attributed to the transfer of momentum from the photons onto the particle as the light refracts through the particle. This force can be split up into two components: the scattering force, which is responsible for moving the particle in the direction of light propagation, and the gradient force, responsible for moving the particle orthogonally towards the gradient of the beam intensity [63]. The gaussian distribution of the intensity of the light beam makes the center of the beam a stable trapping location for particles due to the gradient component of the force decreasing to zero at this location.

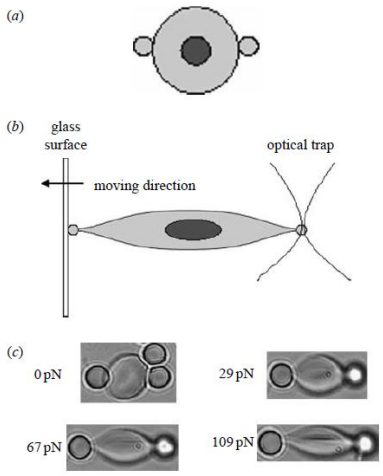

Figure 2-5 Investigating the response of red blood cells to mechanical stress using an optical trap to induce deformation (a) Initial state of the cell with two beads attached at the left and right side (b) Left bead is attached to a glass surface and the right bead is manipulated using an optical trap to induce deformation (c) Forces acting on cells and their respective deformed states. Adapted from [62].

Optical Tweezers have been used for many unique single-cell experiments, such as arranging individual cells to form specific group structures, mechanical deformability

measurements on single cells, single-cell trapping, sorting, etc. [64], [65]. As mentioned before, optical tweezers provide the highest degree of spatiotemporal control of microscale particles of the systems described here. However, they have many limitations that prevent them from being widely used. These limitations include its use of expensive and complex equipment, the fact that laser properties must be tuned to function with the cell's optical properties (size, shape, refractive index), which are not tunable and are often difficult to design for, the cell damage caused by high powered lasers, and most significant of all, the low throughput given that a single laser beam can only control one cell.

ii Electrical Systems:

Electric fields have been used in many different approaches to manipulate, trap, and sort single cells. These approaches include electrophoresis, electroosmosis, and Dielectrophoresis (DEP) with its many variants [66]–[68]. Here I will only describe DEP-based systems due to their maturity and robustness compared to the other electric field-based approaches.

Dielectrophoresis:

Dielectrophoresis is the method of using nonuniform electric fields to induce forces on cells. There are many variants of this mechanism, but the general principle is the same. Given that cells carry electric charges, an applied electric field will induce a change in polarization in the cells. Once polarized, these cells will be attracted to or repelled from the location of the highest electric field gradient. The degree to which these cells respond to this non-uniform field is dictated by the difference in permittivity between the cell and the medium in which they are suspended,

the gradient of the electric field, and volume of the cell, and the frequency of the applied electric field.

As for its use in single-cell trapping systems, micropatterned electrode arrays can be placed at the bottom of microfluidic channels and can be individually controlled to attract or repel cells at specific locations using DEP. An example of one such system is shown in [69], where Taff et al. developed one of the earliest examples of a single-cell capture and release array using DEP.

DEP systems have been continuously improved since their development in the 1960s by Pohl et al. [70]. This makes them one of the most mature cell sorting technologies around. In addition to their maturity, these systems are very robust and offer a relatively high throughput while being label-free. However, they also suffer from a number of limitations, such as the need to use a low conductivity buffer within the microchannel, which has been reported to negatively affect cell viability[71], cell damage caused by joule heating, bubbles formed by electrolysis, and electrode degradation with repeated use.

Optically Induced DEP (ODEP):

In 2005 Chiou et al. developed an interesting variation on DEP that uses light to induce the creation of electron-hole pairs on a photosensitive surface that, in turn, produces a nonuniform electric field through the microfluidic channel at the location of the light beam [72]. This nonuniform field serves the same purpose as in the DEP devices described above and can be used to either trap or repel particles. The main benefit of these systems is that these light beams can be focused down to the micrometer scale and can also be projected onto the device in arbitrarily complex shapes allowing for much

more freedom when it comes to manipulating the spatial position of individual cells or groups of cells. A demonstration of this system is shown in the figure below:

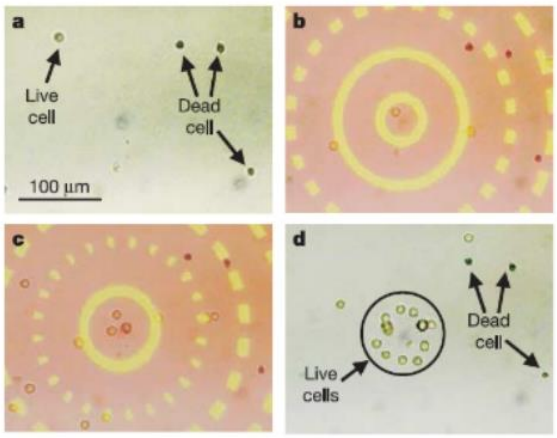

Figure 2-6 Spatial cell manipulation using light-induced dielectrophoretic forces. (a) Live and dead cells near each other. (b)(c) Using concentric circles of light to group live cells together. (d) Live cells are grouped together and isolated from the dead cells. Adapted from [72].

These ODEP systems offer precise spatial manipulation of cells comparable to that of optical tweezers but can do so with much higher throughput and with simpler equipment, given their unique operating mechanism. These systems aren't without their flaws. However, they still suffer from a lot of the same issues as traditional DEP systems, such as cell viability issues with their low conductivity buffers and incompatibility with traditional microscopy systems, given the opaque substrates these systems are built on.

iii Acoustic Systems:

Acoustic cell sorting refers to the use of devices that use piezoelectric substrates patterned with electrodes to generate mechanical waves, which are then transferred to the fluid within a microchannel. These resonant mechanical waves in the fluid will produce nodes and antinodes at

specific locations along the channel, which provide stable spatial trapping of particles of specific sizes and densities[73]. These systems have been traditionally used for continuous cell sorting processes where a specific cell type is deflected from its original path in a microfluidic channel, allowing them to be collected in a channel outlet different from that of other cells in the heterogenous mixture. These systems have the benefit of being label-free and have been shown to provide high throughput without damaging cells [74]. However, here I want to focus on acoustofluidic systems that provide the capability of single-cell trapping and manipulation. An example of one such system is shown below:

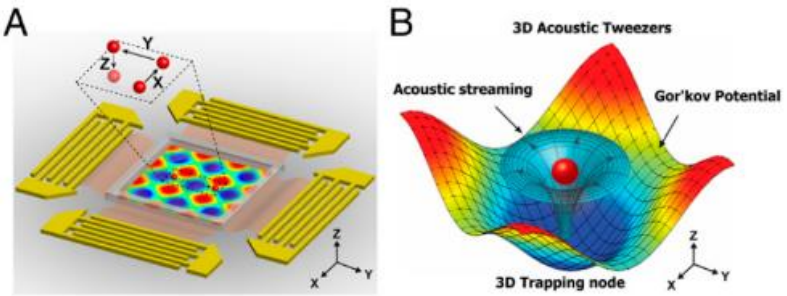

Figure 2-7 Acoustophoretic single-cell manipulation device. (a) Schematic of electrode arrangement and an array of trapping locations showing nodes and antinodes (c) 3D potential energy map for trapping node. Adapted from [75].

Guo et al.[75] developed a device known as “acoustic tweezers” that allows for precise three-dimensional spatial manipulation of individual cells or groups of cells using acoustics. Their design uses two orthogonal sets of interdigitated electrodes patterned on a lithium niobate substrate to produce mechanical waves through the fluid. By carefully tuning the phase of the mechanical vibrations from each set of electrodes, they can create a two-dimensional array of acoustic vibrational nodes in the fluid, which are used to trap the individual cells. By then tuning the amplitude of these vibrations, they can also manipulate the captured particles in the out-of-plane direction. These individual cells can be translated in three dimensions by adjusting the phase and

amplitude of the signals to the electrodes. This device can accurately control the position of single cells and particles down to a micron in size which can be used to build complex three-dimensional cell structures. The capability of building these structures makes this device useful for applications such as tissue engineering and regenerative medicine.

The main drawback of these systems is their complex fabrication and the difficulty in manipulating multiple single cells individually, given that the pressure nodes generated from the surface acoustic waves are uniformly distributed in an array.

iv Magnetic Systems:

Magnetic fields have been successfully used for cell sorting and manipulation for decades [76]. The most commonly used magnetic system in both the industry and research setting is Miltenyi Biotech's MACS cell separation system [77]. As previously described, their system offers unparalleled cell sorting throughput but is designed to separate bulk-scale groups of cells rather than individual cells. This prevents this system from being useful in studies that focus on single-cell heterogeneity. For this reason, there have been many microfluidic approaches that incorporate the use of magnetic fields to capture and manipulate single cells. Here I will describe the general working principle behind these devices and show some representative examples.

Magnetic cell sorting and manipulation operates using the principle of magnetic attraction between ferromagnetic structures and magnetically labeled cells. There are variations on this mechanism where label-free sorting has been demonstrated, but these are rare and for very specific applications. For this reason, I will focus primarily on magnetic systems that manipulate immunomagnetically labeled cells.

Before any magnetic manipulation of cells can be conducted, the cells of interest have to be immunomagnetically labeled. Immunomagnetic labeling refers to the use of superparamagnetic iron oxide beads functionalized with antibodies to bind to specific surface markers on cells through antibody-antigen binding. By targeting a specific surface marker, one can label only a particular population of cells within a heterogenous mixture. These labeled cells are then essentially magnetic and can thus be separated from the rest of the mixture using either external magnets or micropatterned magnetic structures on a substrate.

In order to fully understand the mechanism behind these systems, it is important to understand how functionalized cells are attracted to magnetic structures. The force experienced by cells onto a magnetic structure is described by the following equation [78]:

$$F_m = \frac{V(\chi - \chi_m)}{\mu_0}(B \cdot \nabla)B$$

where F_m is the magnetic force, V is the volume of magnetic material attached to the cell, $\chi - \chi_m$ represents the difference in magnetic susceptibility between the magnetic particles attached to the cell and the medium in which the cell is suspended, μ_0 is the permeability of free space, and B is the magnetic flux density coming from the magnetic structure meant to capture the cell.

As can be seen from the equation above, the force acting on a cell depends on the total volume of superparamagnetic iron oxide beads attached to it as well as the magnitude and the gradient of the magnetic field acting on the beads. Since the total volume of magnetic beads attached to a cell is limited by the surface area and the number of binding sites of the cell, the primary method of enhancing the magnetic attraction force is by increasing the magnitude and gradient of the fields applied. This is the approach that most magnetic cell sorting and manipulation

systems use. MACS, for example, uses a magnetic mesh placed in the separation columns to increase the gradients of the field created by external magnets. This approach can also be used in microfluidic devices by using micropatterned magnetic structures to create high magnetic field gradient locations to enable single-cell trapping. An example of such a system is shown in the following image.

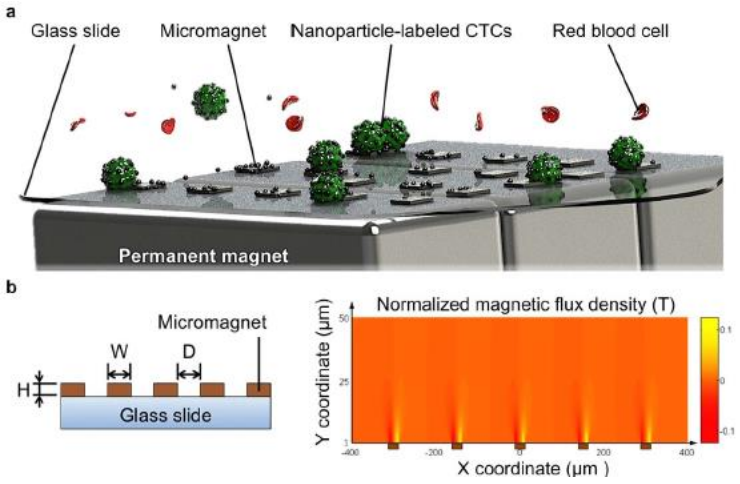

Figure 2-8 Magnetic single-cell trapping device. (a) Schematic of magnetically functionalized cells captured at the micromagnet locations while unlabeled RBCs are not captured. (b) Dimensions and layout of the device. (c) Magnetic flux density above each capturing site. Adapted from [79].

In their device, Huang et al. use a substrate with micropatterned Nickel magnetic structures to create high magnetic field gradient locations where single magnetically functionalized circulating tumor cells (CTCs) could be captured [79]. It is important to note that in this device, there are large permanent magnets placed underneath the substrate, which are used to attract the cells toward the bottom of the channel. Once the cells are close to the surface of the substrate, the cells are then attracted to the micromagnets since these are the locations with the highest magnetic field gradient. This allows for many single CTCs to be captured at specific locations. After capturing, the device can be used for CTC enumeration, which is useful for disease prognosis and for studying the effect of applied treatments on a patient. Additionally, given that this is a

microfluidic platform, one can also use immunofluorescent staining on the captured cells to study other properties of the captured CTCs. In this particular work, the authors stained the captured cancer cells with fluorescent particles to aim at identifying the presence of human epidermal growth factor 2 (HEF2) in the cells. The presence of HEF2 in cancer cells is directly related to increased proliferation rates making these cancers a lot more aggressive than HEF2-negative cancers. Using this process, they were able to successfully determine which cells had HEF2 and which did not, further exemplifying the usefulness of this device in CTC analysis.

Given the versatility and maturity of immunomagnetic labeling methods, one can use magnetic fields to sort cells based on numerous extracellular and intracellular properties, which are not feasible in label-free sorting processes. This gives magnetic and fluorescence-based systems an edge over many of the label-free methods described previously. Furthermore, magnetic systems have the added benefit of not interfering with or directly damaging cells due to the fact that cells do not inherently demonstrate strong magnetic properties, something that cannot be said for electric field-based methods.

Although the simplicity, versatility, and throughput of these devices make them very attractive for single-cell capture processes, they do have some noteworthy drawbacks. These include the fact that they are not label-free, which requires the magnetic labels to be removed from the cells prior to any downstream processing. Additionally, in certain devices, the magnetic capture force and the shear forces from the flow within the device are sometimes too large, resulting in cell damage and loss of viability.

III Single Cell Release

In the previous sections, I discussed the various methods that are currently used for single-cell trapping and manipulation, which are incredibly important for a number of single-cell studies. However, on-chip analysis of single cells is currently limited due to the incompatibility of microfluidic platforms with more complex single-cell analysis tools like mass spectroscopy. For this reason, a single-cell trapping microfluidic platform that can individually release cells of interest for further downstream analysis would be incredibly useful [80]. With such a platform, one could capture a population of cells and find those individual cells that exhibit some sort of interesting aberrant properties and release them for more complex downstream analyses like single-cell genomic, metabolomic, and proteomic studies. Additionally, these released cells can be cultured and expanded to populations large enough to be clinically relevant for purposes such as immunotherapy, where a large number of cells are required for therapeutic purposes [81].

Much of the literature that pertains to single-cell capture fails to mention the release of cells for downstream analysis. I believe this could be attributed to the added device complexity that this demands or ignorance of the importance of releasing captured cells. I will introduce the most noteworthy platforms that have been developed that can capture and release individual cells deterministically.

i Hydrodynamic Capture and Release

As described previously, these systems use hydrodynamic forces to capture single cells at specific locations. Once captured, these cells can be released using other microfluidic components, such as valves and side channels, to generate forces that oppose the original hydrodynamic capturing force. An example of one such system is presented below:

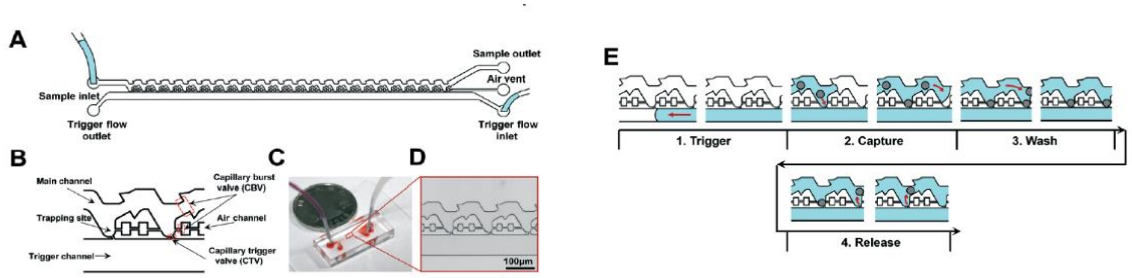

Figure 2-9 Microfluidic device allowing for single-cell capture and deterministic release (a) Overall schematic of the microfluidic device. (b) Zoomed-in view of the device structure, consisting of two types of capillary valves, three channels, and trapping sites. (c) Image of fabricated PMDS microchannel. (d) Zoomed-in image of each capturing site and the release valves. (e)Capture and release procedure. Adapted from [82].

Here Huichao et al. designed a very interesting microfluidic system that is capable of capturing and releasing single cells [82]. It achieves this using a clever microfluidic system that incorporates a carefully designed channel geometry, vents, and valves so that it traps individual cells as they flow into the channel. Once all the traps are occupied, the user can then release single cells one by one by adding pressure on the secondary channel to overcome the capture forces of the main channel. The main disadvantage of this system is that it can only release cells in sequential order starting from the last cell captured and, therefore, cannot take any arbitrary single cell and release it.

ii Biochemical Adhesion Approach

In these systems, individual cells are captured using the chemical binding process between a cell's surface makers and a chemically functionalized substrate. These substrates can be functionalized to capture only a specific type of cell. Once the cells are captured, they can be released by breaking these chemical bonds using a variety of means. There are many methods currently used to break the bonds of all the captured cells simultaneously, but I will focus the scope of this section on those methods that can be used to release single cells.

iii Photochemical Release

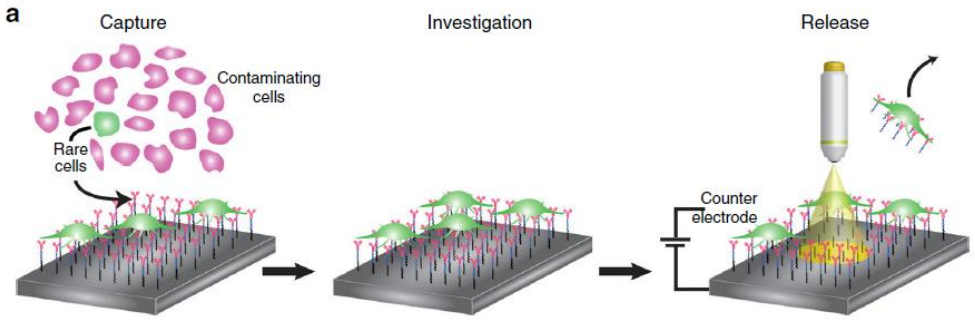

Figure 2-10 Schematic of cell capture using a chemically functionalized substrate and single cell release using light to break the chemical bonds between the captured cell and the substrate. Adapted from [83].

Parker et al. [83] designed a platform that captures rare cells using a biochemically modified surface that binds to specific surface markers on the rare cells. These cells can then be analyzed using conventional optical microscopy systems, and once a particular cell of interest is discovered, it can be released by projecting a light beam on the surface to break the chemical bonds between the cell and the surface. In order to not break the bonds while using the optical microscopy system, an electric potential must first be established on the substrate so that the light beam can photochemically alter the bonds. This process can be used to release a large number of cells or a single cell by modifying the size of the beam.

Even though this system can release individual cells with little to no effect on viability or function, it can only do so one cell at a time, which greatly reduces its throughput. This device is useful for particular applications of rare cell capture and release but is not compatible with automation.

iv Mechanical Release

Another method of altering the adhesion of single cells was presented by Reategui et al., where they used a vibrating microtip to mechanically denature the chemical bonds holding the

captured cells [84]. This method suffers from the same low throughput issues discussed above and is also limited by the size of the microtip, which is around 60 µm in diameter. So, any cells in close proximity to the cell which is meant to be released will also be released.

v Electrical Approach

As discussed previously, DEP-based devices use non-uniform electric fields to attract or repel electrically polarized particles or cells. This has been shown to be a very reliable method of capturing and manipulating the position of individual cells. This same method can be successfully used to release these captured cells by either removing the electric fields or modifying them to repel the captured cells. An example of one such device is presented below:

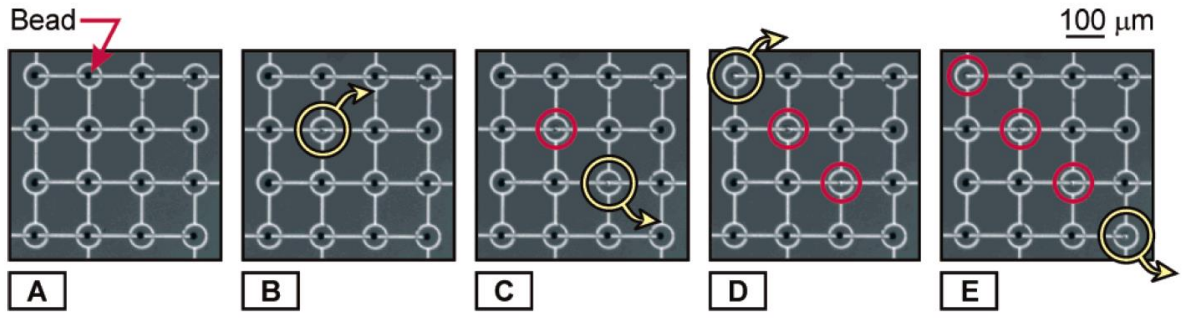

Figure 2-11 Single-cell capture and release using localized dielectrophoretic forces. (a-e) Capturing a 4x4 array of single cells at specific trapping locations and subsequently releasing the cells trapped along the diagonal of the array. Adapted from [85].

In this device, Taff et al. use an array of ring-like electrodes to generate a positive DEP force on cells flowing nearby to trap them at particular locations [85]. This device is also able to release a specific cell by grounding the electrode upon which that particular cell is captured. As can be seen in the figure above, the release process can be precisely controlled to release any individual cell in the array. This device is also compatible with automation, given that each of the captured sites can be electronically controlled. This makes this device highly scalable and can

provide high throughput. Besides the typical problems with DEP-based sorting systems, the only issues with this device are the size of the traps (100 um), which are large enough to trap more than one cell at any given location, and also the fact that in order to capture cells all of the traps have to be electrically active which may generate unwanted power consumption and heat, especially as the device scales in size.

vi Magnetic Approach

While magnetic and electric-based systems offer similar levels of precision when it comes to single-cell capture, magnetic systems are not typically well suited for individual cell release processes. This is because the magnetic capturing structures typically used in these systems are magnetically hard, meaning that they are difficult to demagnetize and thus will always attract magnetically functionalized cells towards them. In order to successfully release magnetically captured cells, one would have to find a way of reducing the magnetization of these structures to reduce the capture force on the cells. In magnetic systems where release has been achieved, as in the case of MACS, it has typically been accomplished by manually removing the large external magnets used for cell attraction. However, these systems release all of the captured cells simultaneously and cannot be modified to release single cells. Most magnetic systems used for single-cell sorting and capture that have been reported do not address this issue; however, recently, work published by Khojah et al. has demonstrated single-cell release using a multiferroic platform.

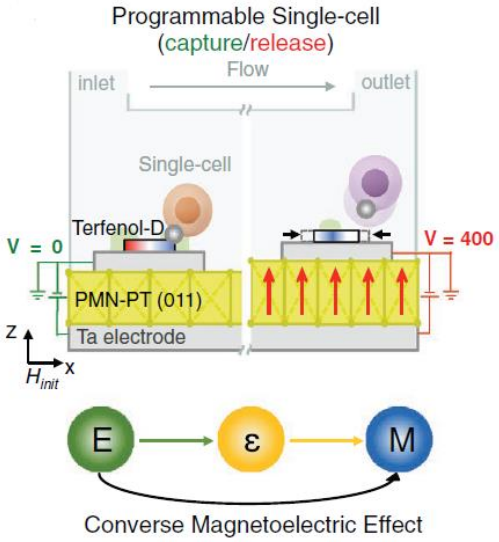

Figure 2-12 Magnetic single-cell capture and release using multiferroics to change the magnetic capture force exerted from the capturing site. Here a Terfenol D micromagnet acts as the capturing site, and the PMN-PT piezoelectric substrate acts to mechanically deform the micromagnet, thus inducing a magnetoelastic response which results in a cell release. Adapted from [34].

In their work, Khojah et al. use a multiferroic platform comprised of magnetic Terfenol D microdisks patterned on top of a piezoelectric PMN-PT substrate to capture magnetically functionalized cells and subsequently release them upon application of a voltage on the piezoelectric substrate[34]. The cells are released due to a change in magnetization in the Terfenol D disks that is caused by exploiting the strong magnetoelastic properties of the magnetic material. The piezoelectric substrate is first subjected to a voltage that causes it to deform mechanically. This mechanical deformation is then transferred onto the magnetic microdisks, which in turn causes the magnetization to change, given its magnetoelastic properties. This change in magnetization causes a sudden reduction in the attractive force acting on the cells, which in turn allows them to be carried away by the drag force of the flow in the microchannel.

This device is very promising, and it is one of the only successful demonstrations of single-cell release using a magnetic capturing platform. However, this paper fails to fully demonstrate the

addressability of each individual disk which is essential for precise single-cell release. Additionally, this system requires the use of external magnets to initially magnetize the microdisks into their capture state.

As previously described, the versatility, simplicity, and compatibility with biological specimens of magnetic systems make them very attractive for single-cell analysis systems; however, the blatant lack of single-cell release methods must be addressed before these systems are ready for single-cell analysis applications.

2.3 Proposed Device

In this section, I will present our novel microfluidic cell sorting device that consists of an array of individually addressable micromagnets that can capture and release single cells deterministically. This device does not aim to compete with current cell sorting systems in terms of throughput, but rather it is designed to allow researchers to be able to capture, culture, examine, and release specific individual cells all within a single device. These capabilities will allow researchers to not only observe the transient behavior of captured single cells but also to be able to release those cells for collection and downstream processing at any point in the experiment.

2.3.1 Design and Operation

I Design

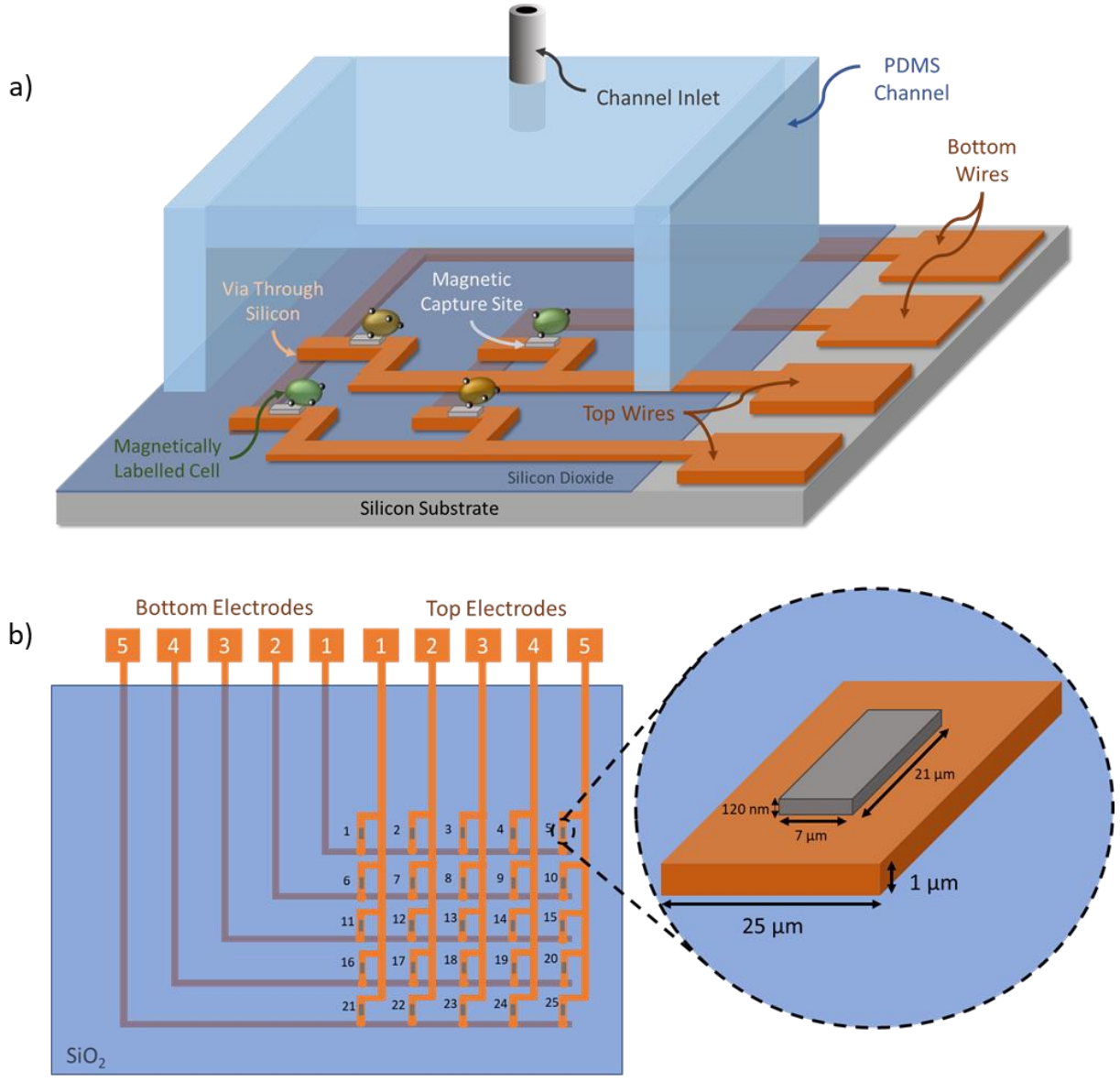

Figure 2-13 Schematic of proposed magnetic single-cell capture and release device using localized Oersted fields. This schematic depicts an array of capture sites placed within a microfluidic channel, with each capture site having a corresponding set of metal wires underneath, which are used for inducing magnetic changes on the capture sites. We also see each capture site with either a desirable or undesirable cell attached to it which alludes to the device's ability to investigate captured cells and subsequently release those desirable cells for downstream collection and analysis.

Our platform is comprised of three main components: (1) a PDMS microfluidic channel to guide the flow of cells, (2) a 5x5 element array of thin (120 nm) 7 μm x 21 μm rectangular iron magnetic capture sites, and (3) a network of copper wires used to magnetize and demagnetize individual capture sites. As shown in **Figure 2-13a**, the device is built upon a silicon substrate. The first layer from the bottom is a set of 5 horizontal copper wires which serve to deliver an electric current to capture sites on any row in the 5x5 array. Above these wires is a thin (120 nm) layer of insulating silicon dioxide that electrically separates the bottom wires from the top wires. This silicon dioxide layer has 25 small circular vias etched through it that allow for electrical contact between the bottom and top wires at specific locations to restrict the current flow to paths that will either magnetize or demagnetize only the desired capture site. Above this silicon dioxide layer is a second set of 5 vertical copper wires that allow the user to deliver electric current to any column of the capture site array. By running a current between any pair of bottom and top wires, the user can generate a highly localized magnetic field at any one of the capture site locations (Figure 1c). Above these top copper wires, the small rectangular iron magnetic microstructures are deposited, which function as capture sites for magnetically labeled cells. These capture sites are placed at the specific locations on the wire matrix where the largest localized magnetic fields can be generated. To prevent the wires and capture sites from oxidizing and interacting with the fluid/cell environment, the whole device is coated with a thin (200 nm) silicon dioxide layer to passivate the surface. To finalize the device, a microfluidic PDMS channel is bonded to the silicon dioxide surface, allowing the flow of cells to be guided over the magnetic capture sites.

II Operation Principle

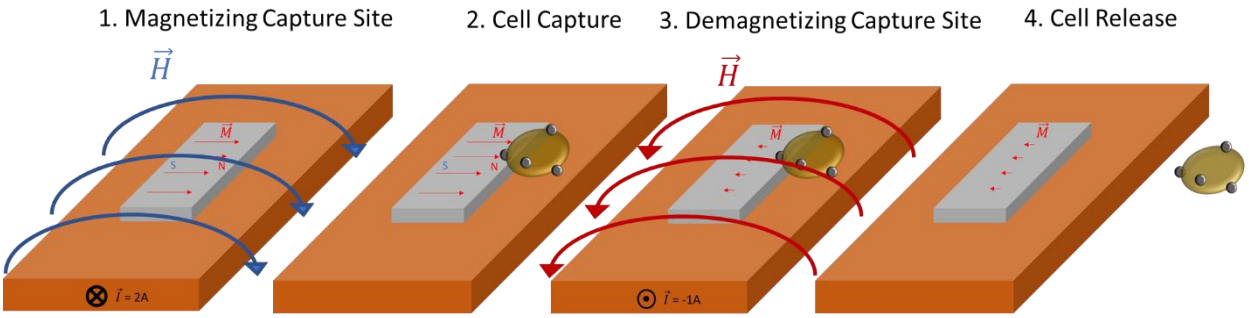

Figure 2-14 4-Step process to capture and release magnetically labeled cells. (i) Magnetization for capture site using a 2-amp electric current to magnetize the capture site. (ii) Magnetized capture site will exert an attractive force on the superparamagnetic beads labeling the cells and immobilizing the cell. (iii) Demagnetizing the capture site using a 1-amp current in the opposite direction to the original magnetizing current. (iv) A demagnetized or mostly demagnetized capture site will exert minimal force on the SPM beads, thereby allowing the drag force from the fluid to release the cells and be collected.

The proposed single-cell capture and release operation of our platform is broken down as follows:

1. The cells to be captured and analyzed are first magnetically labeled with superparamagnetic beads off-chip using standard immunomagnetic labeling procedures.
2. All the magnetic capture sites are first magnetically initialized into the capture state by running current pulses beneath each of them. These current pulses generate a large localized Oersted field that magnetizes the capture sites.
3. The magnetically labeled cells are then introduced into the microfluidic channel using a syringe pump and allowed to sediment to the bottom surface of the channel in order to get them to flow in close proximity to the magnetic capture sites.
4. As the cells flow within the channel, they get attracted to the capture sites and subsequently immobilized by the magnetic force acting between the capture site and the superparamagnetic beads labeling the cells.

5. Once the capturing procedure is completed, the user of the device can observe the individual behavior of cells over a period of time and determine which cells are suitable for downstream collection.
6. The cells deemed suitable for downstream collection can then be individually released by running an electric current in the opposite direction to the original magnetizing current. This current will act to demagnetize the capture site and drastically reduce the capture force exerted by the capture site on the superparamagnetic beads.
7. The demagnetized capture sites can then be remagnetized if additional cell capture is desired.

2.3.2 Modeling

Magnetic Force:

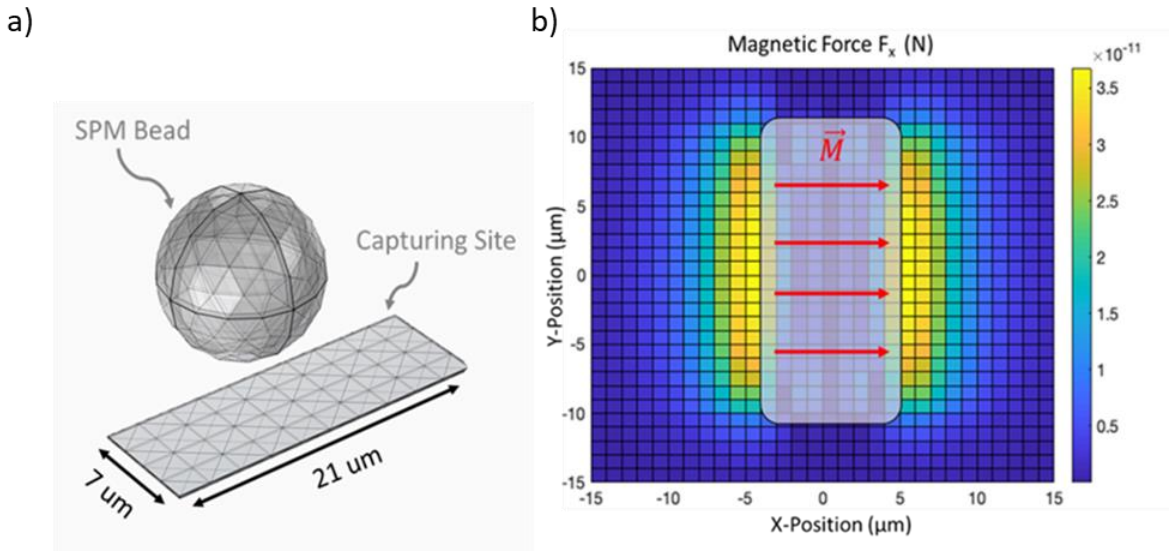

Figure 2-15 Finite element modeling of magnetic capture force and bead dynamics within the microfluidic channel. (a) Spatial distribution of attractive magnetic force between the magnetic bead and a magnetized capturing site. This distribution shows that the left and right edges of the capturing site exert the highest force on a bead, given that these are the magnetic poles of the structure. Bead and capture site meshed model geometry shown (top left inset).

To determine whether the capture site design and mechanism proposed above would be capable of capturing a magnetically labeled cell, we used finite element analysis (FEA) to calculate the magnetic attraction force between a magnetized capture site and a superparamagnetic bead nearby. Additionally, we used a moving-mesh finite element model to explore the dynamics of a superparamagnetic bead flowing along the microfluidic channel and being captured by a magnetized capture site and its subsequent release after site demagnetization. It can be seen in **Figure 2-15b** that the force generated on a superparamagnetic bead by a capture site magnetized along its short axis (F_M) is on the order of 30 pN at both left and right edges, corresponding to its magnetic poles or the locations of the largest magnetic field gradients. Knowing F_M, we were able to calculate the range of flow velocities that the superparamagnetic beads could be subjected to within the microfluidic channel while remaining magnetically immobilized by the capture site. This flow velocity (v_f) was calculated simply by equating F_M to the drag force F_D generated by the fluid dragging the superparamagnetic bead in the channel. The calculation was performed as follows:

$$\boldsymbol{F_M} = 30\ pN \geq \boldsymbol{F_D}$$

$$30\ pN \geq 6\pi\eta r_b \Delta\vec{\boldsymbol{v}}$$

Where $\Delta\vec{v}$ is the difference between the fluid velocity $\overrightarrow{v_f}$ and the particle velocity $\overrightarrow{v_p}$. Assuming $\overrightarrow{v_p}$ is 0 when the bead is captured, the equation simplifies to:

$$30\ pN \geq 6\pi\eta r_b \overrightarrow{\boldsymbol{v_f}}$$

Where η is the dynamic viscosity of the fluid and has a value of $8.9 * 10^{-9}\ Pa \cdot s$, and r_b is the radius of the superparamagnetic bead with a value of 4.25 μm. Further simplifying, we determine the fluid velocity to be:

$$\boldsymbol{v_f} \leq 3.57 * 10^{-4}\ m/s$$

Using this value and the cross-sectional dimensions of our rectangular microfluidic channel (w and h), we were able to determine the maximum volumetric flow rate Q of the fluid we could introduce into the channel and still capture the superparamagnetic bead. This was calculated as follows:

$$Q = v_f * A_{channel} = v_f * w * h \leq 3.57 * 10^{-4} \frac{m}{s} * 5\ mm * 500\ \mu m \leq 53\ \mu L/min$$

Therefore, we should theoretically be able to capture a superparamagnetic bead with a magnetized capture site at any volumetric flow rate below 53 μL/min. Using this flow rate, we modeled the dynamics of the superparamagnetic bead as it flows over a magnetized capture site and the dynamics of the bead after the capture site is demagnetized (**Figure 2-16**). In this model, the superparamagnetic bead flows through the channel alongside the fluid at a volumetric flow rate of 30 μL/min. As it flows above the magnetized capture site, the trajectory of the bead is altered, and the bead is pulled down onto the capture site and immobilized. Once the magnetic capture site is demagnetized, the model indicates that the bead is released and resumes its movement along the channel. The results from these two models demonstrate that the capture and release of a single superparamagnetic bead are possible using the proposed mechanism of magnetization and demagnetization of the capture site.

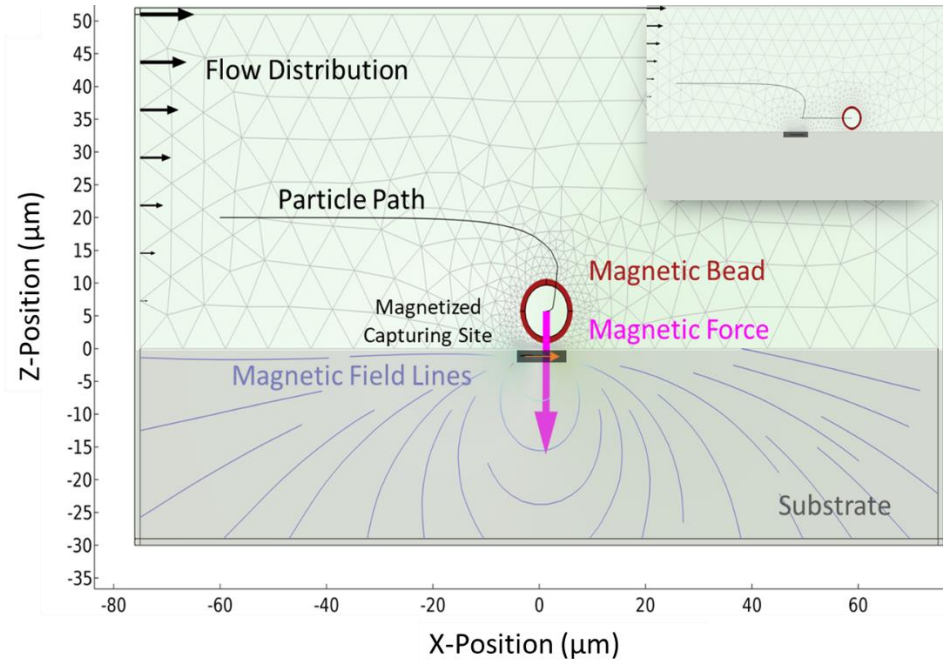

Figure 2-16 Moving mesh model of bead dynamics as it flows through the microfluidic channel above a magnetized capture site. Particle trajectory shows the capturing process as the SPM bead attaches to the capture site. The path of the magnetic bead after the capture site is demagnetized demonstrates successful release (inset top left).

Magnetic Fields from Electric Current:

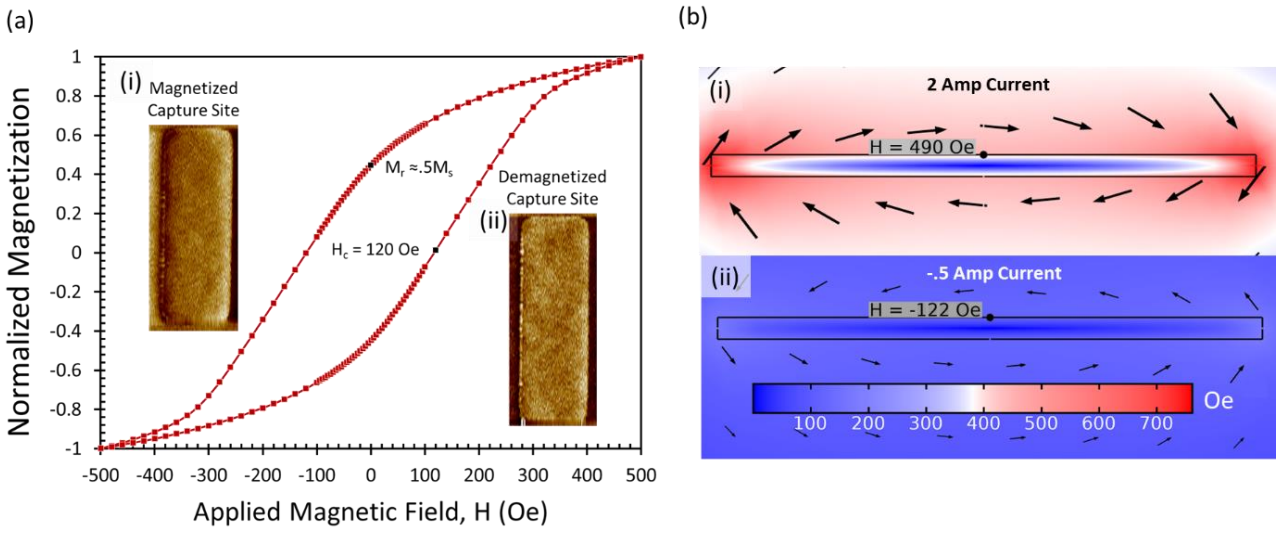

Figure 2-17 (a) Magnetic hysteresis of iron capture sites measured with Super Conducting Quantum Interference Device (SQUID) magnetometry. From this measurement, we know that we

need a 500 Oe field to magnetize the structures to saturation and that we need a field of about -120 Oe to demagnetize the structures. Inset images show experimental magnetic force microscopy (MFM) scans of a magnetized (top left) and demagnetized (bottom right) iron capture site. The magnetized capture site shows dark and bright areas on the left and right edges corresponding to the magnetic poles of the structure. In contrast, the MFM scan of the demagnetized structure shows no discernable poles. (b) Finite Element model of the magnetic field magnitude and direction produced around a current-carrying wire. (i) Field produced around a copper wire using the magnetizing current of 2 amps. It can be observed that on the top surface of the wire, where the capture site would be, the field produced is 490 Oe which is sufficient to magnetize the capture site to saturation. (ii) Field produced around the copper wire using the demagnetization current of -.5 Amps. It can be observed that the field strength at the top surface is -122 Oe which is close to the measured coercivity of the capture site.

With the knowledge that the proposed capture site could theoretically capture and release a superparamagnetic bead, we then determined the magnetic field strengths necessary to magnetize and demagnetize the site and whether these magnetic states would remain stable after the removal of the applied field. To determine the magnetizing field H_{Mag} and the demagnetizing field H_{Demag}, we fabricated an array of capture sites with the dimensions proposed above and experimentally measured their magnetic hysteresis using superconducting quantum interference device (SQUID) magnetometry. The results are shown in **Figure 2-17a,** where we see that the strength of the magnetic field H_{Mag} needed to saturate the capture site was on the order of $500\ Oe$ and the strength of the magnetic field H_{Demag} needed to demagnetize it was approximately $-120\ Oe$. Furthermore, we see that the magnetized state is stable since there is an appreciable remnant magnetization M_r, albeit only about 50 percent of the saturation magnetization M_{sat}.

After measuring the magnetic field strengths necessary to magnetize and demagnetize the capture sites, we determined the magnitude of the electric current needed to generate magnetic fields of this strength. To do so, we used FEA to model the magnetic field strength produced at the surface of a copper wire during the application of an electric current. We found that a current of approximately 2 A was needed to generate the 500 Oe magnetic field required to magnetize the capture site on the surface of the wire. We also found that a current of 0.5 A in the opposite

direction was required to generate the −120 Oe magnetic field necessary to demagnetize the capture site (**Figure 2-17b**).

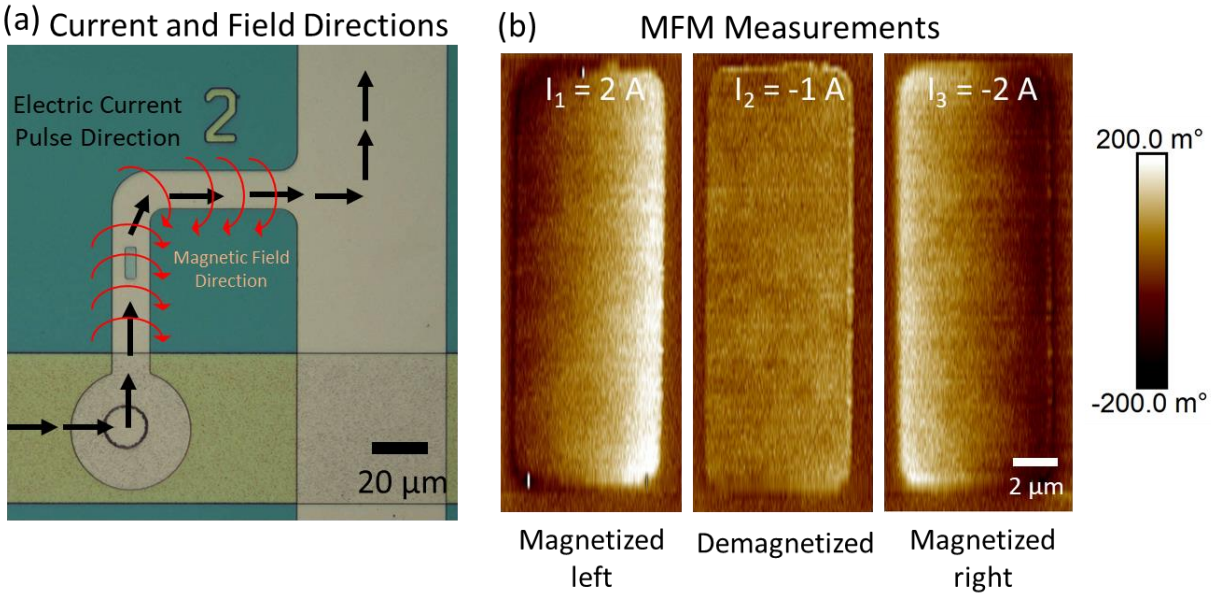

Figure 2-18 (a) Magnetic hysteresis of iron capture sites measured with Super Conducting Quantum Interference Device (SQUID) magnetometry. From this measurement, we know that we need a 500 Oe field to magnetize the structures to saturation and that we need a field of about -120 Oe to demagnetize the structures. Inset images show experimental magnetic force microscopy (MFM) scans of a magnetized (top left) and demagnetized (bottom right) iron capture site. The magnetized capture site shows dark and bright areas on the left and right edges corresponding to the magnetic poles of the structure. In contrast, the MFM scan of the demagnetized structure shows no discernable poles. (b) Finite Element model of the magnetic field magnitude and direction produced around a current-carrying wire. (i) Field produced around a copper wire using the magnetizing current of 2 amps. It can be observed that on the top surface of the wire, where the capture site would be, the field produced is 490 Oe which is sufficient to magnetize the capture site to saturation. (ii) Field produced around the copper wire using the demagnetization current of -.5 Amps. It can be observed that the field strength at the top surface is -122 Oe which is close to the measured coercivity of the capture site. (c) Microscope image of the capture site with arrows showing the direction of the current pulse and the corresponding magnetic field direction surrounding the wire. (d) Results from the MFM test. (i) Capture site magnetized using a 2-amp current pulse. We can clearly see that the left and right edges of the rectangular capture site are the brightest and darkest areas of the image, which correspond to the magnetic poles of the structure. (ii) Capture site demagnetized using a negative 1-amp current pulse. We can see no discernable magnetic poles, meaning the structure was successfully demagnetized. (iii) Remagnetization of the capture site in the opposite direction. Here we see that the location of the bright and dark areas of the MFM measurement have switched compared to (i) after applying a negative 2-amp current pulse.

With the electric current values obtained from the simulation, we proceeded to experimentally verify this magnetization and demagnetization procedure. To do so, we fabricated a device using the microfabrication process described in the following section and tested the magnetization and demagnetization process using magnetic force microscopy (MFM). In this experiment, we ran a 2-amp current pulse beneath the first capture site in the array and measured its magnetization state (Figure 2-18a). We observed that the largest attractive and repulsive magnetic forces between the capture site and the magnetized MFM scanning probe occurred at the left and right edges of the rectangular capture site, indicating that these were the magnetic poles of the structure. This meant that the capture site had been successfully magnetized (Figure 2-18b). We then ran a 1-amp current pulse in the opposite direction to demagnetize the structure and scanned it again. We observed no discernable magnetic poles, indicating that the structure had been successfully demagnetized. To further validate these results, we again ran a 2-amp current pulse, but this time in the same direction as the demagnetizing current, and we observed that the structure was remagnetized in the opposite direction as the first magnetization. This procedure was repeated for all 25 capture sites in the array, and all showed equivalent results indicating that we could successfully magnetize or demagnetize any capture site by running either a 2 or -1 amp current in the wire below it.

2.4 Experimental Results

2.4.1 Bead Capture and Release

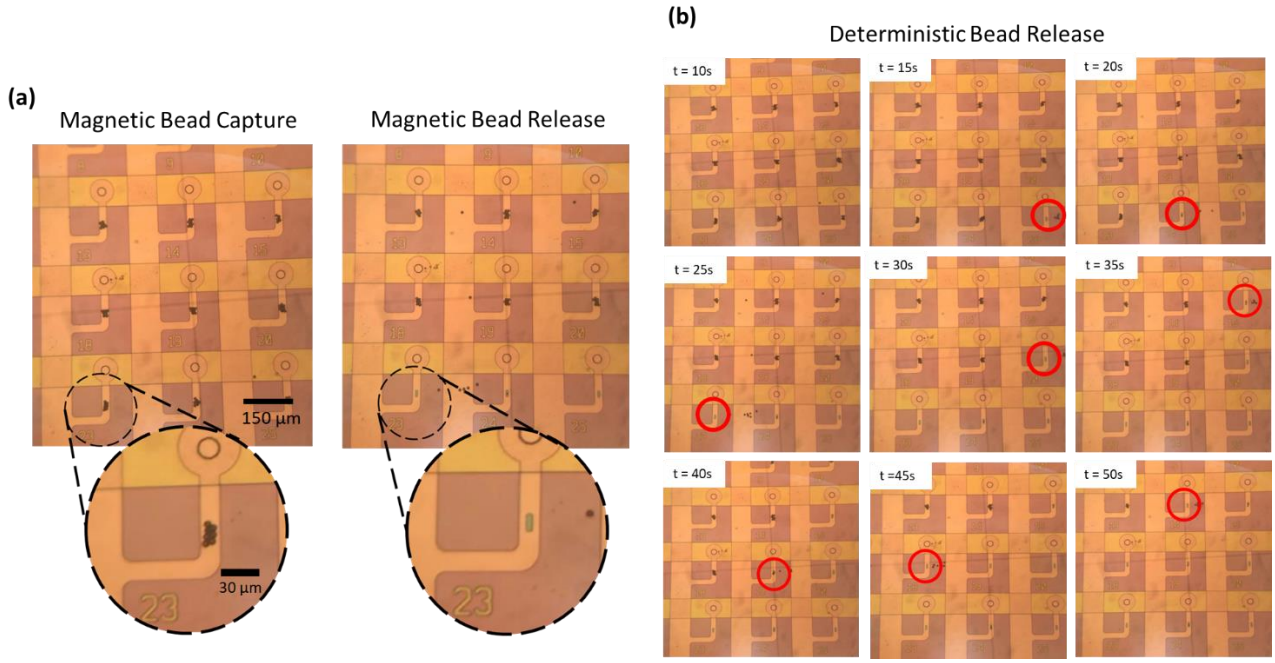

Figure 2-19 (a) Microscope image showing magnetic beads captured at each captured site in a 3x3 section of the larger 5x5 array. The image on the left shows a group of beads at each magnetized capture site. The inset more clearly shows the beads that are attached to capture site 23. The image on the right shows the results of demagnetizing the capture sites starting from the bottom right to the bottom middle to the bottom left. As can be seen, the beads are completely released and dragged away by the fluid in the channel upon site demagnetization. (b) Time-lapse images of individual capture sites releasing their captured beads. The release pattern was arbitrarily chosen to demonstrate the deterministic nature of the release process.

With the magnetization and demagnetization of single capture sites verified, we proceeded to experimentally verify the capability of our device to capture and release cells. Given the added complexity of working with live cells, we first tested the operation of the platform using only superparamagnetic beads. To better mimic the behavior of cells, we used 8.5 µm superparamagnetic beads as a substitute because they have a similar diameter to a cell and, therefore, the fluid will exert a similar drag force on them [86]. In this experiment, we first

initialized all the capture sites to the magnetic capture state by running a 2 A current pulse underneath each site. We then introduced the magnetic bead solution into the channel using a syringe pump with a volumetric flow rate of 30 µL/min. As the beads flowed within the channel, they settled toward the bottom due to their higher density relative to the suspension solution. Once at the bottom, the beads began flowing in close proximity to the capture sites until the magnetic attraction between the bead and a nearby site was sufficient to immobilize the bead. This process continued until all sites had captured the maximum number of beads they could hold. Next, we proceeded to release the beads captured at each individual site, starting from capture site 25, by running a 1-amp current pulse in the opposite direction to that of the magnetizing current. The results of this experiment are shown in **Figure 2-19,** where we see the sequential release of superparamagnetic beads from 8 different capture sites. This experiment demonstrated that the magnetic attraction between an 8.5 µm superparamagnetic bead and a magnetized capture site was sufficient to immobilize it at a flow rate of 30 µl/min which matched the behavior shown in the magnetic force and moving mesh simulations. Additionally, it demonstrated that we could deterministically release the captured beads on any desired capture site by using a current pulse of −1 A, which again confirmed that the magnetic capture sites were successfully demagnetized upon the application of this current.

2.4.2 Single Cell Capture and Release

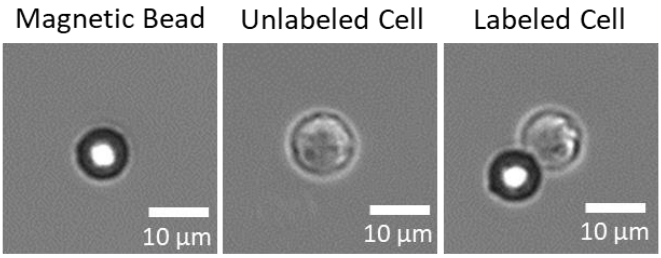

Figure 2-20 Microscope images of an 8.5 µm superparamagnetic bead, an unlabeled T cell, and a T cell tagged with one 8.5 µm superparamagnetic bead.

Further validation of the operation of this platform required a demonstration of its ability to capture and release magnetically labeled cells. To demonstrate this functionality, we labeled Jurkat T cells with 8.5 µm superparamagnetic beads using standard immunomagnetic labeling procedures. Since these labeling procedures are not perfect, the resulting cell solution consisted of labeled cells, unlabeled cells, and free superparamagnetic beads (**Figure 2-20**). Approximately only 30% of cells in the solution were successfully labeled with superparamagnetic beads. Prior to the introduction of the cells into the channel, the capture sites were magnetized using 2-amp current pulses. The cell solution was then introduced into the device at a flow rate of 30 µl/min. Given the relatively low concentration of labeled cells and the presence of free superparamagnetic beads, it took approximately 5 minutes before we observed successful cell capture at the majority of capture sites (**Figure 2-21**).

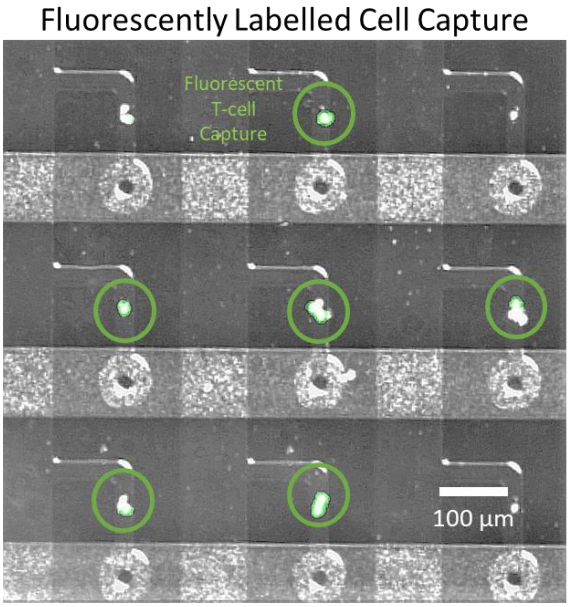

Figure 2-21 Capture of magnetically labeled T-cells as seen under a fluorescence microscope. Cells were fluorescently labeled prior to their introduction into the microfluidic channel.

Once captured, the cells were immobilized for approximately 30 minutes before we began the release process. This was done to demonstrate the fact that cells could be held indefinitely using these magnetic capture sites without the risk of random release. Once this was confirmed, we demagnetized the capture sites containing cells one at a time, using the same −1 A pulse described previously. Immediately upon application of the current, the captured cells were successfully released as the drag force overcame the magnetic capture force (**Figure 2-22**). This process was successfully repeated for all the captured cells. These results demonstrated that we could successfully capture single cells at discrete locations, magnetically immobilize them for extended periods of time, and ultimately release them one at a time for downstream collection.

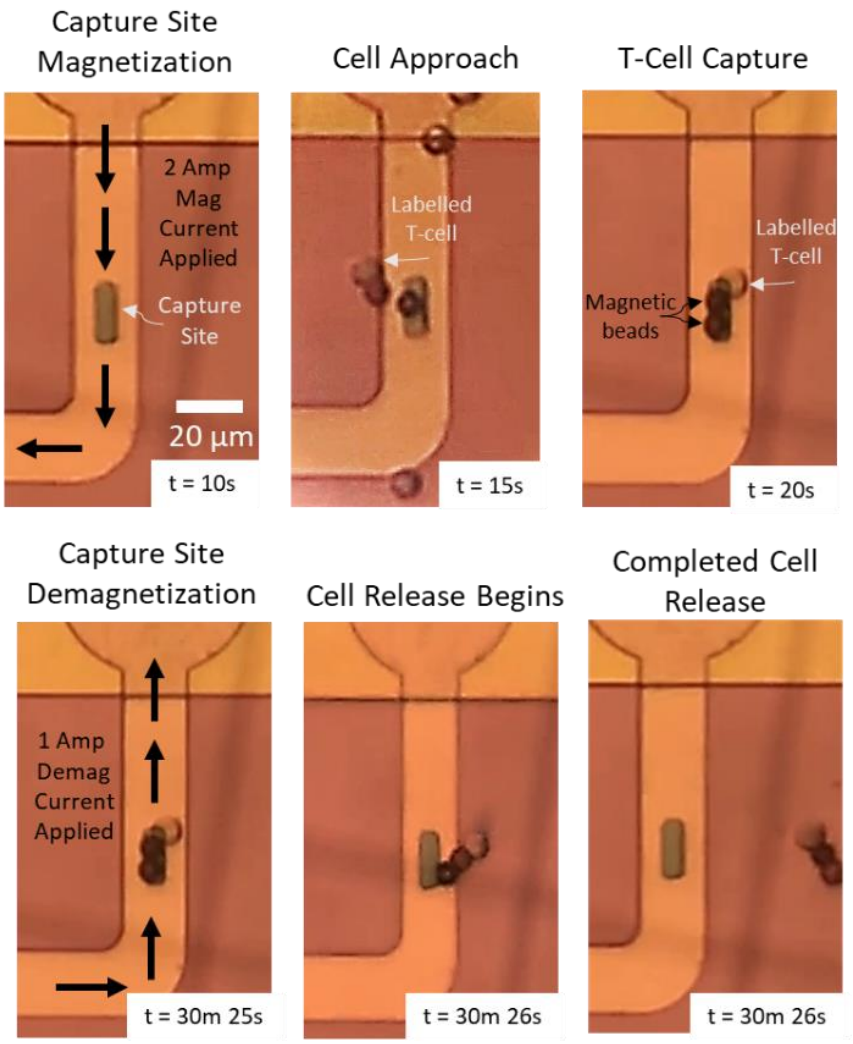

Figure 2-22 Time-lapse microscope images of single magnetically labeled T-cell capture and release process. The first image shows the magnetization current pulse applied. The second image shows the captured T-cell with its two respective magnetic beads. The third image shows the demagnetization current applied in the opposite direction as the magnetization current and with half the magnitude. The fourth and fifth images show the cell and the magnetic beads released from the capture site.

2.4.3 Microfabrication

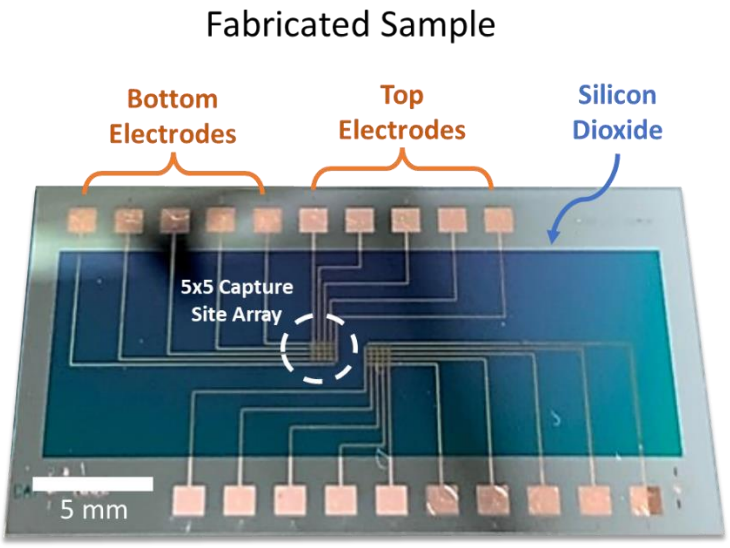

Figure 2-23 Picture of the fabricated device at chip scale. As can be seen, these devices have 5 bottom electrodes and 5 top electrodes to individually control each of the capture sites in the 5x5 array. This device has 2 5x5 capture site arrays totaling 50 capture sires per device and 20 electrodes to control them.

In this section, I will outline in detail the microfabrication procedure used to make our device **Figure 2-23**. In addition, I will describe some of the issues that were encountered during this process in hopes of making this fabrication process easier to replicate for future students.

1. Dice and clean silicon wafer

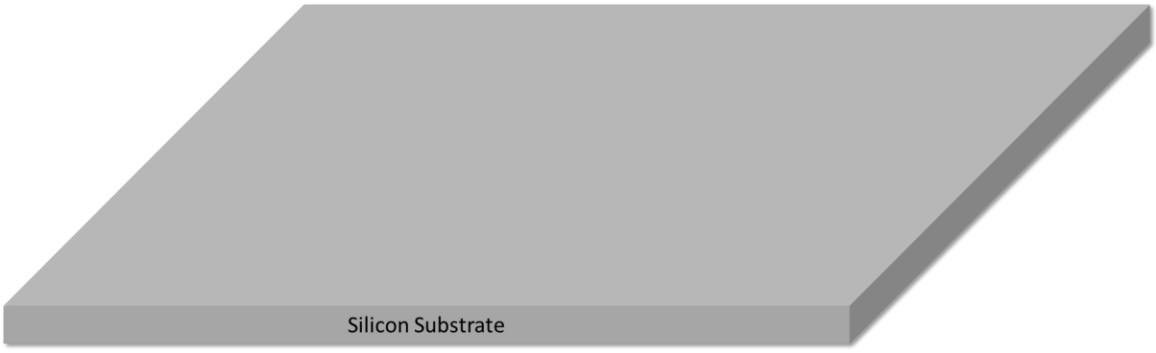

Figure 2-24 Bare silicon substrate

The silicon wafer piece must first be cleaned using acetone, methanol, and isopropanol to get rid of organic contaminants. The piece can further be cleaned with de-ionized water using an ultrasonic bath cleaner if desired. The piece is then dried with nitrogen.

2. Deposit and pattern bottom copper wires

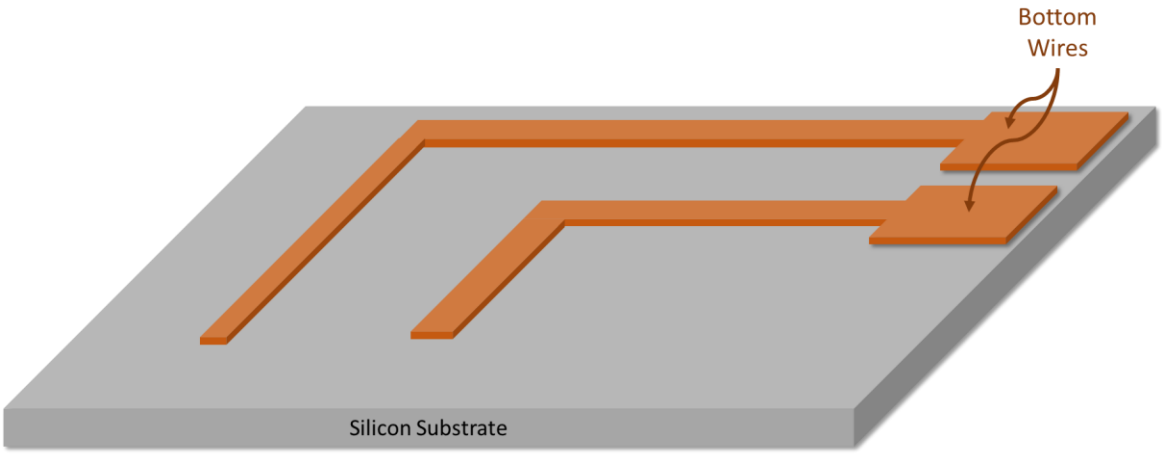

Figure 2-25 Deposition and patterning of bottom copper wires and electrodes

The first layer of electrodes is patterned using photolithography. The photoresist used was AZ nLOF 2020. The spin coating procedure was the following:

- Wafer dehydration at 100 C for 5 minutes
- HMDS Spin coat: 500 rpm spin (5s), 3000 rpm spin (60s)
- nLOF 2020 Spin Coat: 500 rpm spin (5s), 3000 rpm spin (60s)
- Soft bake: 110 C 1 min, 5 min cooldown
- Exposure: 5 seconds 10mW/cm^2
- Develop: AZ300MIF 90-120 sec with slight agitation
- Clean with water, not IPA

- Descum using Matrix Oxygen plasma asher 100W for 60 seconds.

Once the resist was patterned, the metal was deposited using e-beam evaporation. The deposited stack was Ti [5 nm] / Cu [500 nm] / Ti [10 nm]. Titanium was used as an adhesion layer because, without it, the internal stresses of the copper layer would cause the wires to peel off. The top layer of Titanium was used to prevent oxidation. The deposition rate was 3 Angstroms/s for all three layers. A faster deposition rate would cause the wires to peel off. Following this deposition, the piece was submerged in NMP at 80C for 4 hours with vigorous agitation to liftoff the resist. If this didn't completely liftoff the resist, then I would use the ultrasonic bath for around 10 seconds to completely remove the resist and improve the copper wire patterns. If the piece is left too long in the ultrasonic bath, you risk the copper peeling off from the silicon.

3. Deposit an insulating layer of SiO2 to separate the bottom wires from the top wires.

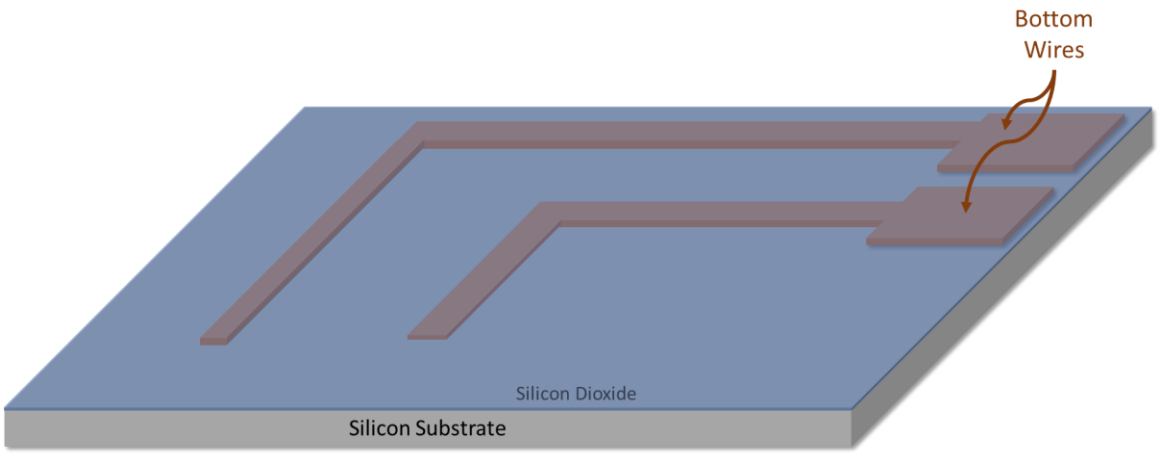

Figure 2-26 Deposition of insulating PECVD SiO2 layer

Above the first layer of wires, I deposited the insulating layer of SiO2 using the STS PECVD. The thickness deposited was 500nm. The thickness was verified using a Nanospec reflectometer.

4. Etch vias through SiO2.

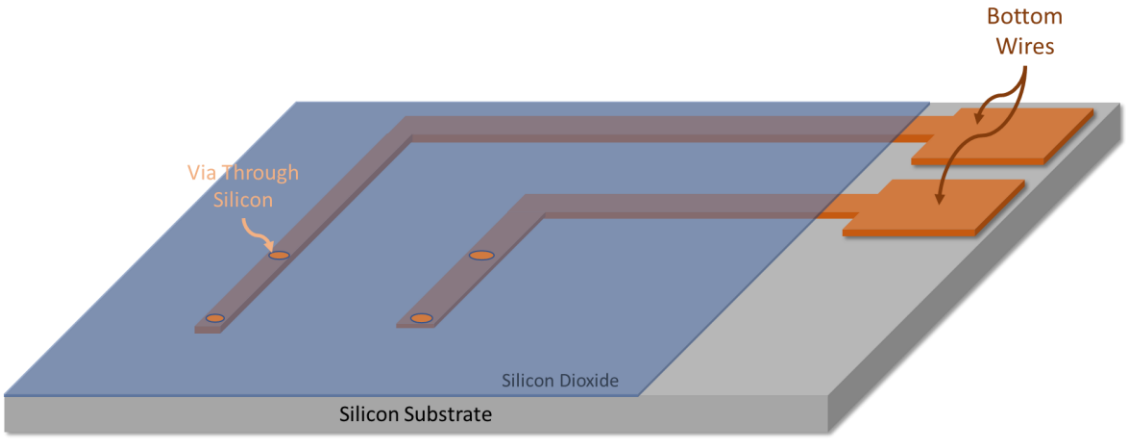

Figure 2-27 Via etch through SiO2 in order to expose bottom copper wires at specific locations.

In order to etch the vias through the SiO2, I first patterned the wafer using nLOF 2020 photoresist to act as an etching mask. Once patterned, the wafer was submerged in buffered oxide etchant (BOE) for 10 minutes with minimal agitation. This allowed the etchant to remove all the SiO2 at the via locations, successfully exposing the copper wires. After performing the etch, the resist etch mask was removed using NMP at 80C for 30 minutes, followed by a solvent clean to remove any unwanted contaminants.

5. Deposit and pattern top copper wires

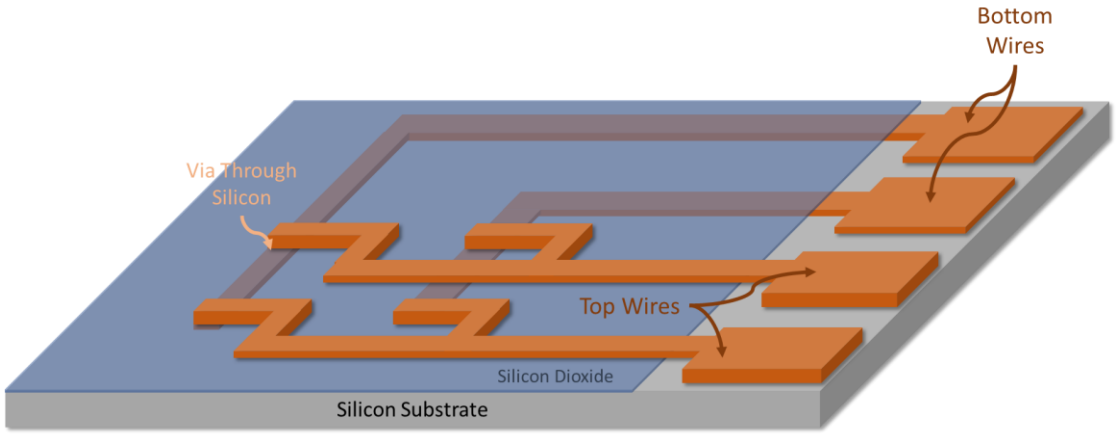

Figure 2-28 Deposition and patterning of top copper wires and electrodes.

Using the same photolithography and liftoff processes outlined in step 2, I patterned the top copper wire design. I then deposited the top copper electrodes with the following stack: Ti [5 nm] / Cu [1000 nm] / Ti [10 nm]. The copper was thicker in this layer so as to reduce the total wire resistance and allow for the maximum current to run through them. The titanium layers were used for the same reason described previously.

6. Deposit and pattern the magnetic capturing sites.

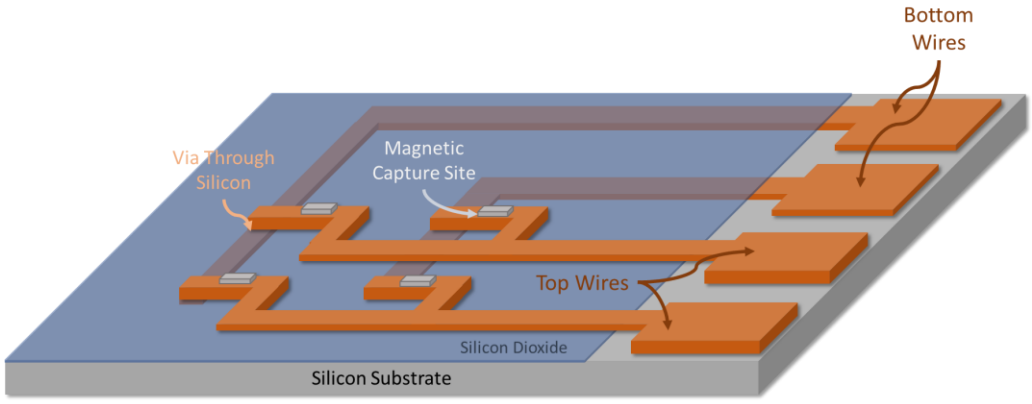

Figure 2-29 Deposition and patterning of small rectangular Iron capture sites.

The iron micromagnets were deposited and patterned using the same photolithography and liftoff processes described previously. The metal was again deposited using the CHA e-beam evaporation system. The deposited stack was Ti [5 nm] / Fe [120 nm] / Ti [10 nm].

7. Deposit top insulating layer of SiO2

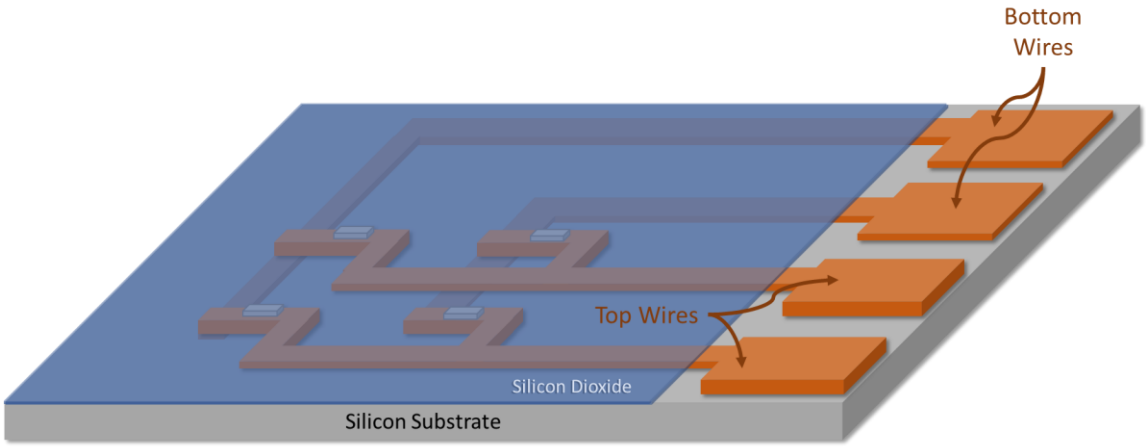

Figure 2-30 Deposition of the final insulating layer of SiO2. Etch performed to expose copper electrodes to allow for wire bonding.

The final passivating layer of SiO2 was deposited using the STS PECVD system. The SiO2 in this layer was 1 um thick. This thickness was chosen so as to completely cover the sidewalls of the copper wires and prevent any electrical contact between these wires and the fluid that would flow above them. Since this deposition covered the entire wafer, I had to perform a final etch to remove the oxide above the copper contacts, which were to be wire bonded to. This was performed using an nLOF 2020 resist etching mask, which was subsequently removed using NMP in the same way described above.

8. Bond PDMS microfluidic channel

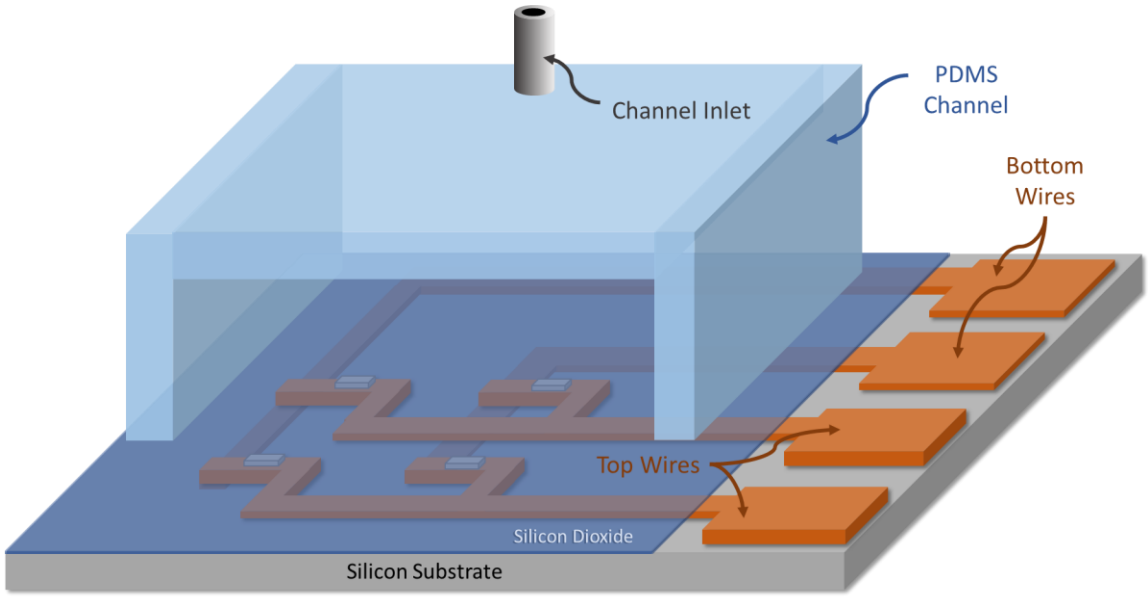

Figure 2-31 Bonding of PDMS microfluidic channel on to chip.

Lastly, the PDMS channel, which was previously poured and cured over a mold, was bonded to the SiO2 surface of the device using a standard oxygen plasma cleaning procedure. The inlets were then manually punched through the PDMS to allow fluid to flow within the channel.

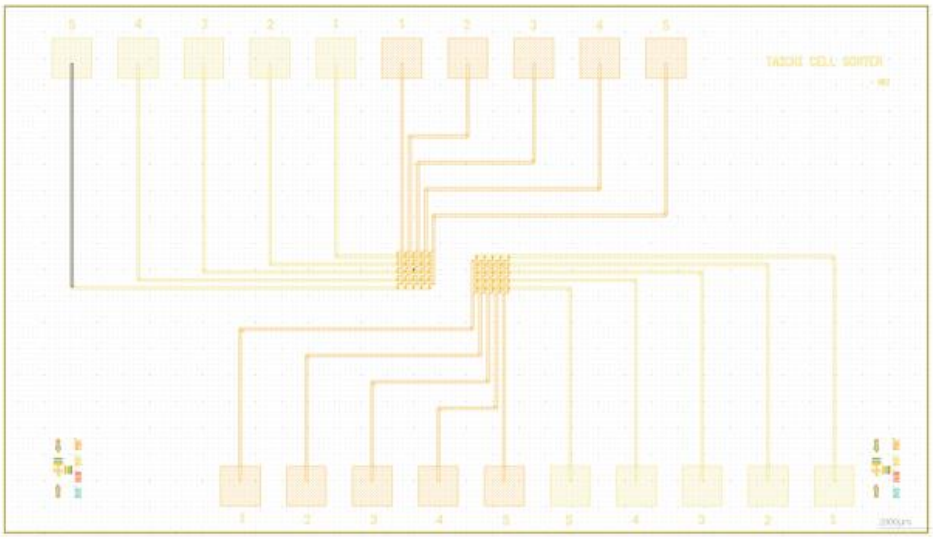

Figure 2-32 Photolithography mask used for the microfabrication of our single-cell capture and release platform. The mask shown above is composed of 6 different layers, one for each photolithography step.

2.4.4 Microfabrication Challenges

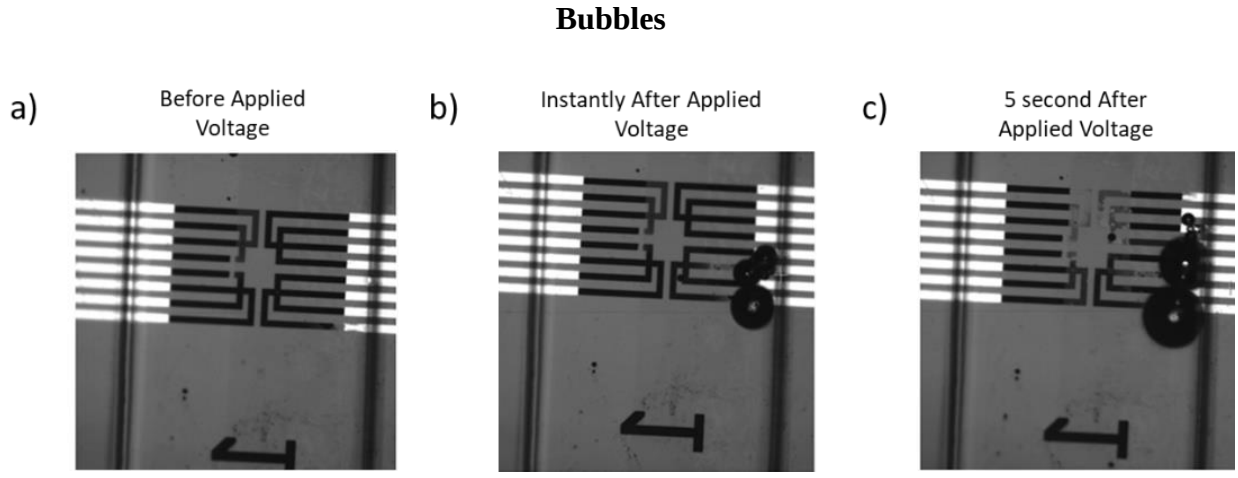

Figure 2-33 Testing issue with generation of bubbles within the microfluidic channel upon the application of current. (a)State of wires prior to running a current. (b) Immediately upon the application of current there are bubbles generated in the fluid directly in contact with the wires. (c) After 5 seconds of current application, one can observe the size of the generated bubbles has increased, and the color of other wires has changed. The other wires seem to be deteriorating.

This issue was first encountered in an earlier version of the device, as shown above. Every time we would attempt to run an electric current large enough to switch the magnetic state of the capture sites while simultaneously flowing liquid above the capture sites, there would be bubbles generated in the liquid. These bubbles would be quite large and would alter the flow of liquid within the microfluidic channel. This bubble generation would be accompanied by a deterioration of the copper wires and a large increase in their resistance. After much experimentation, we were able to deduce that this bubble generation was caused by two mechanisms. First, there was some sort of electrolysis happening that would cause the copper electrodes to deteriorate and generate hydrogen anytime there was a voltage put on them. This was evident due to the change in color of the electrodes. Second, the high current and high resistance from the small thin wires caused a large amount of joule heating to be produced. If the current ran too long, the liquid above the wires would boil. We discovered this by flowing ultrapure DI water in the microchannel, which theoretically should not allow any electrolysis to happen. When the current was run, in this case, the electrodes did not deteriorate, and the bubbles were not generated instantly. Rather, the bubbles required the current to run for a longer period, but eventually, they would be generated, and the wafer became noticeably hot to the touch. The issue of the bubbles was very serious, given the fact that they would instantly destroy the device upon the application of current.

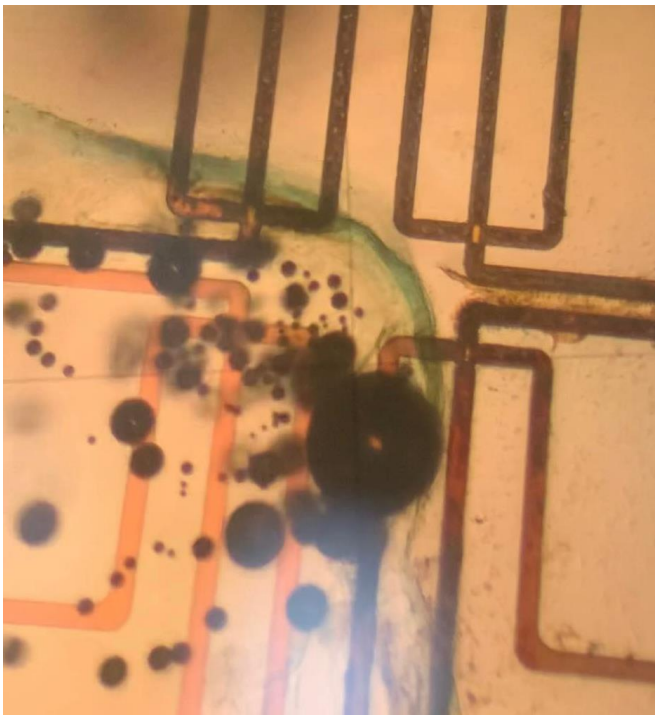

Figure 2-34 Color microscope image of the generation of bubbles in the liquid within the microfluidic channel upon the application of current. In this image, the current is being run through the bottom left set of wires. These wires do not seem to deteriorate. In contrast, the other three sets of wires appear to become darker. This appears as if there is some sort of electrochemical reaction between the electrodes and the fluid within the microfluidic channel. This observation is supported by the green liquid that seems to be coming off of the bubbles. This could be a product of the chemical reaction between copper and the liquid in the microfluidic channel.

To address this issue, we first decided to deposit a thicker insulating layer of SiO2 on top of everything to completely isolate the electric components from the fluid environment in the microfluidic channel. This worked well to prevent electrolysis seen; however, if the current was left running too long (~2 seconds), we would still observe the boiling effect described previously. This heat generation issue was more difficult to address because the currents required for magnetic switching were fixed and could not be decreased. We decided to lower the resistance of the wires by making them a lot thicker and wider. This reduced the total amount of joule heating produced

for a given current. Additionally, we realized that since the magnetic switching process occurs on the order of nano to microseconds, we could achieve our goal by running a very short current pulse. So instead of manually running a current by placing probes on the chip electrodes, we devised a system to run a very short current pulse with the magnitude needed to magnetize or demagnetize the capture sites. This current pulse was short enough to not allow enough time for any appreciable heat to be generated. With both the thicker SiO2 and the shorter current pulse, we were able to completely eliminate both the heat and bubble generation problems.

Metal peeling off.

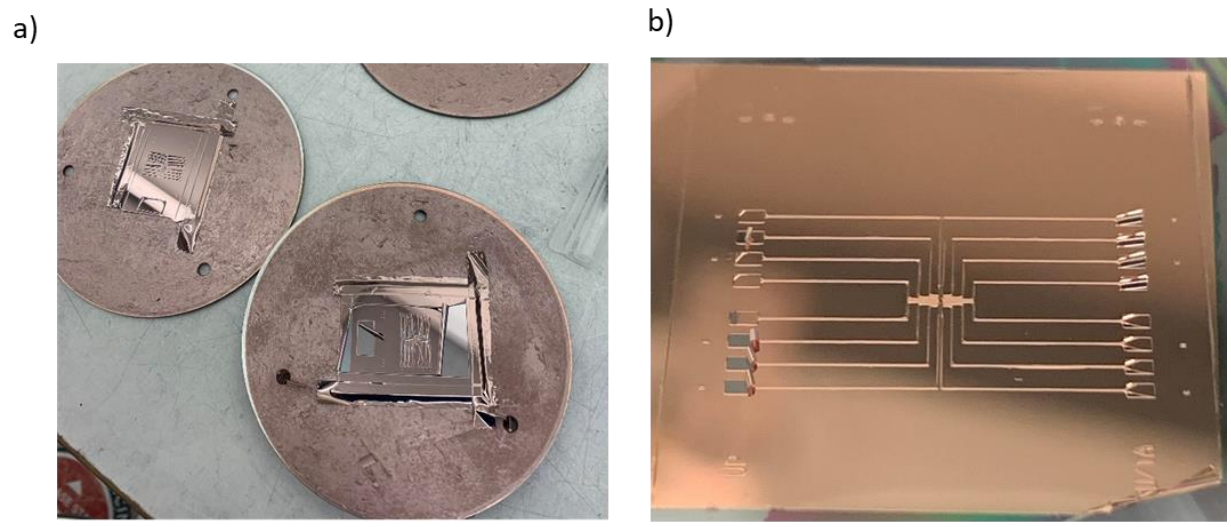

Figure 2-35 Experimental images of failed copper depositions. In these images, we can observe the copper has peeled off from the substrate. In the image on the right, it can be observed that the copper films have curled up upon themselves, leading us to believe that this was caused by high residual stresses. It was discovered that this was caused by attempting to deposit the copper with too high of a deposition rate. By lowering the deposition rate, this issue could be avoided.

After we decided to increase the thickness of the electrodes in order to reduce their electrical resistance, we found that the copper would peel off from the wafer after deposition. This

would occur regardless of what adhesion layer we were using, so it was evident that it wasn't a problem with the Titanium adhesion layer. After much trial and error, I discovered that the cause for the film peeling off after deposition was that the deposition rate was too fast. Given that the metal being deposited was very thick (1 um) relative to thicknesses normally deposited in an electron beam evaporation system, and I didn't want to wait an unreasonably long amount of time for the deposition, I increased the deposition rate. This change caused a large increase in the residual stresses during the deposition, and as the film got thicker, the stresses eventually overcame the adhesion between the titanium and the silicon substrate, and the metal would peel off. In order to remedy this problem, I decreased the deposition rate to 3 angstroms per second, which is slower than normal. This reduced the residual stresses significantly and eliminated the problem entirely.

Warped PDMS

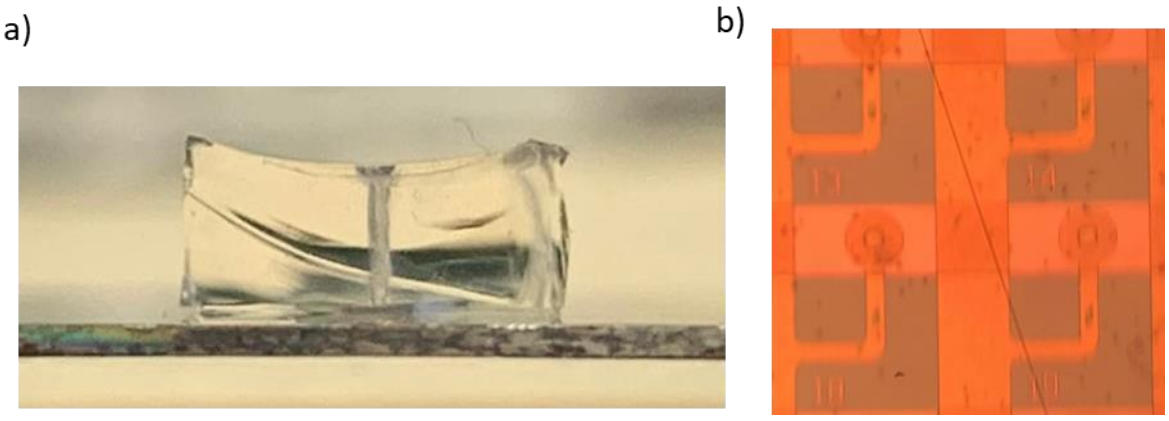

Figure 2-36 Experimental images of poorly fabricated PDMS channel. (a) Side view of the PDMS channel where it is clearly observed that the top surface is concave. This curvature was produced due to the PDMS mold being too small. (b) The effect of this curvature was that it optically distorted the images we could capture using the microscope, and since the PDMS bonding is irreversible, these devices were essentially rendered useless.

I noticed this issue after I had finished fabricating a new batch of devices, and I attempted to use them for an experiment. For some reason, I could not focus on the individual capture sites since everything looked blurry. I ended up figuring out that the cause for this optical distortion was that the PDMS channels that we were bonding onto the wafer were not flat. This occurred because our collaborators from the Di Carlo lab changed the channel pouring protocol and changed the mold to a smaller one in order to minimize the amount of PDMS poured. This smaller mold container resulted in a meniscus forming from the surface tension in the liquid PDMS, and thus when it cured, the microfluidic channel had a curved surface, and this distorted the images we could obtain through the PDMS. To remedy this, we just increased the lateral dimensions of the mold and allowed the PDMS to settle flatly without risking the creation of a meniscus. With this protocol, the cured PDMS channel was perfectly flat, and the images that could be obtained were not distorted. This allowed us to conduct our experiments and record videos unobstructed.

Electrical shorting (wire breakdown)

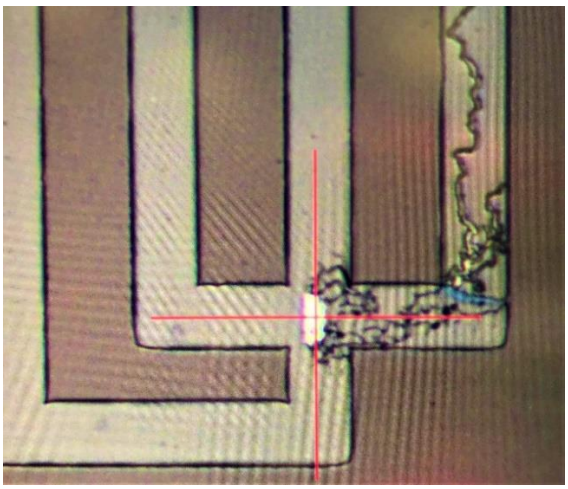

Figure 2-37 Microscope image of wire after the application of a voltage that was too large, and the wire burned out.

This problem occurred in earlier versions of the device where the wires beneath the capture sites were a lot thinner than those of the current device. Their reduced thickness caused their resistance to be very large, and thus to run an appreciable current through them, we had to apply a large voltage. If the voltage was too large, the wires would become damaged and would burn out, like in the image above. Once this happens, the wire will no longer be usable. To fix this issue, we just increased the thickness of the wire to reduce its resistance. This would allow us to run the same currents but with a much lower applied voltage. This reduced the chance of the wires breaking down.

Bad PECVD SiO2 Deposition

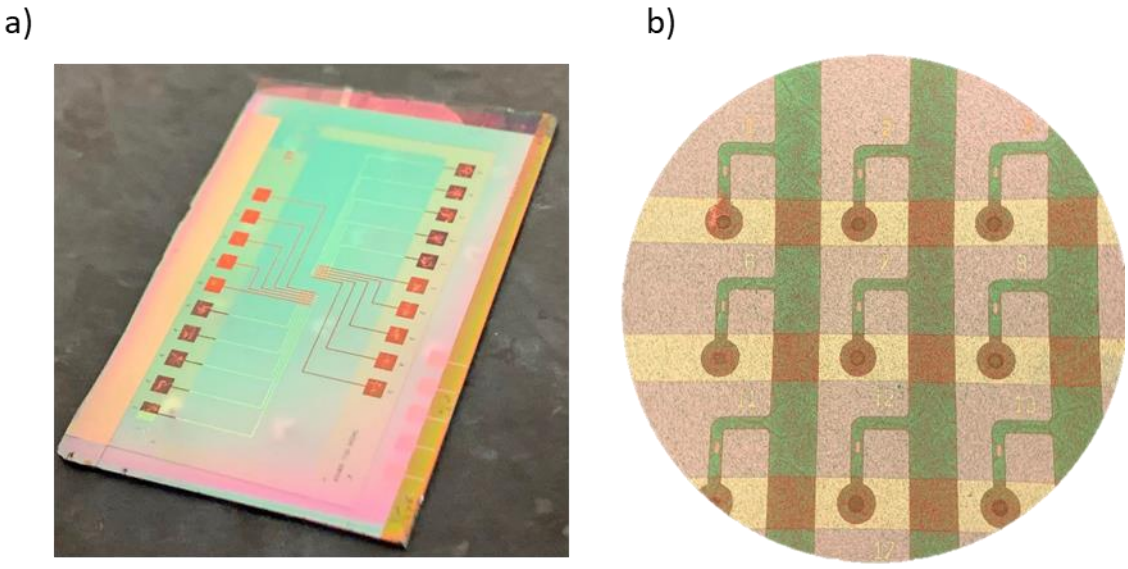

Figure 2-38 Images depicting a failed SiO2 PECVD deposition. (a) Although not immediately obvious, the color of the final SiO2 layer was cloudy due to having a deposition chamber that was not clean. (b) Microscope image showing the poor quality of the SiO2. The granularity shown is not typical of a PECVD oxide deposition.

As described in the microfabrication section, silicon dioxide was used in two different layers to both separate the top and bottom set of wires and to prevent the wires from interacting with the fluid environment in the microfluidic channel. This silicon dioxide was deposited using the STS PECVD deposition tool in the EIV cleanroom. If this tool had not been cleaned for a while, it would result in a poor-quality film deposited. This occurred because, during every deposition, the chamber itself becomes coated with layers of silicon dioxide or nitride, and this continues for as long as the machine is not cleaned. Eventually, this chamber coating becomes so thick that some of the silicon dioxide begins flaking off and ruins the deposited film. If the film was bad enough, you could see the film be cloudy and speckled. Whenever the deposited film would look like this, it would no longer insulate properly, and the device would no longer work since the top, and bottom wires would short through the silicon dioxide. In order to prevent this in future depositions, I had to run the cleaning process on the chamber.

2.5 Summary and Conclusions

In this work, we proposed a design for a magnetic microfluidic platform that allows users to capture single, magnetically labeled cells at discrete locations in an array configuration and to release them individually for downstream collection. The proposed capture-and-release process consists of magnetizing and demagnetizing small iron capture sites using highly localized magnetic fields produced by electric currents in a network of wires beneath the capture sites. To validate the proposed design, we used FEA to predict the attractive magnetic forces between the capture site and the labeled cells and then used these forces to simulate the dynamics of cell capture and release using a moving-mesh FEA model. We then experimentally measured the magnetic fields required to magnetize and demagnetize the proposed capture sites and modeled the currents

required to produce them. Once the design process was complete, we fabricated the device and tested the current-induced magnetization and demagnetization of the capture sites using MFM. Following this, we experimentally demonstrated the ability of our platform to capture superparamagnetic beads and release them individually. In summary, we experimentally demonstrated the ability of our platform to capture Jurkat cells labeled with 8.5 μm superparamagnetic beads and to subsequently release each one of the captured cells upon the application of a demagnetizing current.

The magnetization and demagnetization mechanism described in this work can be extended to much larger capture site arrays in order to analyze a clinically relevant number of cells. Furthermore, this platform can capture any cell that can be magnetically labeled, making it significantly more versatile than other single-cell capture devices that are designed to target one specific cell type. Additionally, in contrast to DEP and optical-based systems, where the electric fields and UV light can negatively affect cell viability, the labeling and magnetic fields used in our platform have a negligible impact on cell viability [39]. With these advantages over similar devices, our platform will facilitate the single-cell analysis procedures necessary to develop the next generation of therapies and will support the further development of fields like cancer and neurobiology research.

Chapter 3. Microfabrication of a 400 MHz Multiferroic Implantable Antenna

3.1 Introduction

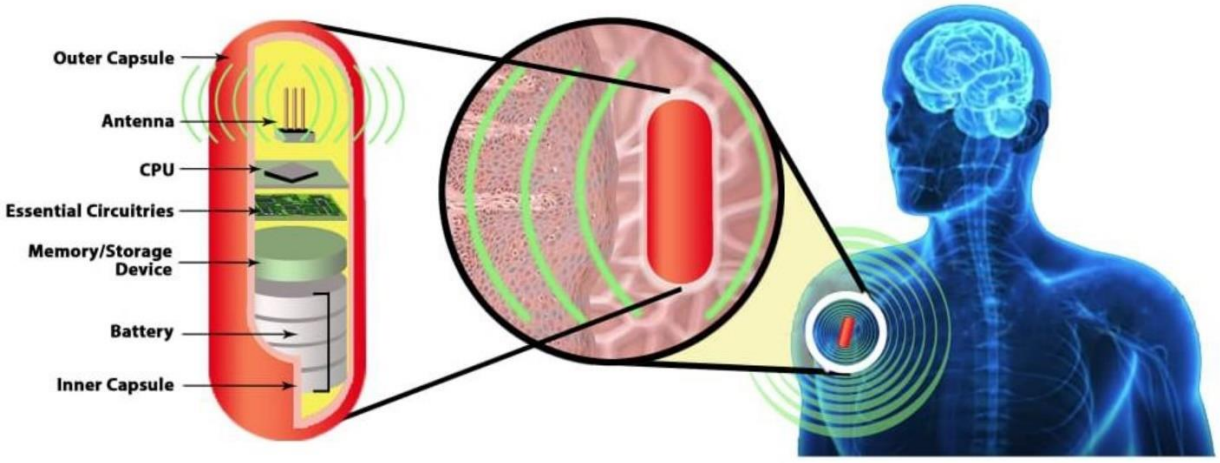

Figure 3-1 Schematic depicting possible implantable device with imbedded miniaturized antenna and other components. Adapted from [87]

Miniaturized antennas are of great importance for many applications. One application space that has garnered a lot of interest recently is that of implantable medical devices. Examples of implantable devices include pacemakers, cochlear implants, and insulin pumps. These implantable devices have to communicate with the outside world in order to share the data they're collecting. In the past, the implanted devices were powered and monitored by an external station via wired connectors, which posed a risk and hazard to the human body and required unavoidable surgical procedures. However, nowadays, most of these implantable devices use small antennas to transmit information. Over the last couple of decades, there has been a significant amount of research conducted on perfecting these miniaturized implantable antennas. This has proven to be quite challenging for the reasons outlined below:

1. Size constraint

The size of the antenna is critical in implantable devices, as the smaller the antenna, the less invasive the device will be. Smaller antennas also take up less space inside the body, which can be important in devices that are placed in areas where space is limited. Additionally, smaller antennas are less likely to cause discomfort or irritation to the patient, which is important for the long-term use of the device. Designing a small antenna is not easy, though, as you have to consider not only its design but also its fabrication process. As antennas get smaller, the fabrication processes needed to make them become significantly more complicated.

2. Biocompatibility

Biocompatibility is also a crucial consideration when designing a miniaturized implantable antenna, as the materials used to construct the antenna must not cause an adverse reaction in the body. This means that the materials should not be toxic, should not cause an immune response, and should not cause inflammation or irritation. They also should not cause any kind of chronic or acute effect on the body. The materials used in implantable antennas must also be able to withstand the harsh environment of the body, which includes exposure to bodily fluids, high temperatures, and pressure changes. They should be able to resist corrosion, erosion, and fatigue. These requirements make it difficult for researchers to find suitable materials and designs.

3. Efficiency

Efficiency is an important consideration when designing a miniaturized implantable antenna, as it relates to the power consumption and battery life of the implanted device. An efficient antenna will consume less power and extend the battery life of the device. There are several factors that can affect the efficiency of an implantable antenna, including the design of the antenna, its size, the materials used to construct it, and the operating frequency. Given that

implantable antennas are very small, they often suffer from electrical losses, which lower their efficiencies. For this reason, researchers are looking at finding new methods of electromagnetic wave propagation that mitigate these losses.

3.2 Multiferroic Antennas

One approach that aims to address some of the limitations of current miniaturized antenna technology is that of using multiferroic materials to create microscale mechanical antennas. Traditional antennas are limited in size by the wavelength of the EM signal they are designed to propagate. Due to efficiency losses, they typically cannot be any smaller than about a tenth of this wavelength. In contrast, multiferroic magnetoelastic antennas are designed based on the mechanical resonance of the structure rather than the EM resonance. Given that the mechanical wavelength is much shorter than the EM wavelength for a specific frequency, these multiferroic antennas can be made to be many times smaller than the smallest traditional antennas. In addition to this, these antennas have theoretically a much higher efficiency since they do not use electric currents but rather a voltage to generate the EM signals. As these antennas decrease in size, they do not suffer additional resistive losses.

As described in the introduction, these antennas are made of multiferroic composites consisting of a ferroelectric material and a ferromagnetic material mechanically bonded at their interface. By applying a voltage onto the ferromagnetic material, one can cause a mechanical deformation due to the piezoelectric effect. This deformation is then mechanically transferred onto the ferromagnetic layer that, as stated before, is mechanically bonded to the ferroelectric layer. By applying this deformation to the ferromagnetic layer, we cause the direction and magnitude of its magnetic moment to change. This effect is known as the inverse magnetostrictive effect or the Villari effect. This change in magnetization will then cause a change in the magnetic fields

surrounding the film. By applying this voltage in a sinusoidal fashion to the ferroelectric, we can generate a sinusoidal change in magnetic fields surrounding the device that can then propagate in free space. This is the general mechanism with which these multiferroic antennas function. It is important to note that this approach is also reciprocal, meaning that if instead of transmitting a signal, you want to receive a signal using this antenna, it can be done. In this case, the mechanism would instead be as follows: as the magnetic portion of the EM signal approaches the ferromagnetic material, this material begins mechanically deforming due to the direct magnetostrictive effect. This deformation would then be transferred onto the ferroelectric layer that is bonded to it, and this deformation would induce the generation of an electric charge in the ferroelectric material due to the piezoelectric effect. This generation of charge could then be measured as a voltage signal.

3.3 Proposed Design

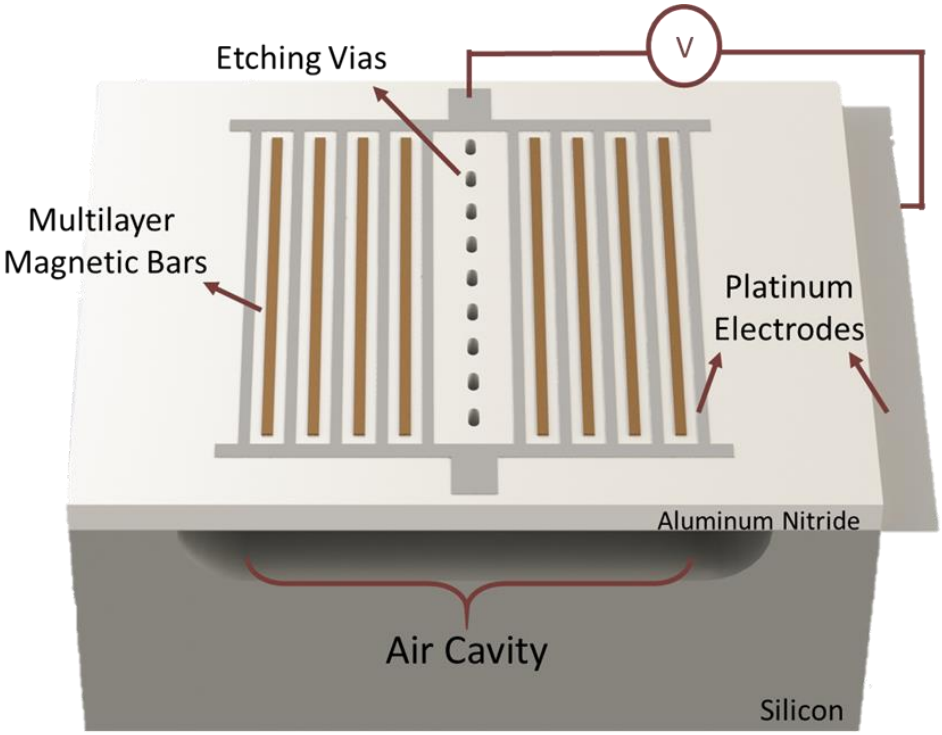

Figure 3-2 Schematic showing the design of our 400 MHz multiferroic antenna (not drawn to scale). Components included: Silicon substrate, a platinum bottom electrode, an aluminum nitride piezoelectric layer, platinum top interdigitated electrodes, magnetic bars, etching vias, and an air cavity. The voltage between the bottom platinum electrode and top electrodes is shown to demonstrate operation.

In this section, I will introduce our design for a 400MHz multiferroic antenna. In the following subsections, I will describe the design and role of each component, starting from the substrate and working my way through the fabricated stack. Some simulation examples will be used to better illustrate the operation of the device.

- Silicon Substrate

This device is built upon a silicon substrate. This substrate is solely used to provide us with a good structural foundation upon which to build. We do not use any of its semiconductor properties in our antenna operation. In our case, we opted for using high-resistivity silicon in order to reduce

the amount of parasitic currents that could be generated in the substrates since these parasitic currents contribute to loss and reduce the performance of the device. The silicon wafers used were 4 inches in diameter but were diced into smaller pieces to increase the number of devices that could be made without increasing the cost. The size of the silicon pieces after dicing was 22mm x 22mm. These pieces were large enough to accommodate multiple antenna designs and would allow us to test various parameters during the design process.

- Aluminum Nitride

The Aluminum Nitride film deposited above the silicon substrate is the ferroelectric component of our multiferroic antenna. As described previously, its main role is to deform under the application of a voltage mechanically. There are many materials that exhibit this necessary piezoelectricity, but Aluminum Nitride was chosen due to its many desirable properties, such as:

  - Piezoelectricity

    AlN is a ferroelectric material with desirable piezoelectric properties. AlN is a popular choice for piezoelectric actuators because it has a high piezoelectric coefficient, which means it can generate a large electrical charge for a given mechanical stress and vice versa. In our application, this is important because we want to be able to generate the maximum amount of deformation for a given applied voltage in order to deform the magnetic material better.

  - Desirable mechanical properties

    Aluminum Nitride's high elastic modulus, hardness, wear, scratch and tensile resistance to delamination, and substrate adherence make it a highly appealing material

for applications where mechanical reliability is of utmost importance, such as implantable medical devices.

- Biocompatibility

  Aluminum Nitride has been shown to be biocompatible and very chemically inert, which are, of course, highly desirable properties for a material to be used in implantable devices. Any material that has any likelihood of having adverse effects on a patient is immediately disqualified from the material selection.

- Low Cost

  Compared to other ferroelectrics with similar performance profiles, Aluminum Nitride is significantly more cost-effective. This is due to its ease of deposition using DC magnetron sputtering. All that is required is an Aluminum target and a source of nitrogen which are both relatively accessible.

In order to induce mechanical deformation in the AlN film, there must be an electric field applied through it. In our design, the electric field is generated by applying a voltage through the thickness of the AlN. In order to apply this voltage, we have two sets of electrodes, one beneath the AlN and one above it. The electrode beneath the AlN is a continuous platinum film (100 nm) upon which the AlN is grown. Above the AlN is the other set of electrodes, the design of which will be discussed in detail in the next subsection. By applying a voltage on these top electrodes and having the platinum bottom electrode be electrically grounded, you can generate an electric field through the thickness of the AlN, which will induce a mechanical deformation relative to the strength of the applied voltage.

In our design, the AlN film is 1 um thick. This is unusually thick for thin film devices such as our own. However, we chose this thickness to increase the in-plane load-bearing capabilities of the thin film in order to prevent any mechanical failure during operation.

The AlN films used in our devices were fabricated by a vendor at Carnegie Mellon University. We chose to outsource this deposition in order to prevent any inconsistencies in the fabrication, given the importance of this component.

- Top Electrode Bars

As discussed above, the electric field through the AlN nitride is generated between the bottom platinum electrode and the electrodes above the AlN. These electrodes above the AlN are not a continuous film, as was the case with platinum. Instead, these top electrodes are made with a finger-like or interdigitated geometry. The reason for this geometry is that it allows us to make a mechanically resonant structure at the specific frequency we desire. Given that our device is made to resonate with an in-plane vibrational mode, we can tune this resonant frequency by carefully designing the width of the electrodes and the spacing between them. It is important to note that the reason we wanted our device to be a resonant system is that at resonance, the mechanical deformations are maximized, and thus the magnetic signal that we can emit is greatly amplified compared to an off-resonance vibration. In our case, we wanted to design a device that operated at 400 MHz, so in order to achieve the greatest mechanical deformation at this frequency, we carefully designed the electrodes to achieve piezoelectric resonance at this frequency. The final dimensions of the electrodes were chosen to be 5.4 um wide with a 16.2 um spacing between them. The number of bars per antenna and the length of these electrodes did not play a significant role in the resonance behavior, but they were important for other reasons. The length of these electrodes

dictated the length of the magnetic bars we would place between them and, therefore, the amount of magnetic material we could have per antenna. This amount of magnetic material is directly correlated with the amount of magnetic signal we can get from our antenna, so one would expect it would be necessary to maximize the length of these electrodes. However, after a certain length, the voltage signal applied on the electrodes decays, and any further material beyond that point is useless. Taking this into consideration, the length of the electrodes was chosen to be 1000 um. In a similar fashion, the number of electrodes placed side by side dictates the number of magnetic bars we can place between them and, therefore, the amount of magnetic material we can have per antenna. So again, one would expect that we should maximize the number of electrodes. However, as the number of electrodes increases, the electrical impedance of the system also changes, and this affects the coupling between the electrical and mechanical mechanisms. Taking this into account, we decided to use 32 electrodes, as this had been shown in our simulations to work well. The 1um thickness of the electrodes was chosen in order to minimize the resistive losses that could be experienced. A thicker set of electrodes may be more beneficial, but due to fabrication limitations, we were limited to around 1 um. Finally, the material chosen for these electrodes was Aluminum due to its desirable electrical properties and ease of deposition. Originally, the design included gold electrodes, but due to fabrication issues and high cost, we switched to aluminum which also has a high conductivity.

- Magnetic Bars

The next component of the antenna is the magnetic bars. The role of the magnetic bars was to get deformed by the piezoelectric deformation of the AlN. This induced deformation would change its magnetic state, and this change in magnetization would then change the magnetic fields surrounding the structures. These perturbations in the magnetic field would then travel through

free space and could be detected by a receiver somewhere else. The geometric design of these magnetic bars was guided principally by the design of the electrode bars. The dimensions of the magnetic bars, with the exception of the thickness, had to match the dimensions of the electrodes exactly. The reason for this was that in order for the bars to mechanically resonate at 400 MHz, their dimensions and spacing had to be identical and periodic. For this reason, the width of the magnetic bars was 5.4 um, and the spacing between each other was 16.2 um.

To better understand the design of the magnetic bars, I will describe the mechanism of their deformation. When a positive voltage is applied to the electrode bars, this will cause the AlN to deform beneath them by expanding out of plane. This out-of-plane expansion will cause the AlN in the space between the electrodes to stretch in-plane. In the same way, when you put a negative voltage on the electrodes, the AlN will compress out-of-plane. This will make the AlN in the space between the electrodes compress in-plane. If you then put magnetic bars in this space between the electrodes and you alternate the voltage that you apply on the electrodes, you can subject these magnetic bars to alternating in-plane compression and tension. Due to the magnetostrictive effect, these alternating stresses will cause an alternating change in magnetization. To better illustrate the mechanism, I've added the diagram below:

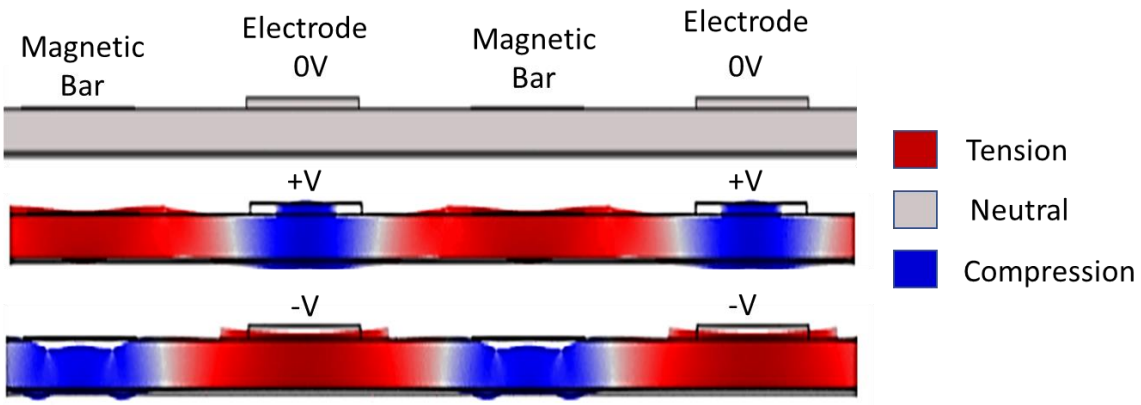

Figure 3-3 Simulation results depicting the different deformations produced by different applied voltages on the electrodes. The graphic shows two electrodes and two magnetic bars. The magnetic bars are much thinner than the electrodes, so they are not easily discernable. It can be seen that before the application of voltage, the AlN is unstrained. Upon the application of a positive voltage on the electrodes, there is a tensile strain produced at the AlN region supporting the magnetic bars. Similarly, upon the application of a negative voltage, the region between the electrodes is under compressive strain. These alternating strains applied onto the magnetic bars are what cause its magnetic state to change and thus produce an electromagnetic signal.

The material chosen for the magnetic bars was FeGaB due to its favorable magnetic properties and its previous use in similar devices. FeGaB has a relatively high magnetization and a very low coercivity which means that any magnetic switching that occurs does not require a lot of energy input. Additionally, FeGaB has high magnetostrictive coefficients, meaning that the magnetization will change easily with an applied stress. It is important to note that in previous iterations of the device, we had used other materials for the magnetostrictive bars, such as Nickel and a FeGa/NiFe multilayer composite. Nickel was eventually discarded as a candidate for the material due to its poor magnetostrictive performance and its high coercivity. On the other hand, the multilayer composite was a very promising material candidate. However, this material required a much more involved deposition procedure that, unfortunately, was not able to be continued due to an equipment failure. This multilayer composite had similar or ever better properties compared to the FeGaB material chosen. The FeGaB material chosen was deposited by some collaborators at Northeastern University due to their familiarity with this material and their expertise with the

deposition tool. It is important to note that their deposition method included an in-situ magnetic field that was used to deposit a film that had an inherent magnetic bias in a particular direction. In our case, we chose a 45-degree magnetic bias direction in order to ensure that the magnetization would rotate coherently during the application of this alternating stress. Ensuring the coherence of the magnetic rotation was important in order to obtain the maximum amount of magnetic signal possible.

- Air cavity

The final component of the antenna is the air cavity beneath the AlN. This air cavity is created by removing the supporting silicon upon which the antenna is built. By removing this silicon, we allow the AlN to deform more freely, thereby drastically increasing the amount of stress and strain that can be developed in the AlN and magnetic bars. If this silicon were not removed, then the AlN film would be mechanically clamped on the resonant behavior and would be almost completely eliminated. The width of the cavity is made to be as close as possible to the width of the antenna. Additionally, this air cavity helps contain the elastic energy within the AlN since the drastic difference in material properties at the interface of the AlN and air causes energy to be reflected.

3.4 Microfabrication Process

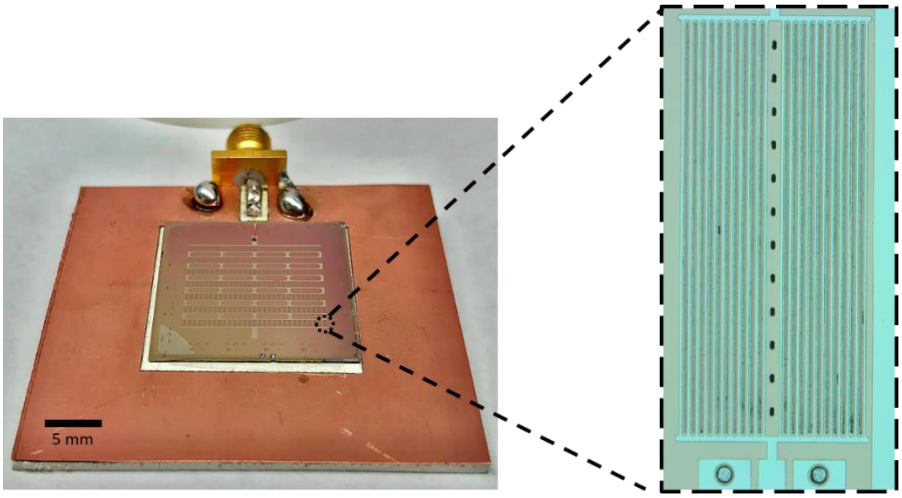

Figure 3-4 Image of one of our earlier antenna designs where each chip included around 200 individual antennas. The image on the right shows one such antenna. In this design, the antenna array was fed through wire bonding the top electrodes to an SMA connector.

In this section, I will describe in detail the microfabrication process used to make our device.

1. Wafer Cleaning

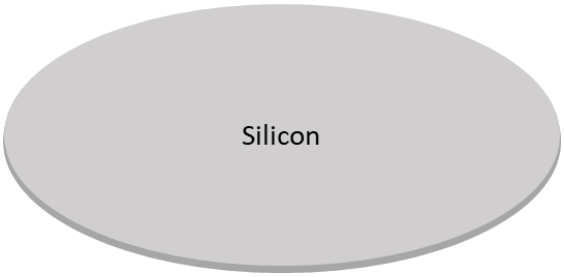

Figure 3-5 High-resistivity 4-inch silicon wafer

The devices are built upon a 4-inch, high-resistivity, p-type Silicon wafer. Prior to processing, the wafer is cleaned using acetone, methanol, and isopropanol to remove any organic contaminants. The wafer is then washed with deionized water and dried using nitrogen. High resistivity silicon was used to minimize the effect of parasitic currents generated in the substrate.

2. Pt/AlN Deposition

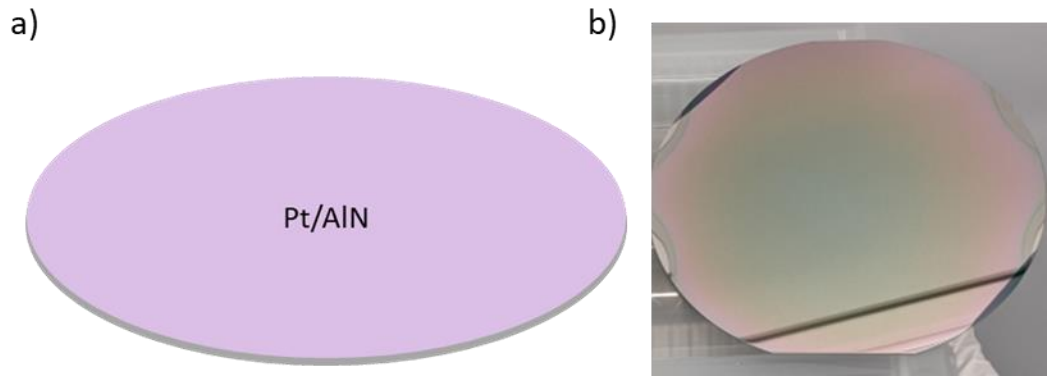

Figure 3-6 (a) Silicon wafer with a platinum electrode and aluminum nitride layer deposited. (b) The image on the right shows an example of a newly deposited wafer from our vendors at Carnegie Mellon University.

The wafers were then sent to Carnegie Mellon University for deposition of the piezoelectric Aluminum Nitride Film. In order for the Aluminum Nitride to grow with the correct crystallographic orientation, the films had to be grown on platinum. This platinum also acted as the bottom electrode layer for the device. The stack deposited was the following: Ta / Pt (100 nm) / AlN (1 um). Tantalum was used as a thin (~3 nm) adhesion layer. Both the Tantalum and the Platinum were deposited using e-beam evaporation. Subsequently, the Aluminum Nitride was sputter deposited using an Aluminum target in a Nitrogen environment. The quality of the Aluminum Nitride was verified using XRD, and the residual stresses of the film were also carefully tuned so as to avoid the film buckling during the silicon release step.

3. Wafer Dicing

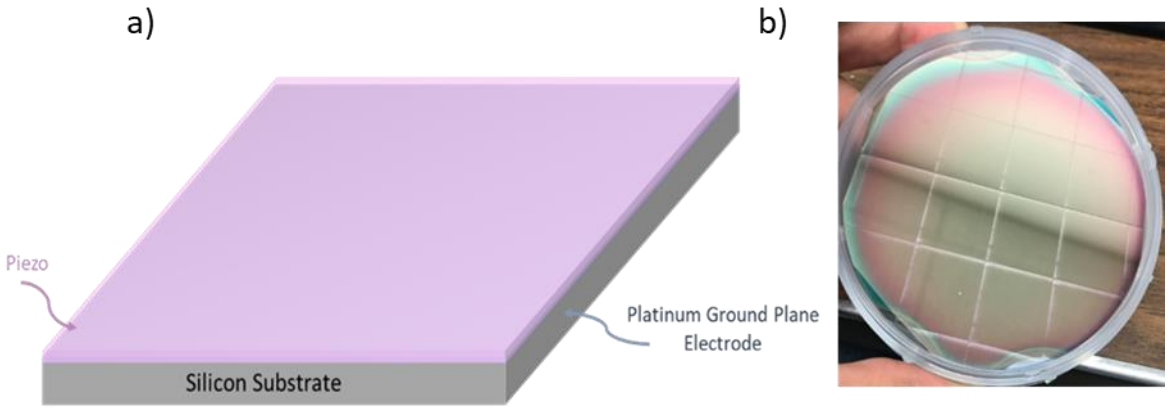

Figure 3-7 (a) Diced wafer into 22mm x 22mm square pieces. (b) Experimental image of a diced wafer

Once the wafers were shipped back, we diced them into 22 mm x 22 mm square pieces. To perform this dicing, the wafer was first coated with a protective layer of AZ5214 photoresist which was just spin-coated and prebaked at 100C for 1 minute. This layer of photoresist prevented Silicon dust from redepositing on the AlN surface during the dicing process. After the dicing process, the photoresist was removed by cleaning each piece with acetone, methanol, isopropanol, and DI water and dried with Nitrogen.

4. GSG Via Etching

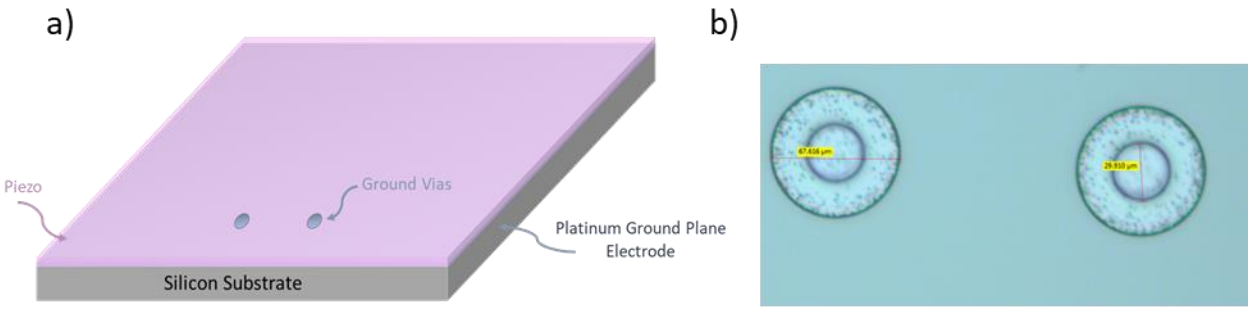

Figure 3-8 (a) Schematic of vias etched through AlN film down to the platinum bottom electrode (b) Experimental image of successful etch. In this image, we can observe two concentric circles for each etching site. The smaller circle is the photoresist layer which acts as the etching mask. The larger circle is the portion of AlN that was removed after a 10-minute AlN wet etch.

The first layer to be patterned was that of the ground vias used to connect ground pads to the bottom platinum electrode layer. This procedure was done using standard photolithography. The photoresist used in this process was KMPR1005 due to the fact that its developer (SU8 Developer) did not etch AlN, which cannot be said for the other commonly used photoresists (nLOF 2020, AZ5214). The photolithography process used here was the same for all subsequent layers, so I will outline the process here in detail:

- Clean piece with acetone, methanol, and IPA and dry with N2
- Dehydration bake at 150 C for 15 minutes on a hotplate
- Cool down for 5 minutes
- Spin coat KMPR1005
    - Ramp: 100 rpm/sec; Speed: 500 rpm; Time: 5 sec
    - Ramp: 300 rpm/sec; Speed: 4000 rpm; Time: 30 sec
    - Ramp: 300 rpm/sec; Speed: 0 rpm; Time: 0 sec
- Hot plate pre-exposure bake to remove solvents in photoresist
    - 100 C for 5 minutes
- Exposure (this time has to be recalibrated if the photoresist has been sitting at room temperature for too long (months). Typically, the exposure dose will decrease as the photoresist ages)
    - 6.1 seconds @ 12mW/cm^2
- Post-exposure bake
    - 100 C for 2 minutes
    - The pattern should become visible at 1 minute

- Photoresist Development
    - Submerge in SU-8 developer for 9 minutes
    - Place pieces upside down in a large beaker using a wafer cassette with a stirrer at around 300 rpm
    - Spray wash with SU-8 developer for 10 seconds
    - Spray wash with IPA for 10 seconds
    - Dry with N2 gun
- Measure feature size using Dektak profilometer and adjust exposure dose as needed. The development time will not significantly affect the size of the features since this resist is very thick. However, even a slight change in exposure dose will significantly affect the final feature size. Oftentimes, a feature may appear fully developed, but since the photoresist is so thick, it is impossible to accurately tell if all of the photoresist has been successfully removed from the trenches. This can cause liftoff procedures to fail due to the photoresist remaining where it should no longer be.
- Optional: Photoresist Stripping
    - Use NMP @ 80 C with vigorous agitation (stirrer at 1000 rpm)
    - Time depends on whether the photoresist has metal deposited upon it, as is the case with liftoff procedures. In these cases, the photoresist stripping can take upwards of 5-10 hours. If there is no metal on the photoresist or if the metal is very thin, then the liftoff is much quicker (1-2 hours)
    - Often times you may need to use ultrasonic cleaning to remove the photoresist fully

- You can also use the oxygen plasma stripping with a power of 250W for 1 minute to remove the resist completely, but this runs the risk of oxidizing whatever metal you have deposited on your wafer.

Once the via pattern is made using the photolithography process outlined above, the piece is submerged in the AlN etchant. In this case, we use AZ300MIF to etch through the AlN all the way down to the Pt bottom electrode. This process varies with the amount of agitation used and how good the photoresist development was during the photolithography. With minimal agitation, this process takes around 10 minutes. After the etch is completed, the AlN at the via locations should be mostly removed, it may look a bit speckled, but it should be enough to create good contact with the ground plane. The photoresist is then used as the etching mask is removed by submerging the piece in NMP at 80C for about an hour. If the resist has not been completely removed, you can use the ultrasonic bath or oxygen plasma stripping procedure to completely remove it. This oxygen plasma procedure can only be done at this step because, in subsequent steps, you risk oxidizing your metal films.

It is important to note that during the photolithography step for the via pattern, the photomask must be very clean as any bit of dust will result in small unwanted vias being etched on the surface of the AlN, which can cause the device to short at unwanted locations.

5. Electrode Deposition and Patterning

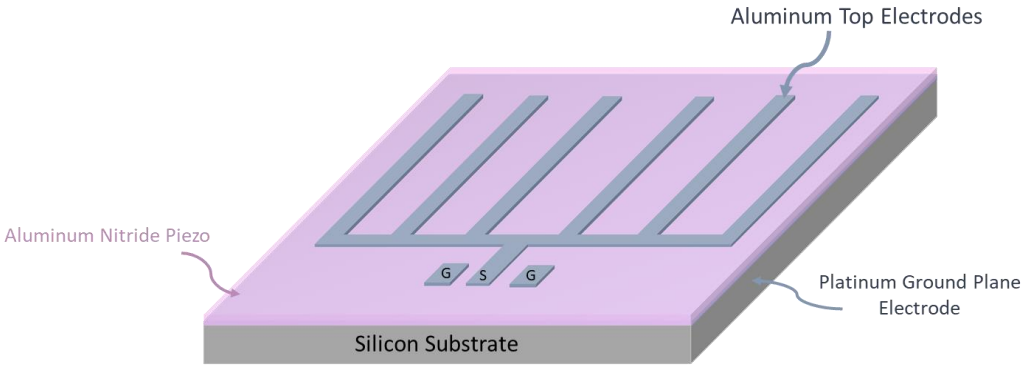

Figure 3-9 Deposition and patterning of top aluminum electrodes on top of the aluminum nitride layer. The pattern includes two ground pads that are deposited above the vias etched in the previous step. This was done to be able to feed the antenna using a GSG probe instead of wire bonding to minimize the losses.

Next, we use the photolithography process described above to make the top electrode pattern. Once the photolithography is done, we deposit the top electrode material using the CHA e-beam evaporation system. Prior to the deposition, the piece is descum using the Matrix oxygen plasma asher using 80W for 1 minute and baked on a hotplate at 100 C for 1 minute to remove any moisture from the surface and improve adhesion of the deposited metal layer. The stack deposited is Ti (5 nm) / Al (1 um) / Ti (10 nm). The titanium layers are used as both adhesion layers and protective layers to prevent oxidation.

Once the deposition is complete, the piece is submerged in NMP at 80C to strip the resist as described previously. The process can take 5-10 hours. Once most of the metal has been removed, the piece can be placed in a beaker with DIW within an ultrasonic bath for 10 seconds to remove any residual photoresist. This final step is quite delicate as too much time in the ultrasonic bath can lead to the metal peeling off from the AlN surface and ruining the device.

6. Magnetic Bar Deposition

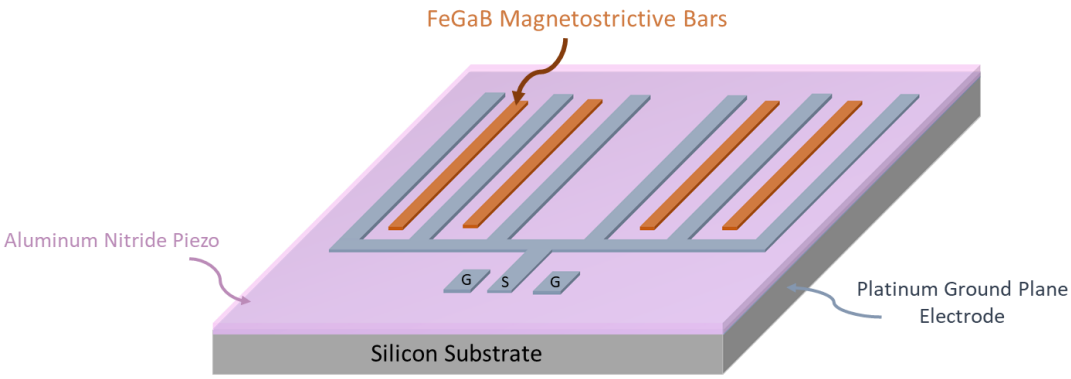

Figure 3-10 Deposition and patterning of FeGaB magnetostrictive bars

Following the exact same photolithography process described above, we then pattern the magnetostrictive bar pattern. We then sent the pieces to Northeastern University to have the pieces deposited with the magnetostrictive material stack. The material was deposited using a sputtering system with an in-situ magnetic bias to control the magnetic properties of the deposited magnetic material. The stack deposited was Cr / [FeGaB (45 nm)/ SiO2 (5nm)]$_{x9}$ / FeGaB(45nm)/Al. The Cr was used as an adhesion layer because it can lower the magnetic coercivity of the deposited magnetic material. The interlayers of insulating SiO2 were used to reduce eddy current losses in the magnetic material. Ultimately, the Al top layer was used to prevent oxidation.

After the deposition, the pieces were sent back to us. I performed the liftoff in the same way as with the Al electrode layer described above. The main difference with this liftoff procedure was that since this metal was sputter deposited and was very thick, the stripping of the resist took a lot longer than with the evaporated metal. This is to be expected since e-beam evaporation is a lot more directional and results in a less conformal metal film, whereas sputtered metal is more conformal and covers the sidewalls of the resist. This limits how fast the NMP can strip off the KMPR1005 photoresist. This resulted in the liftoff taking about 10-12 hours in heated NMP to

remove most of the unwanted metal. We then had to use the ultrasonic cleaner for about 30 seconds to completely remove all of the unwanted resist from the AlN surface.

7. Via Etching

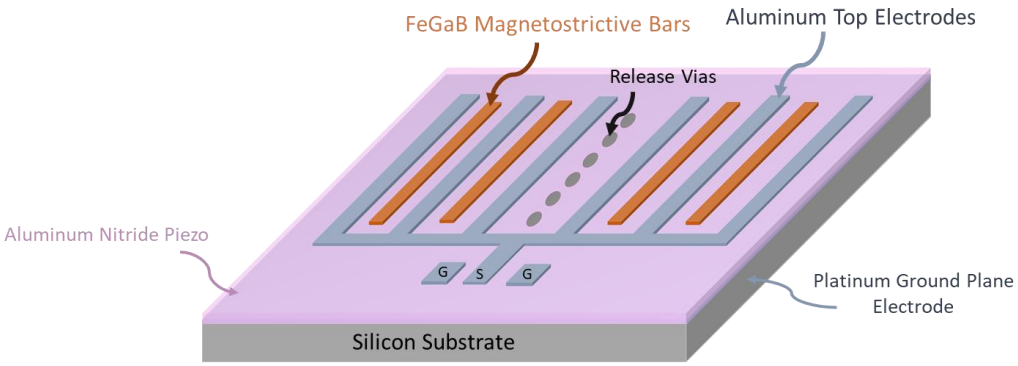

Figure 3-11 Release via etching through aluminum nitride and platinum layer down to Silicon

The next step was to etch vias through the AlN and through the platinum bottom electrode all the way down to the silicon wafer. To do this, we first made the etching mask using the same photolithography process described in the previous sections. Once the release via pattern was successfully made, we proceeded to etch through the AlN and the Pt layers using Cl2 plasma RIE etching. This process was conducted using RIE so that the etching was vertical and no isotropic etching occurred. This process was carefully tuned so that the etch would completely remove the AlN and the Pt layers exposing the bare silicon substrate without completely removing the photoresist. If the photoresist was completely removed, then we risked etching parts of the metal and AlN, and that would destroy our device. The final etch process was comprised of 2 etching steps: The first one was a 3-minute etch followed by a 5-minute cooldown, and the second etching step was a 3-minute and 10-second etching step and this cool down period prevented the heat generated by the plasma from hard baking the photoresist. It is important to note that in order to

place the devices in the RIE etching tool, the pieces had to be mounted on a silicon wafer with a thick oxide on it. This was because if we mounted it on a bare silicon wafer, the etching of the silicon would result in a lower etching rate and would also cause the etched silicon from the mounting wafer to redeposit on top of the photoresist making it hard to remove in the following step. Additionally, the device pieces were mounted onto the SiO2 wafer using thermal paste to prevent the pieces from heating up too much during the etching process and hard baking the resist. Hard-baked KMPR1005 becomes nearly impossible to remove using NMP, even with the ultrasonic bath.

After verifying the etch depth using an optical microscope by observing the etching vias turn dark gray (the color of the silicon substrate) as opposed to the white AlN or Pt, we proceeded to remove the etching mask by stripping the resist using the same NMP procedure outline before. Due to the heat and high energy of the plasma during the RIE etching process, the KMPR1005 photoresist surface becomes harder and thus becomes more difficult to remove using NMP. This resulted in the photoresist stripping taking about 12+ hours in heated NMP. This would sometimes not be enough to completely remove the photoresist, and I would use the ultrasonic bath for periods of up to 5 minutes to remove the residual resist. This, again, was difficult because it would often damage the existing metal structures on the AlN. It is also important to note that you cannot use oxygen plasma stripping to remove this resist because it will lead to the oxidation of the top Al electrodes and the FeGaB magnetic bars.

8. XeF2 Silicon Release

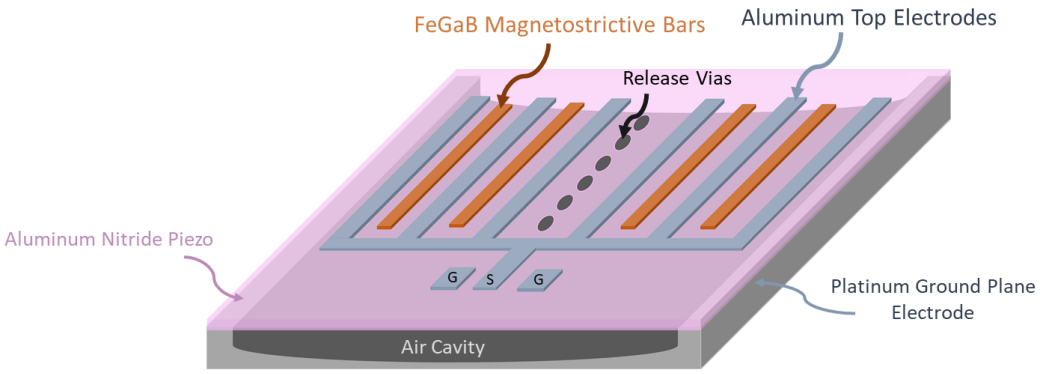

Figure 3-12 Silicon beneath antenna removed using XeF2 dry etching.

To finalize the device, we had to remove the silicon layer supporting the device in order to create a free-standing membrane. To do this, we used XeF2 dry etching to etch the silicon beneath the AlN through the release vias previously etched. The etch was performed in a small XeF2 etching chamber. To completely etch the silicon supporting the device, we performed an etch consisting of around 80 60-second cycles of XeF2 at a pressure of 2500 mTorr. After each cycle, the chamber would refill with new XeF2 to allow the etch rate to remain constant and not be reaction limited. It is important to note that the wafer piece had to be taped around its perimeter so as not to allow the XeF2 to etch the side walls of the chip. If not properly done, this would cause the etch rate to decrease drastically, and it would damage the structural integrity of the chip. In other words, the etch had to only occur within the etching vias previously made. This taping was done with Kapton tape since it did not interact with the XeF2 environment in the chamber.

In order to verify whether the etch was complete or whether more etching cycles were required, I scanned the surface of the device using a Dektak profilometer to determine which areas of the chip no longer had supporting silicon beneath it. In these areas, without silicon, the AlN surface would deflect downwards with the force of the scanning tip, whereas in supported areas, this would not

happen. This was done because the AlN and Pt layers were opaque and thus would not allow me to determine how large of an area had been etched beneath the device.

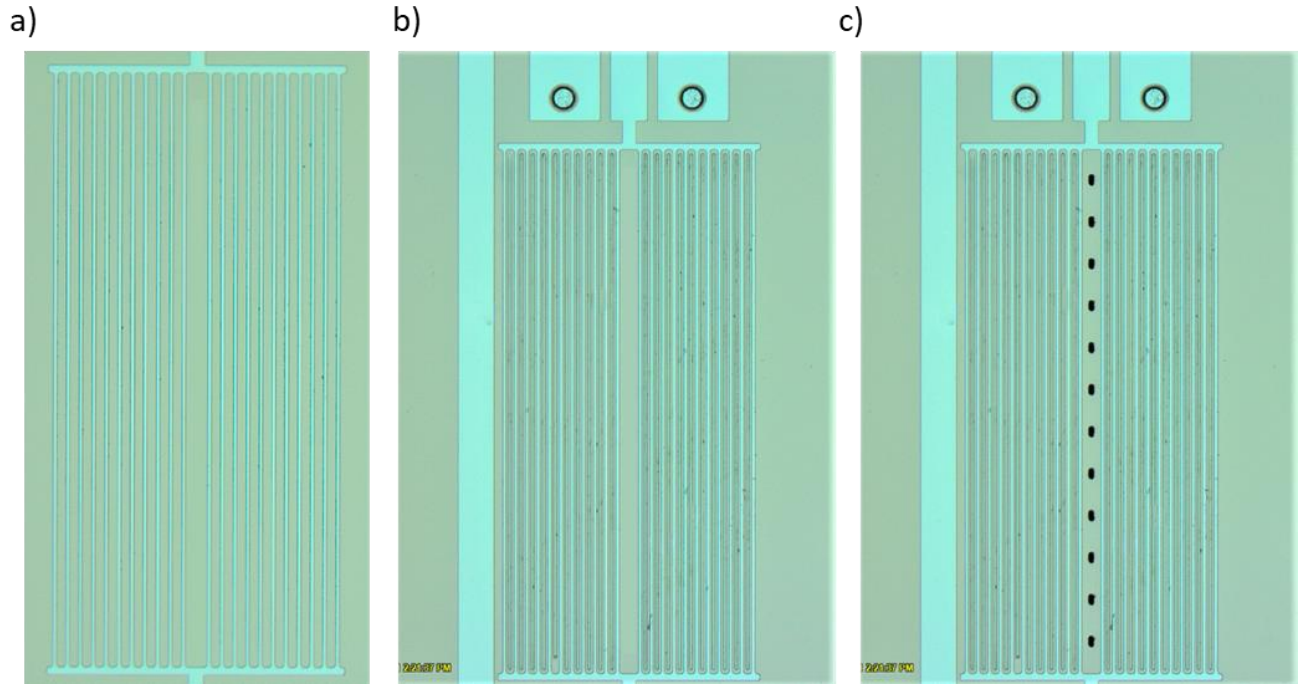

Figure 3-13 Experimental images of fabrication process results. (a) Deposition and patterning of electrodes. (b) Deposition and patterning of magnetic bars. (c) Vias etched through AlN and Pt and silicon below antenna removed (not visible).

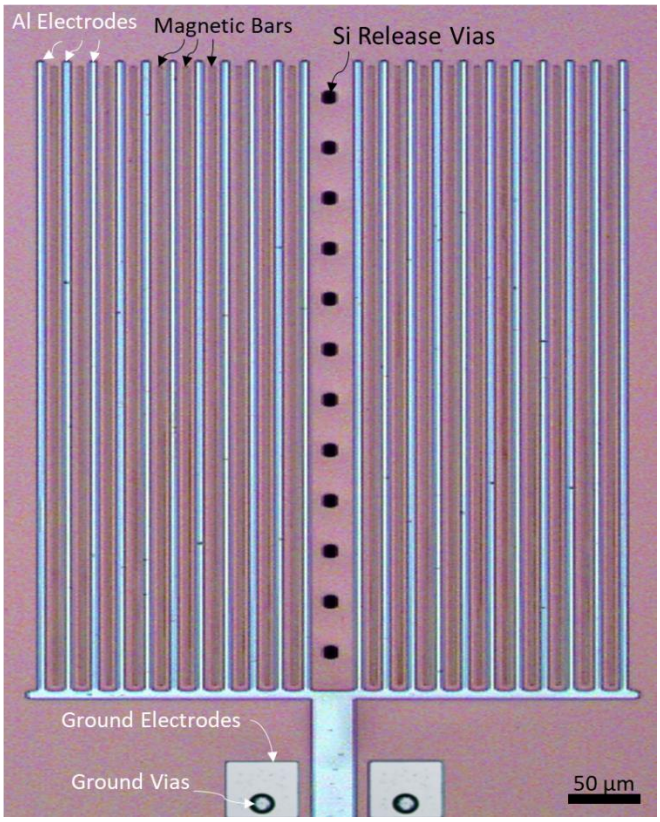

Figure 3-14 Microscope image of a successfully fabricated antenna with components labeled.

3.4.1 Microfabrication Challenges and Further Details

When I was selected as the microfabrication engineer on this project, I was given a short set of instructions by a recently graduated colleague that were supposedly the steps to fabricate the device. However, as I soon found out, those instructions were very limited and were mostly incorrect. Due to this, I had to redesign the entire fabrication process, and while doing this, I encountered many challenges and setbacks. The following are some examples of some of the difficulties that I encountered when attempting to redesign the fabrication process. I hope that these serve as examples and help future researchers avoid some of these problems before encountering them.

1. Depositing AlN on HR silicon using a Titanium adhesion layer

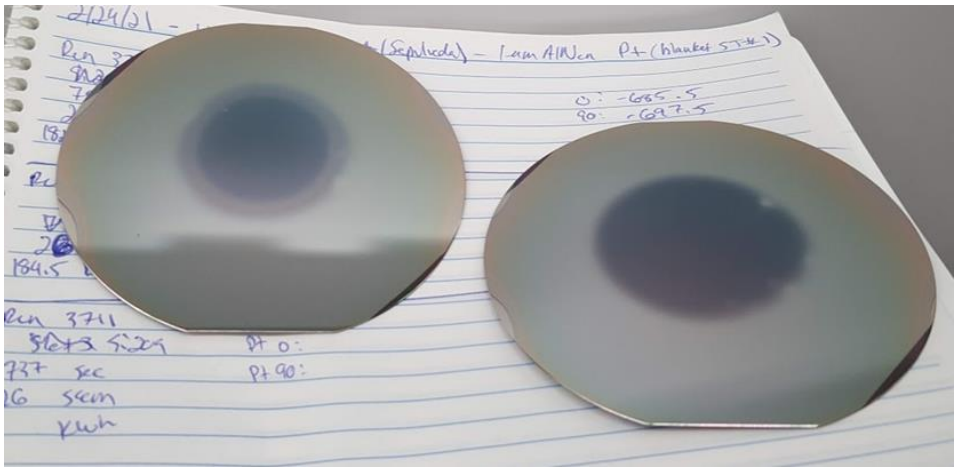

Figure 3-15 Issue with AlN deposition caused by poor heat conduction by high resistivity silicon wafers. The increased heat during deposition caused the platinum to chemically react with the silicon.

As described in the microfabrication section above, the piezoelectric AlN layer was deposited by a group at Carnegie Mellon University. They had done this deposition many times for our group, so when I requested that they deposit a new batch of silicon wafers, I did not expect any issues. With this new batch, I requested there mainly two modifications made compared to previous AlN depositions. I requested that the AlN residual stress be tensile as opposed to the normal compressive stress, and I requested that the depositions be done on high-resistivity silicon wafers. When the staff attempted the deposition, they immediately ran into some issues were the AlN that was being deposited had some very drastic discolorations. After much experimentation, the staff discovered that the cause for these issues was our use of very high-resistivity silicon substrates. These wafers would not conduct heat very well, so they would heat up a lot during the deposition, and thus this heat caused the platinum electrode to react with the silicon forming an unwanted compound that affected the growth of the AlN. This issue could not be resolved, so we had to switch to normal n-type silicon wafers. In addition to the HR silicon heating problem, the group

ran into an issue with the AlN that was caused by the titanium adhesion layer used below the platinum. It appeared that using Titanium would cause the AlN film to look a lot darker than usual. This was surprising to the group as they had been using titanium as an adhesion layer for many years. However, for the sake of time, we had to make a quick modification that would allow us to get the wafers as soon as possible. We decided to change the adhesion layer from titanium to tantalum, seeing as they had also used this in the past. This worked well, and the AlN films obtained were of very high quality.

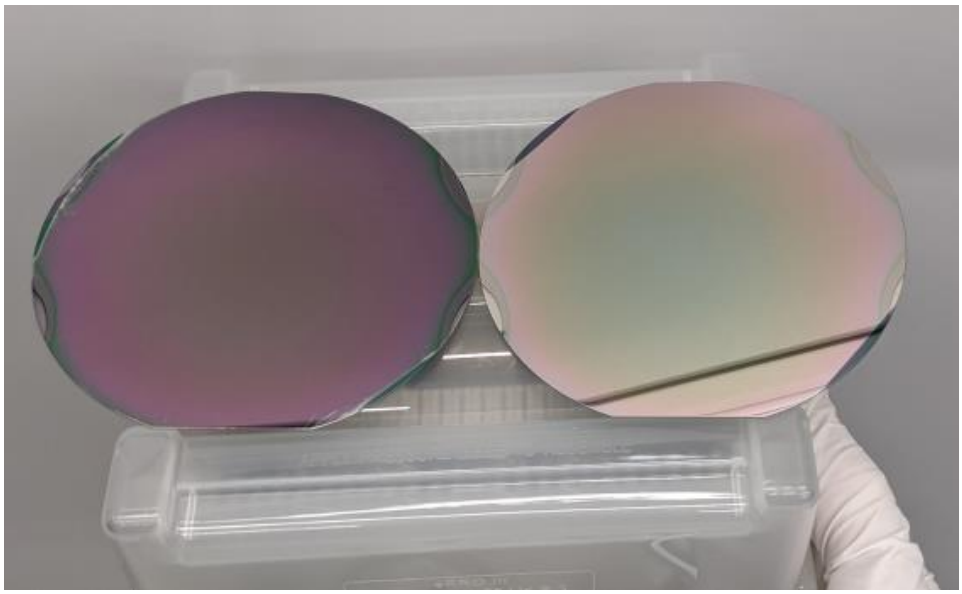

Figure 3-16 Darkened AlN when using titanium as an adhesion layer. The wafer on the right was deposited using a tantalum adhesion layer instead. The quality of the AlN on the right was much better than the one on the left.

2. Dicing AlN wafers

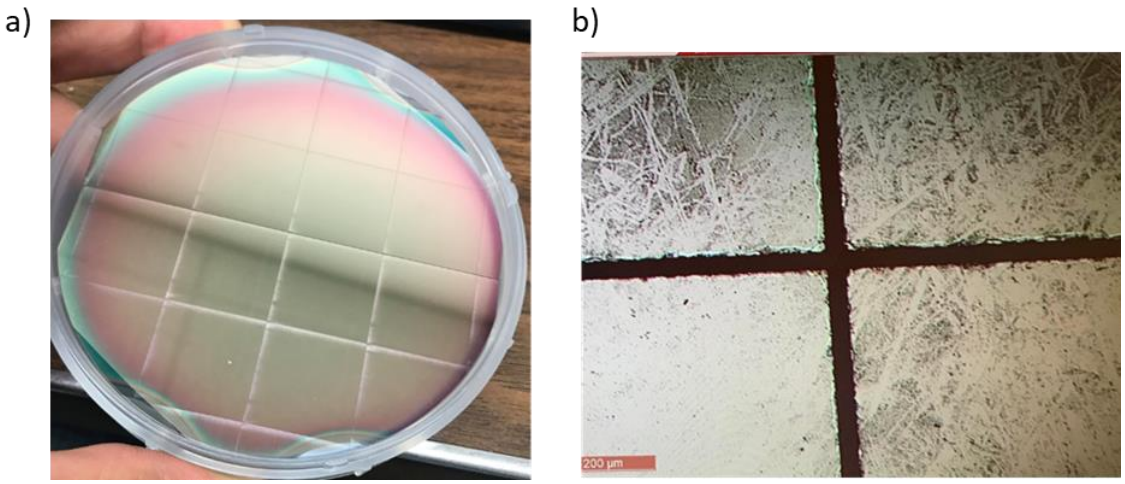

Figure 3-17 (a) AlN wafer diced without photoresist layer to protect the surface. (b) Microscope image showing the debris and dust on the surface of the AlN along the dicing lines produced by the sawing procedure.

One of the first issues encountered when attempting to fabricate these antennas occurred during the wafer dicing process. I sent the 4-inch wafers to be diced into 22mm x 22mm square pieces at the High-Frequency Electronics Laboratory. When I received them, I noticed that there seemed to be some dust along the dicing lines. Upon further microscopic inspection, I noticed that the AlN surface had gotten dirty with debris from the sawed silicon. I noticed that this dust was not easy to remove with acetone, methanol, isopropanol, and water. It required the use of DI Water in the ultrasonic bath for about 1 minute to remove most of the dust. However, even with this procedure, the pieces were never again perfectly clean, and this affected the quality of the subsequent metal layers deposited on the AlN.

To prevent this from happening, the 4 in wafer must be coated in a protective layer of photoresist prior to the dicing procedure. I chose to use soft-baked AZ5214 photoresist because of

how easy it was to remove using acetone. After implementing this protocol, I never again encountered this issue.

3. KMPR1005 photoresist

Figure 3-18 Bottle of KMPR 1005 photoresist originally used in June 2021, which had expired for a year. It can be seen that the expiration date is also only valid if the bottle is stored at -10C, which was not the case with this bottle. This caused many issues with the photolithography development process.

As described previously, KMPR 1005 photoresist was chosen due to its thickness and etching resistance. However, one of the main reasons we used it was because its developer (SU-8 Developer) did not attack AlN, which cannot be said for other commonly used developers like AZ300MIF or AZ400K. When I began the microfabrication process development, I ran into a lot of issues trying to figure out the exact photolithography processing steps using this photoresist. I would follow the exact steps outlined in the data sheet provided by the manufacturer, but this would never work. After much trial and error and modifying everything from the prebake

temperature to the exposure dose to the development time, I ultimately got the photolithography to work. However, even in the best-case scenario, the smallest features I could repeatedly pattern were on the order of 5 um. This was an issue because the linewidth of the features on the antenna mask was 3.5 um. According to the manufacturer, this photoresist should be able to pattern features down to 1 um, so I had to find the reason why it was not working. After much research, I discovered that the KMPR resists have to be stored frozen to prevent deterioration. The resist I was using was provided by the cleanroom facilities at UCLA, and they were storing it in a normal refrigerator. In addition, the photoresist bottle had expired by a year, and according to the manufacturer, if the photoresist is not frozen, the photoresist will deteriorate within months. I presented this information to the cleanroom facilities and requested that they buy a new bottle of KMPR and that they store it in a freezer. Once the new bottle arrived, I followed the photolithography process outlined in the photoresist datasheet and successfully patterned even the smallest features on our mask.

It is important to note that we would store small bottles poured from the main bottle of KMPR at room temperature to be used in the span of a week in order to avoid having to continuously freeze and thaw the main bottle. Over the course of the last two years, I noticed that these bottles stored at room temperature would quickly change their properties. As they aged, they became much more sensitive to the exposure dose of UV light. Where the photoresist from the original bottle needed a 10-second exposure, a bottle that had been sitting at room temperature for about three months only needed 6 seconds. This issue was not seen with other photoresists.

4. Etching ground vias

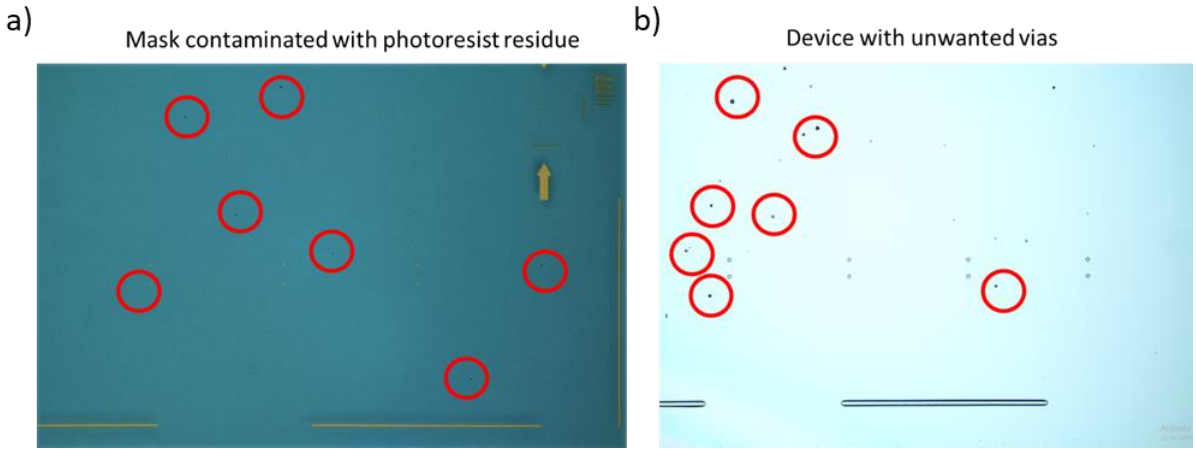

Figure 3-19 (a) Microscope image of a photomask used during photolithography. The red circles show specks of dust and photoresist that were hard to remove with a normal AMI solvent wash. (b) Resulting pattern after ground via etching. The red circles show that these specks of dust caused the creation of unwanted vias. These vias were problematic because they shorted out the piezoelectric electrode sandwich structure at unwanted locations.

As one uses a photomask repeatedly for various processes, it becomes dirty with photoresist residue and specks of dust. For this reason, it is very important to clean the mask after every photolithography session. Typically this mask is cleaned with acetone, methanol, IPA, and water; however, there are times when this solvent wash is insufficient to remove all the photoresist residue. One of the big issues this caused was that during the photolithography step used to make the ground vias, these specks of dust and photoresist would also result in small patterns transferred onto the photoresist since they also blocked UV light. During the AlN etching step, these small dots would also allow AZ300MIF to get through and etch the AlN at unwanted locations. These unwanted vias would then subsequently cause the top metal layers to short through the AlN and connect with the bottom ground plane. This issue was hard to find since these specks of photoresist and dust were too small to be seen with the human eye. It wasn't until I examined the photomask

under the microscope that I realized that the unwanted vias or pinholes on our devices matched up perfectly with the location of small specks of dust and photoresist that were stuck onto the mask. Since the normal solvent washes were not enough to get rid of all these specks, I had to use more drastic measures. I attempted to use a heated NMP bath, but this did not seem to work either. Ultimately, what worked the best seemed to be submerging the mask in a bath of AZ300T photoresist stripper heated to 80 C for 30 minutes, then cleaning it with DI water and drying it thoroughly with Nitrogen.

5. Metal liftoff failure

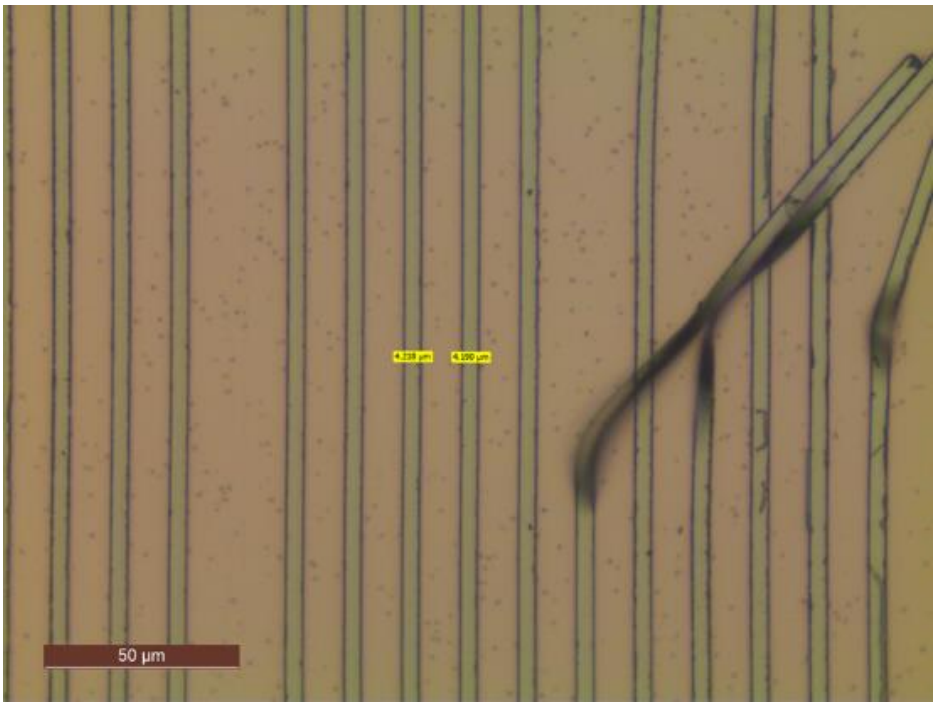

Figure 3-20 Microscope image of metal bars peeling off. This failed liftoff procedure was caused by the poor photolithographic development of the photoresist.

Another common source of failure in our early devices was the fact that deposited metal bars would not adhere to the AlN surface. After placing the devices in the photoresist stripper to remove the photoresist and achieve the metal liftoff, I would come back to more than 50 percent of the

deposited pattern peeled off. After a thorough investigation, I found that this issue stemmed from 2 distinct causes: The photoresist was not fully developed, and we needed an adhesion layer between the metal and the AlN surface. The issue with the photoresist not being fully developed was caused by our use of the expired photoresist bottle, as outlined above. This old photoresist became hard to develop, and given its large thickness, it would appear fully developed under the microscope, but there was often still photoresist in the developed trenches. This issue was resolved when we began using the new bottle of KMPR 1005 photoresist. In addition, we began to put the piece in the Matrix Asher for a 1-minute oxygen plasma descum procedure. This ensured that we were removing all of the unwanted photoresists from the trench. As for the second source of the issue, we discovered that the adhesion of the metal films was significantly improved with the use of a thin adhesion layer. We tried chromium and titanium since these are the two most commonly used adhesion layers and determined that titanium gave us the best results. The use of a thin titanium layer between the metal and the AlN, as well as using the new photoresist, resulted in great adhesion between the deposited metal and the AlN surface. Furthermore, I found that if you prebake the device on a hotplate at 100C for a couple of minutes prior to the metal deposition, this also increases the adhesion of the film. I am unsure as to why this is, but I assume it has something to do with removing the moisture on the surface of the AlN.

6. Chlorine RIE Etching failure

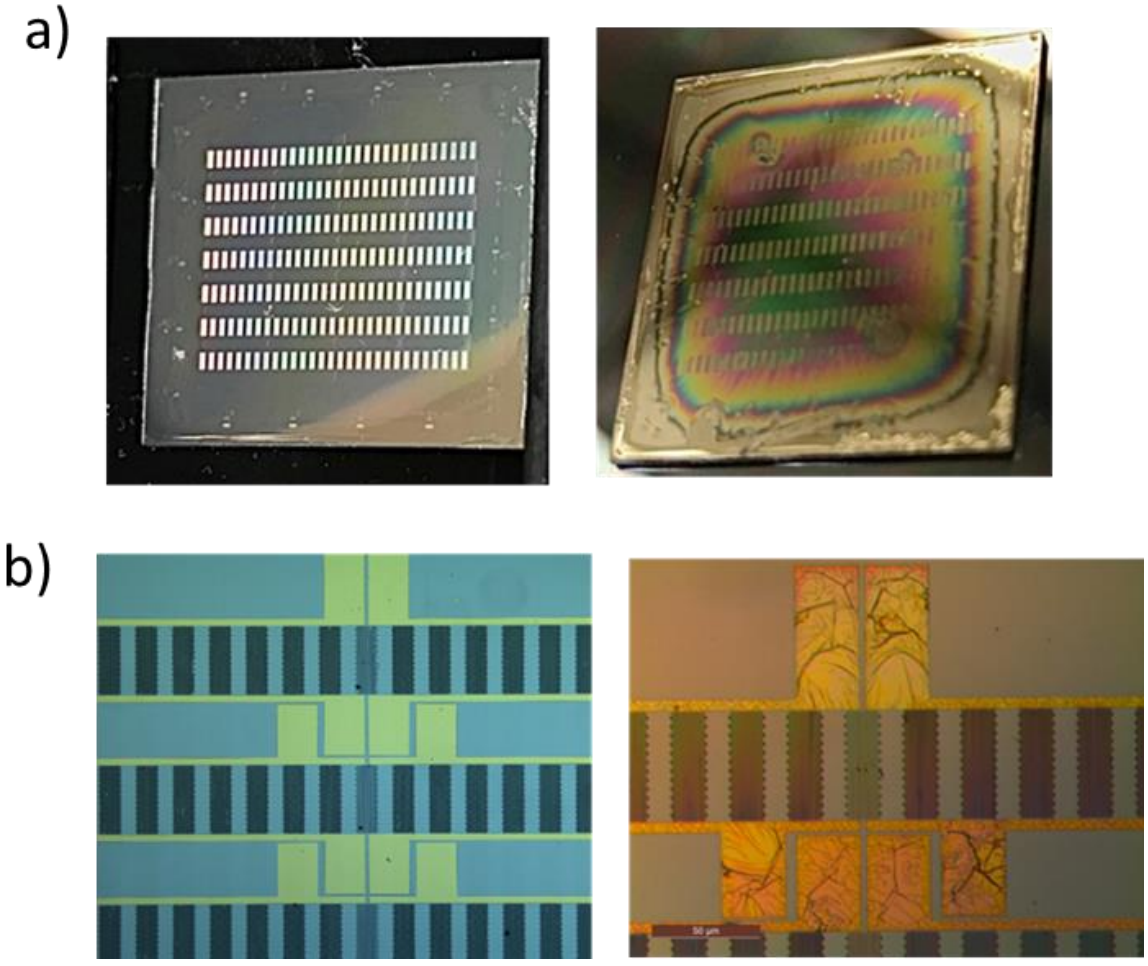

Figure 3-21 (a) Image showing the antenna chip before and after the Cl2 RIE etch aimed at etching the vias through the AlN and Pt down to the silicon. The image on the right shows the results of an etch that was too long. In this image, the photoresist has been mostly removed, and even unwanted regions of the AlN have been etched. (b) Microscope images showing the results after a successful etch that unfortunately resulted in a thin layer of photoresist above the electrodes being hardened and becoming nearly impossible to remove without the aid of oxygen plasma stripping. This issue occurred because the photoresist became too hot during the etching process.

As described previously, in order for the device to work, we had to etch the silicon beneath the AlN. In order to do so, we had to first etch vias through the AlN and the Pt so we could have access to the supporting silicon below. This etch was conducted using chlorine plasma RIE etching. In this procedure, we ran into two main issues. I will describe these challenges in detail below:

- Etch time

When we began this project, we were given instructions that this etching was to be split up into three separate 3-minute etches for a total of a 9-minute etch. This process had supposedly worked for a previous student. However, I immediately found that this would not be possible because when the pieces came out of the system after the third etch, the photoresist that was used as an etching mask was almost completely removed. In fact, the resist around the perimeter of the square piece was completely removed, and the chlorine etching removed most of the AlN below it. This caused the rainbow coloring that can be observed in the images above. Due to this, we had to find a new etching process, and through some experimentation, I found that a two-part etch comprised of a 3-minute etch, and a 3-minute and 10-second etch was exactly enough to etch through the AlN and the Pt at the via locations and not risk completely removing the photoresist used as an etching mask.

- Hard-baked resist on top of metal structures

The second challenge related to the chlorine RIE etch was that after doing the etch and attempting to strip off the photoresist mask, most of the photoresist from the AlN surface came off, but the photoresist that happened to be above the metal patterns would not. The photoresist above the metal patterns seemed to form a thin hardened layer that was almost impossible to remove using the heated NMP bath. It did not matter how long I left the pieces in the NMP or how vigorous the

agitation was. Only a very small amount of this hardened photoresist would come off. I even tried to remove it using the ultrasonic bath, but this only minimally worked. The one thing that I found was capable of removing this thin layer of photoresist was using the Matrix oxygen plasma cleaner at 250 C and 500W for a short 10-second photoresist stripping. This instantly removed all of this hardened resist. However, the heated oxygen environment inside the chamber also oxidized the metal surfaces. By keeping this procedure as short as possible, one can minimize the amount of oxidation that occurs. Alternatively, the metal surfaces can be coated with some protective material like titanium or tungsten to reduce the amount of oxidation. This issue with the hardened resist was not predictable, some pieces would have it, and others would not. The only factor that I could deduce would reduce the likelihood of it occurring was making sure that when the piece was put into the chlorine RIE etcher, it had to be mounted onto the carrier wafer with enough thermal paste. If there was too little thermal paste, this photoresist's hardening would be more evident.

7. XeF2 etch

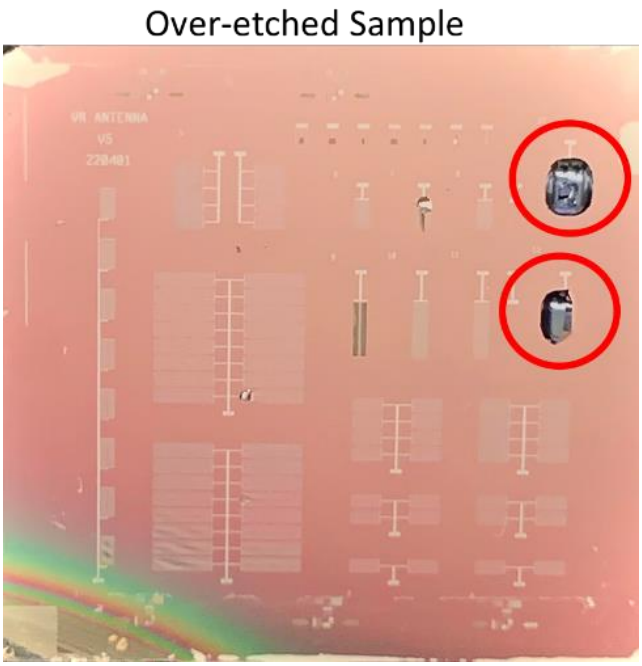

Figure 3-22 Image showing the results from a XeF2 silicon etch that was too long. The amount of silicon removed beneath the antennas was too much, and the fragile film eventually broke and exposed the etched silicon beneath the AlN.

The silicon release step using the XeF2 vapor had its own set of challenges. The two biggest challenges were that XeF2 vapor seemed to etch some of the metals we had originally planned on using for the top electrodes in this device and that since the AlN and Pt film are opaque, we could not tell how much silicon was being etched underneath. I'll go into more detail about these two challenges below:

1. XeF2 attacking gold electrodes

We had originally planned to use gold top electrodes on our antenna. The reason for this was that gold does not oxidize and has a very high conductivity. I fabricated multiple devices up until this last step, and once I took them out of the XeF2 etching chamber, I noticed that the gold films were darkened. I noticed that the longer I performed the silicon etch, the more the gold electrodes would turn black. After some research, I ended up discovering that gold would react with XeF2 in the

presence of any moisture. So in order to reduce this effect, I would have to bake my samples until they were completely dehydrated. This procedure seemed to work only minimally, as the gold electrodes would still show signs of deterioration, albeit less than before. After much trial and error, I finally decided to change materials and found that the only other material that had high conductivity, was cheap to deposit, and would not react with XeF2 was aluminum. From that point on, all of the electrodes on my devices were fabricated using aluminum instead of gold.

2. Measuring etch distance

Each antenna on the chip had to have the silicon supporting it complete removed from underneath it. To achieve this, we put the chip in the XeF2 etching chamber, but after etching the first batch, we realized that we had no way of knowing if we had completely removed the silicon support underneath unless we destroyed the film. To avoid having to destroy the film, I came up with the idea of figuring out what areas beneath the film were etched by scanning the surface with a Dektak profilometer. By using a very small tip force, we could prevent the tip from puncturing the surface. As the tip scanned the surface, it would eventually reach a point where the supporting silicon substrate had been removed, and it would push the AlN film down. This allowed us to see what areas still had silicon underneath and which did not. By using this process, we could progressively perform the XeF2 etch while measuring the amount etched so as to not under or over-etch.

8. AlN Film Buckling

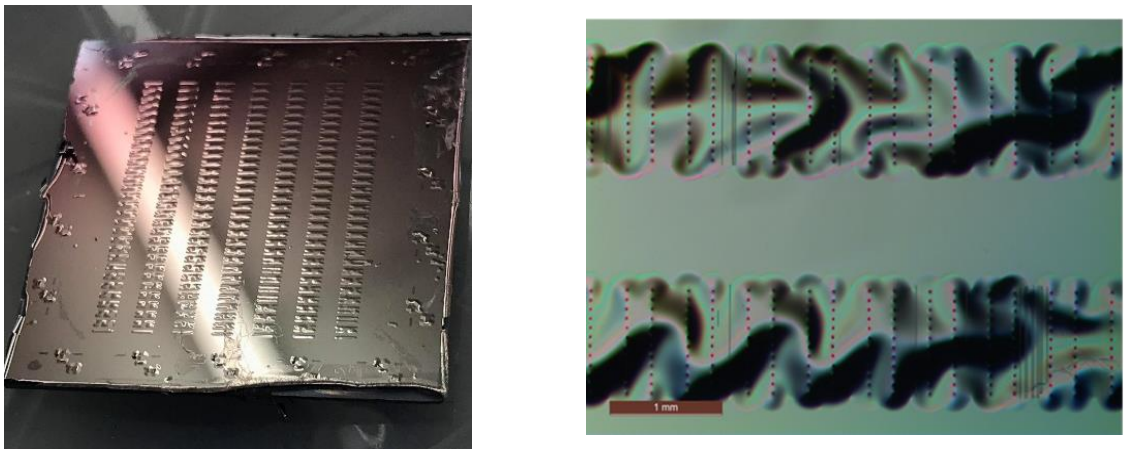

Figure 3-23 Images showing the results of a bad XeF2 etch where the film above the etched areas appears to have buckled. This occurred due to the AlN film having been deposited with high compressive stress so that when the silicon beneath it was removed, the thin film could no longer keep its shape.

Another challenge we experienced while performing the silicon substrate etch was that the AlN film above the areas that were etched was deforming out-of-plane. These out-of-plane deformations were evident even to the naked eye. The cause for these deformations ended up being residual stresses in the AlN film. We found that these films were fabricated with compressive stress, and when the silicon support was removed, these films acted as thin plates subjected to compressive loads. Once the etched area became large enough, the film was not able to withstand the compressive force, and the film buckled, leading to large out-of-plane deformations. Once this issue was discovered, we decided to order new AlN wafers but clearly specified that we wanted to tune the residual stresses to be as small as possible and, if there were to be some stresses present, for them to be tensile instead of compressive. Tensile residual stress would not result in the film buckling regardless of the size of the etched area underneath each antenna. In order to tune these stresses, the researchers at Carnegie Mellon University tuned the argon pressure and sputtering power to get a slight tensile film stress.

3.5 Material Characterization

In this section, I will give some information about the material characterization experiments conducted in order to verify the quality of the materials used.

3.5.1 Magnetic

One of the most commonly used methods of characterizing magnetic materials is through the use of super conducting quantum interference device (SQUID) magnetometry. This allows you to measure the magnetization of a very small amount of magnetic material given an applied magnetic field. By sweeping the applied magnetic field, one can obtain the magnetic hysteresis for a specific material or structure. This magnetic hysteresis loop can provide information such as the saturation magnetization of the material, the coercivity H_c, and the field required to saturate it H_{sat}, amongst other things. In our case, we wanted to primarily figure out what the coercivity of the magnetic material we were depositing was. The reason for this was that this coercivity would tell us if the magnetization of the material was too hard to be switched using the applied strain from the AlN. The results from the SQUID measurement of the deposited FeGaB film are shown below:

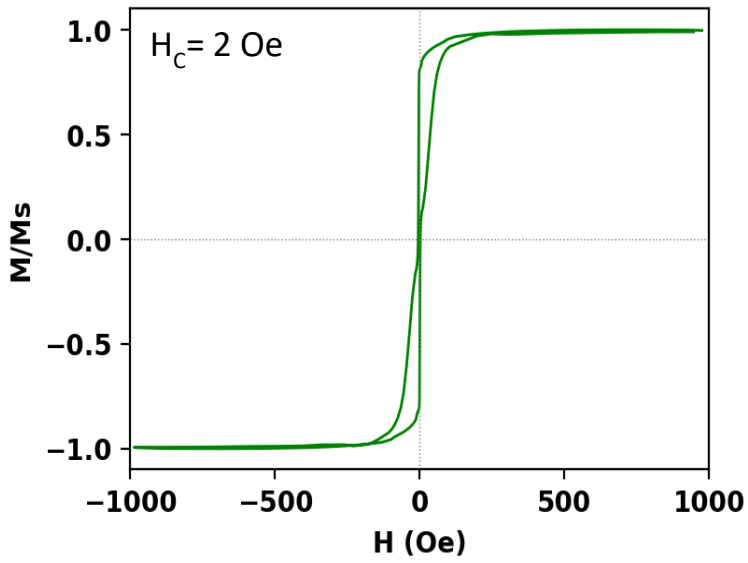

Figure 3-24 Magnetic hysteresis for our Ti (8nm) / [FeGaB (45nm) / SiO2 (5nm)]x9 / FeGaB (45nm) / Ti (8nm) magnetic stack. Magnetization is normalized. Coercivity is approximately 2 Oe. The pinching seen close to the origin of the plot can be attributed to inconsistent SiO2 interlayer thicknesses.

In this plot, we see that the coercivity is on the order of 2Oe, which is extremely low. This is beneficial for our device since it lowers the magnetic losses during magnetization switching. The easier it is for the magnetization to change given an applied strain. It is important to note that the shape of the hysteresis loop is a bit anomalous since it should not pinch at the center as it does. According to our collaborators at Northeastern University, this could be caused by the inconsistent SiO_2 thicknesses deposited by the system. This was an issue that was observed after the deposition had been completed.

Another characteristic of the magnetic material that was important to know was that of the gilbert damping factor α. This parameter is a unitless number that describes the resistance or lack thereof of a magnetic moment to change directions. A lower damping factor means that the magnetic material is less resistant to direction change. As you can imagine, this means that, in our case, we would prefer to have a low damping factor. For comparison, a similar material

FeGa/Cu, has been shown to have a damping factor of around .05. The results of the measurement of this damping factor are shown below:

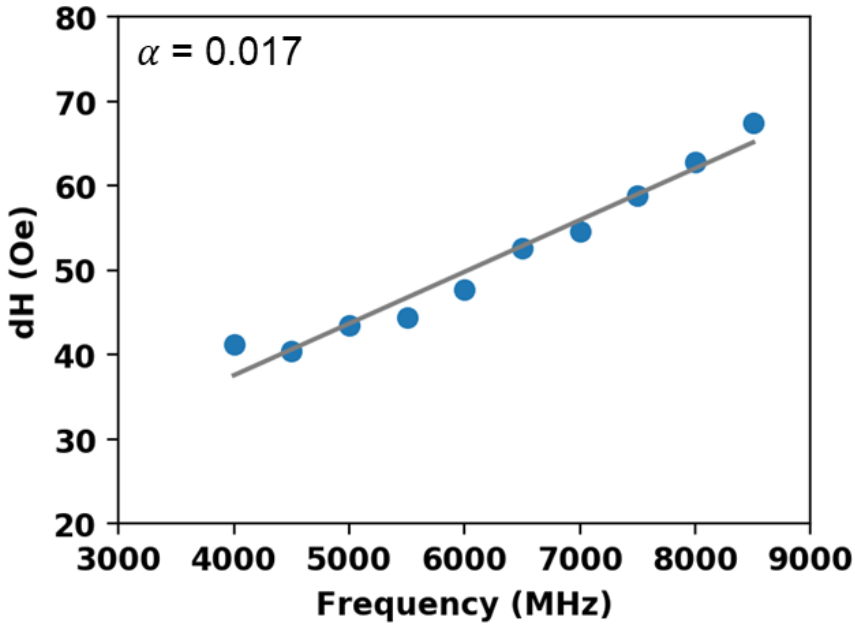

Figure 3-25 Measurement of Gilbert's damping coefficient in FeGaB film. The slope of the line indicates a damping coefficient of .017 which is very low compared to similar magnetostrictive materials.

The slope of the plot above gives us the damping factor of the Ti (8nm) / [FeGaB (45nnm) / SiO2 (5nm)]x9 / FeGaB (45nm) / Ti (8nm)stack we deposited. We can see that it is very low (.017) even compared to similar magnetostrictive materials like FeGa (.05). This is good for the device since we want to minimize the material's resistance to magnetization change.

Finally, we wanted to also measure the magnetostrictive performance of the Ti (8nm) / [FeGaB (45nnm) / SiO2 (5nm)]x9 / FeGaB (45nm) / Ti (8nm) film deposited. To do so, our colleagues at NEU measure the magnetostriction of the material as a function of the applied field. The results are shown below compared to their typical FeGaB deposited stack:

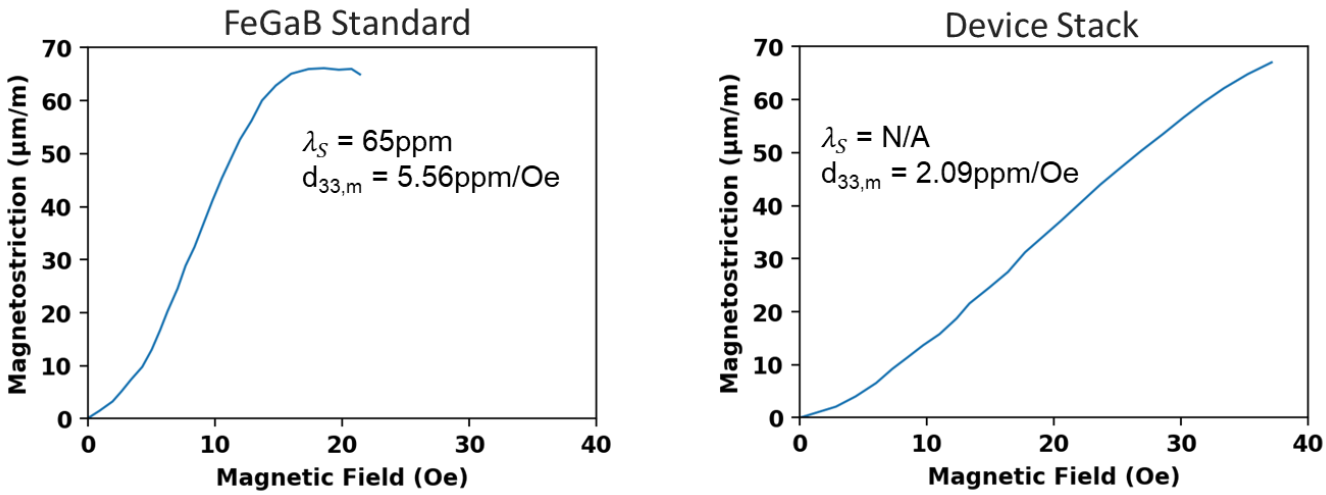

Figure 3-26 Magnetostriction measurements for FeGaB and our Ti (8nm) / [FeGaB (45nnm) / SiO2 (5nm)]x9 / FeGaB (45nm) / Ti (8nm) magnetic stack. Comparison of piezomagnetic coefficient and saturation magnetostriction. Saturation magnetostriction is not available for our film due to the field required for saturation was higher than what our system could provide.

We can see above that the piezomagnetic coefficient d_{33} for our material is about 2.09 ppm/Oe, which is good but much lower than the FeGaB standard of 5.56 ppm/Oe. According to our colleagues, this could be caused by our use of a titanium seed layer rather than their typical Cr or Cu seed layer. This difference may also account for the change in saturation magnetization, which, as can be observed, is not reached on our film. Regardless of these differences, the magnetic characterization of this material shows favorable results.

3.5.2 Piezoelectric

Prior to the full fabrication of our device, we first wanted to characterize the properties of the AlN material deposited by the group at Carnegie Mellon University. After the deposition, their group performed a measurement of the residual film stress. The results are shown in the table below:

Wafer Number	AlN Stress (MPa)		
	0°	90°	Average
1	66.5	60.3	63.4
2	120	112	116.0
3	45.5	39.1	42.3
4	123.4	118.4	120.9

Table 3-1. Table of fabrication stresses on the four new AlN wafers ordered from Carnegie Mellon University. As can be seen, these new wafers all had positive tensile stresses in order to prevent the film from buckling after the removal of the silicon beneath it.

As can be seen in the table above, all of the four wafers deposited have positive stresses ranging from 42.3 MPa to 120 MPa. It is important to note that for this batch, it was explicitly requested that all films have positive tensile stress. The reason for this was to reduce the likelihood of the films buckling after the silicon release step.

In addition to this measurement, the CMU team also measured the rocking curve full width at mid-height FWMH. This was done to quantify the quality of the deposited AlN crystal. The results are shown below:

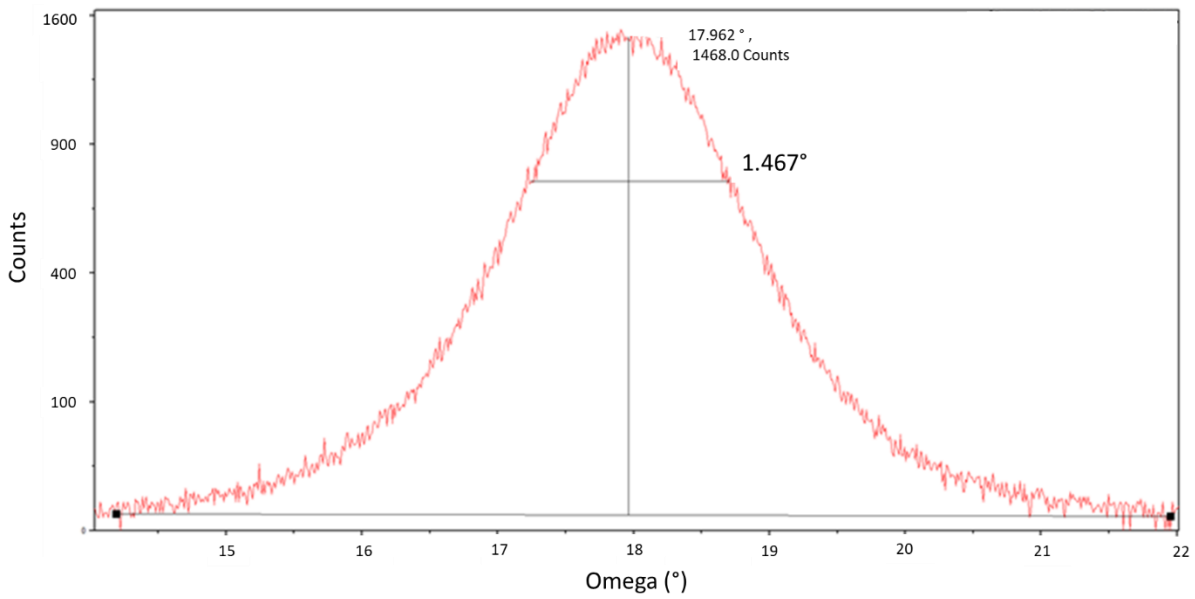

Figure 3-27 Rocking curve of AlN deposited. FWMH is 1.467 degrees which correspond to a highly c-axis AlN film.

As can be seen in the plot above, the FWMH is 1.467, which corresponds to a highly c-axis AlN film. This is an excellent value for AlN films of this thickness grown on metal electrodes [88]

Finally, we measured the electric permittivity of the AlN film and compared it to that which was reported in the literature. In the plot shown below, we can see that the permittivity is approximately 11. The permittivity reported in the literature is around 9, which is relatively close to our measured value. In addition, we also measured the current through the bottom and top electrodes as we varied the applied voltage. This was done to ensure that there were no pinholes in the AlN film. The fact that we saw no current, regardless of the applied voltage, meant that the film quality was good, and there were no pinholes present.

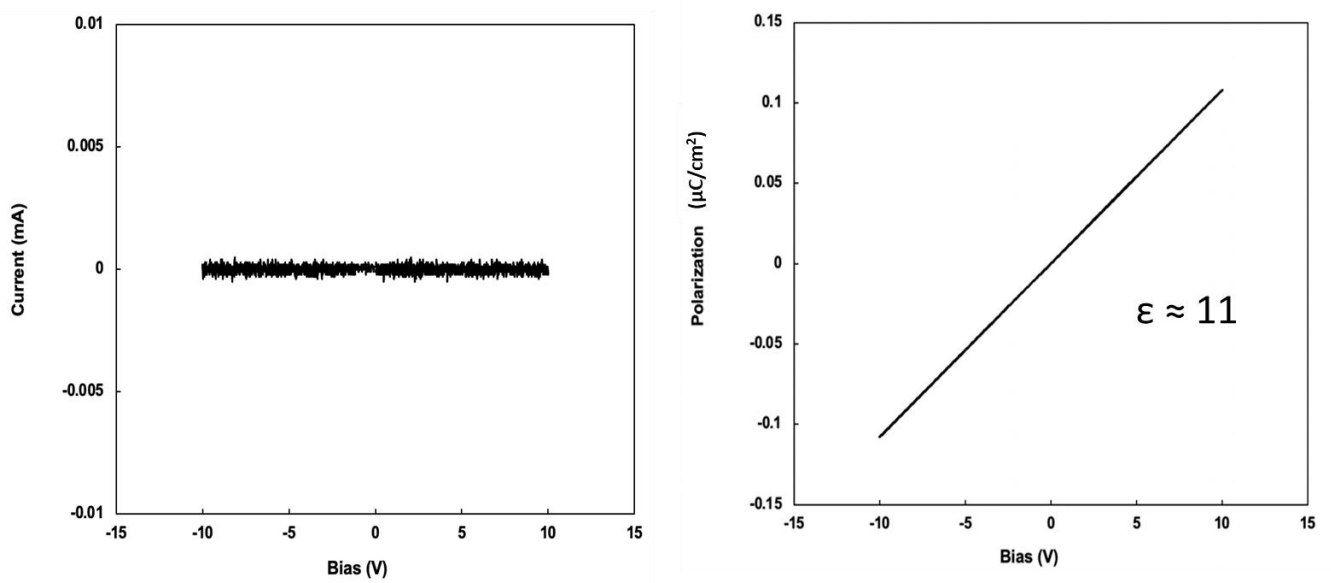

Figure 3-28 Characterization of AlN electric properties. (a) flat voltage vs. current plot, meaning that the film was continuous and did not have any pinholes. (b) Voltage vs. Polarization plot with which we can calculate the electric permittivity of AlN to be 11.

3.5.3 Air cavity width

As described in the sections above, the last step in the fabrication process for the antenna is the silicon release step. In this step, the silicon beneath the antenna is removed using a XeF2 vapor etch. It is very difficult to know exactly how much silicon has been removed after a certain etch time. Also, the etch rate varies with the amount of silicon sidewall exposed and the pressures measured by the system. These uncertainties make it extremely difficult to determine if the etch has been completed or not. One way of determining the etched amount is by adding test structures that can be destroyed in order to measure the amount of Silicon removed beneath the AlN. This method is not sustainable since you have to repeatedly destroy portions of the chip. So in order to address this problem, we came up with a method for determining the etched distance without the need to destroy the AlN. To do so, we used a Dektak surface profilometer to measure the

topography of the chip. If we measured a device with the silicon beneath it removed, the tip would push down the AlN film, and the deformation would be evident in the outputted plot. This added deformation would tell us exactly how much silicon had been removed beneath the device without destroying it. The results of one such measurement are shown below:

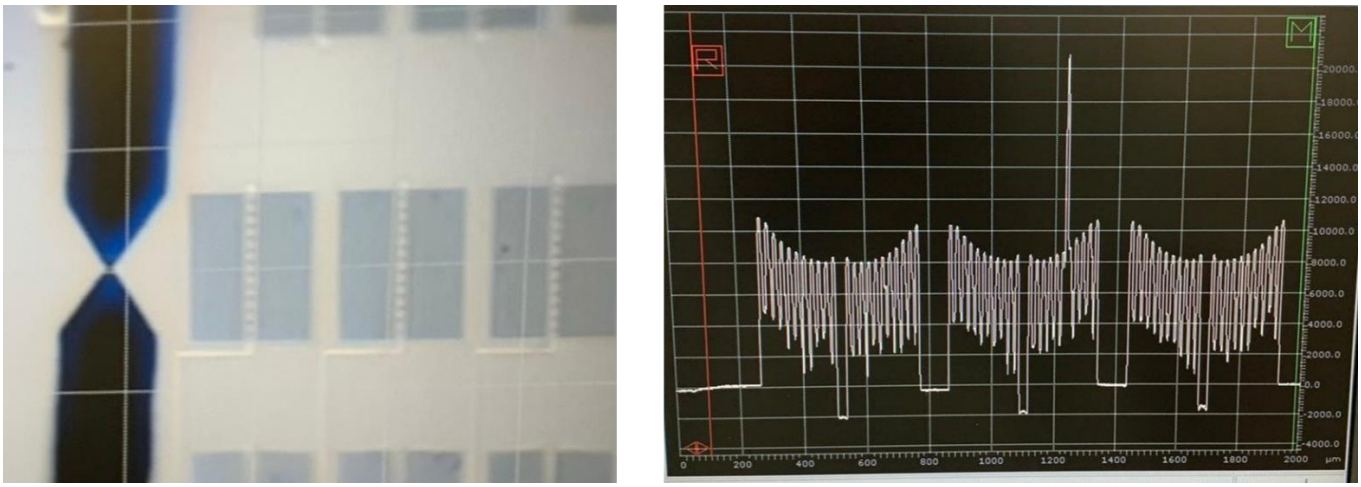

Figure 3-29 Silicon removal measurement using Dektak profilometer. (a) microscope image of tip scanning above the antenna structures. (b) Dektak scan results after scanning the above three antennas side by side. As can be observed, the film is pushed down when scanning above the antenna structures.

In the image shown above, we can see both the microscope image of the tip scanning along the surface of the chip and the resulting surface topography. As can be seen in the image on the right, each of the three scanned antennas has a concave surface which allows us to know the amount of silicon that has been etched beneath each antenna. At locations away from the antenna, the surface is flat, which means there is still silicon beneath those areas. This technique allowed us to perform an etch and visualize the amount of silicon removed and allowed us to continue etching if necessary.

3.6 Experimental Results

Once the fabrication process of the antenna was established, we went ahead and began testing the performance of the antenna. All of these tests were conducted at the University of Texas at Dallas with our colleague Nishanth Virushabadoss from Rashaunda Henderson's group. As described previously, most of my focus was on developing the microfabrication process. For this reason, I will not be delving into detail about the specifics of the different testing procedures. I will only discuss the main results relating to the S11 reflection coefficient and the S21 transmission coefficient testing.

3.6.1 S11 Reflection Coefficient

As described previously, we designed this antenna to mechanically resonate at 400 MHz in order for it to radiate within the Medical Implant Communication System (MICS) frequency band. In order to achieve this, we used FEM to design the dimensions and geometry of the electrodes, magnetic bars, and piezoelectric material. From the model, we concluded that our antenna design should mechanically resonate close to 400 MHz. In order to test whether this would happen experimentally, we subjected our fabricated antenna to an S11 reflection coefficient test. This test measured the amount of energy reflected back as you varied the frequency of the input signal into the antenna. The signal was fed onto the top electrodes of the antenna using a GSG probe connected to a vector network analyzer (VNA). The results of this measurement are shown in **Figure 3-30** below. In this plot, we see that the reflection coefficient S11 is minimized at around 420.5 MHz, which means that the antenna is resonating at this frequency and successfully converting the electrical energy into piezoelectric mechanical vibrations. This measurement successfully validated our design and confirmed that our antenna was mechanically resonating at the desired frequency. The shift from the expected 400 MHz to the measured 420 MHz could be attributed to

inconsistencies in fabrication processes. These inconsistencies could result in the dimensions of the components of the antenna being slightly larger or smaller than designed, which would, in turn, cause a slight shift in frequency. Additionally, the FEM models used to design this antenna did not consider the film stresses present in the AlN. Even though we fabricated these devices with as neutral film stress as possible, any residual stress would cause a shift in the resonant frequency. In addition to measuring the S11 response, we also measured how this S11 curve would shift as the strength of the applied bias field increased. We observed that as the applied magnetics bias field increased from 0 Oe to 200 Oe, the resonant frequency shifted monotonically from 420.6 to 420.7 MHz. Even though this change is extremely small, it suggests that there is magneto-mechanical coupling. The change in frequency can be explained by an effect known as the delta-E effect, where the stiffness of a magnetic material increases with an applied field. This change in the stiffness of the magnetic bars in our device would increase the overall resonant frequency.

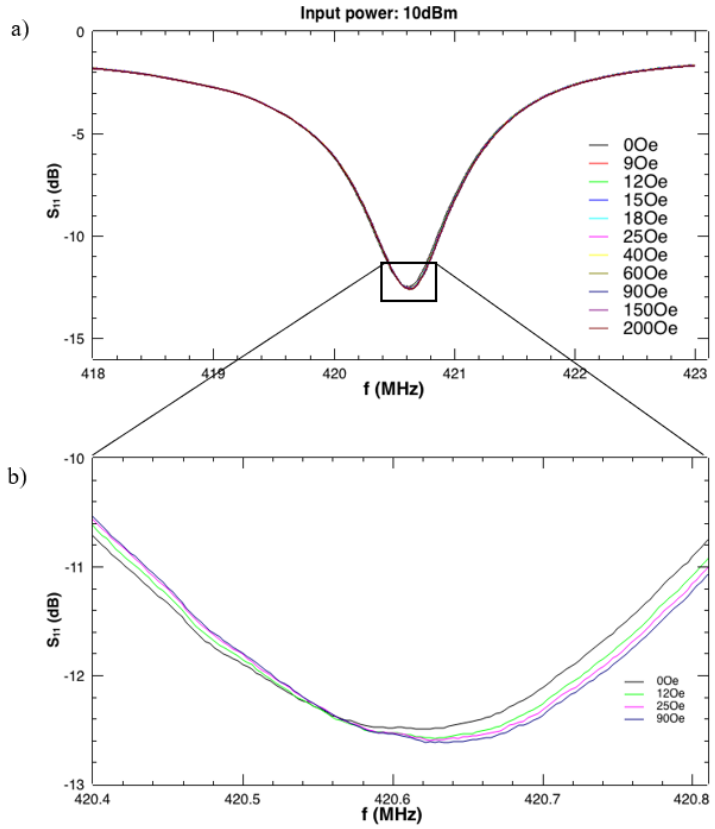

Figure 3-30 Reflection Coefficient S11 measurement. (a) Full S11 peak showing the resonant behavior of our structure at around 420 MHz. (b) A zoomed-in image of different S11 measurements done by applying different magnetic fields. It can be observed that the resonant frequency shifts slowly to higher values. This shift could be attributed to the delta-E effect in magnetic materials.

3.6.2 S21 Transmission Coefficient

Once the mechanical resonance of the antenna was experimentally verified using the S11 test described above, we proceeded to measure the radiation performance of our antenna. To do so, we measured the S21 transmission coefficient as a function of applied signal frequency. In this test, Port 1 was a GSG probe connected to our antenna, and Port 2 was a magnetic field probe that would sense small AC magnetic fields. This S21 parameter measures how power is transferred to the magnetic field probe from our antenna relative to the input power as a function of frequency. In this test, the magnetic probe was placed in close proximity (around 3cm) to our antenna (**Figure**

3-31). This was done in order to ensure that any radiated magnetic fields from our antenna would be captured by the magnetic field probe.

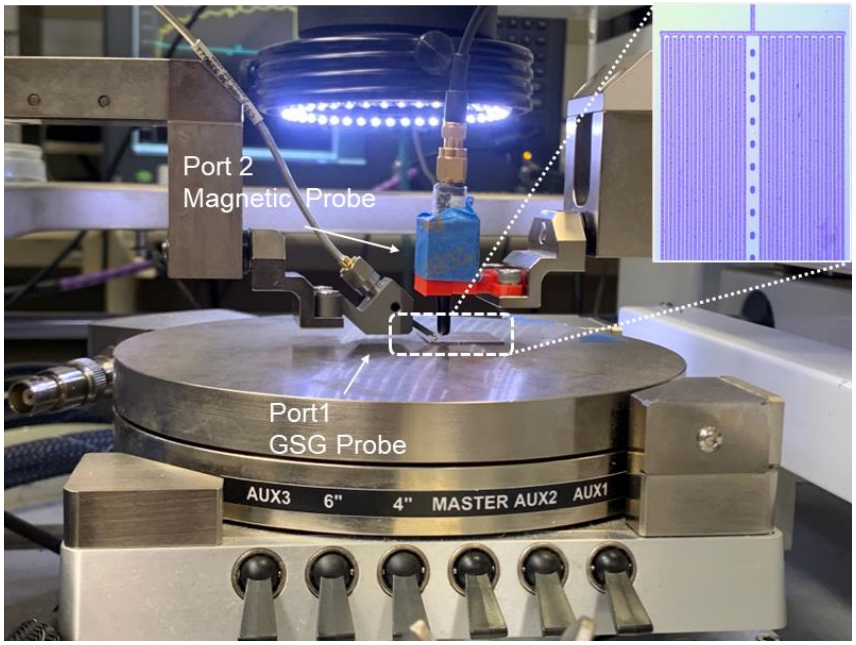

Figure 3-31 Experimental Setup for S21 transmission coefficient test.

The results of the test conducted are shown in **Figure 3-32**. Here we see that the transmission peaks at the resonant frequency of around 417 MHz, which is close to the 420 MHz resonant frequency obtained in the S11 test. Additionally, we tested how this S21 peak would change as we varied the bias field from 0 to 90 Oe. We observed that, again, the S21 peak would shift to higher frequencies as the bias field strength increased. This shift in resonant frequencies can be explained by the increase in magnetic material stiffness that occurs with stronger bias fields (delta-E effect).

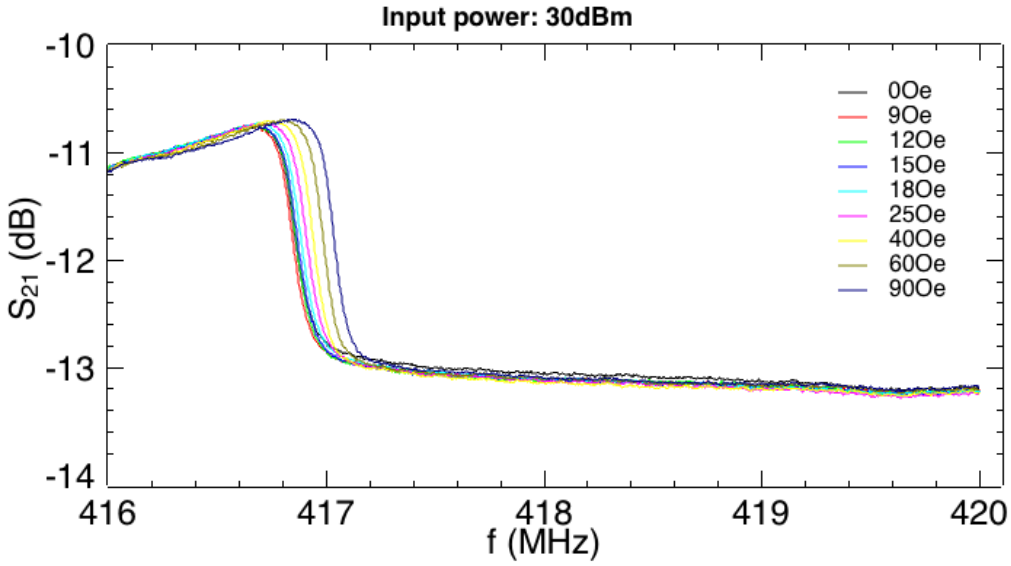

Figure 3-32 Measurement of S21 transmission coefficient with different applied bias magnetic fields. As the applied bias field increases, the increase in resonant frequency suggests that this behavior could stem from the delta-E effect experienced by the magnetostrictive bars.

3.7 Conclusions

In this chapter, I discussed our development of a 400 MHz multiferroic antenna. I first discussed the reasons why there is a need for miniaturized implantable antennas today and how current electrically small antennas are not well suited to address these challenges. Next, I discussed the benefits of using multiferroic technology to address the limitations of electrically small antennas. I then introduced the design of our antenna and described its operation mechanism in detail. Given that my role in the project primarily consisted in developing the microfabrication process for this antenna, my focus in this chapter was outlining the fabrication process in detail and including information about the challenges experienced during the design of this fabrication process and how we overcame them. Next, we showed images of successfully fabricated devices and discussed how we experimentally characterized each antenna component. Finally, I demonstrated the

experimental validation of our antenna's mechanical resonance and the magnetic signal's transmission to a nearby probe.

In conclusion, this work has demonstrated a proof-of-concept miniaturized multiferroic antenna with a good piezoelectric resonance response and clear magnetic signal transmission near 400 MHz. Most importantly, this work will aid those students who aim to fabricate similar devices in the future by providing guidelines and discussing how to avoid common pitfalls.

Chapter 4. Conclusions and Outlook

Microdevices that utilize ferroic materials hold much promise in biomedical engineering and the medical industry. From miniaturized sensors and actuators to miniaturized communications devices, these devices are poised to replace many outdated technologies due to their inherent benefits, like biocompatible materials and miniaturization capabilities. The work presented in this dissertation has focused on the development and fabrication of two key technologies: A ferromagnetic single-cell capture and release platform and a 400MHz multiferroic antenna.

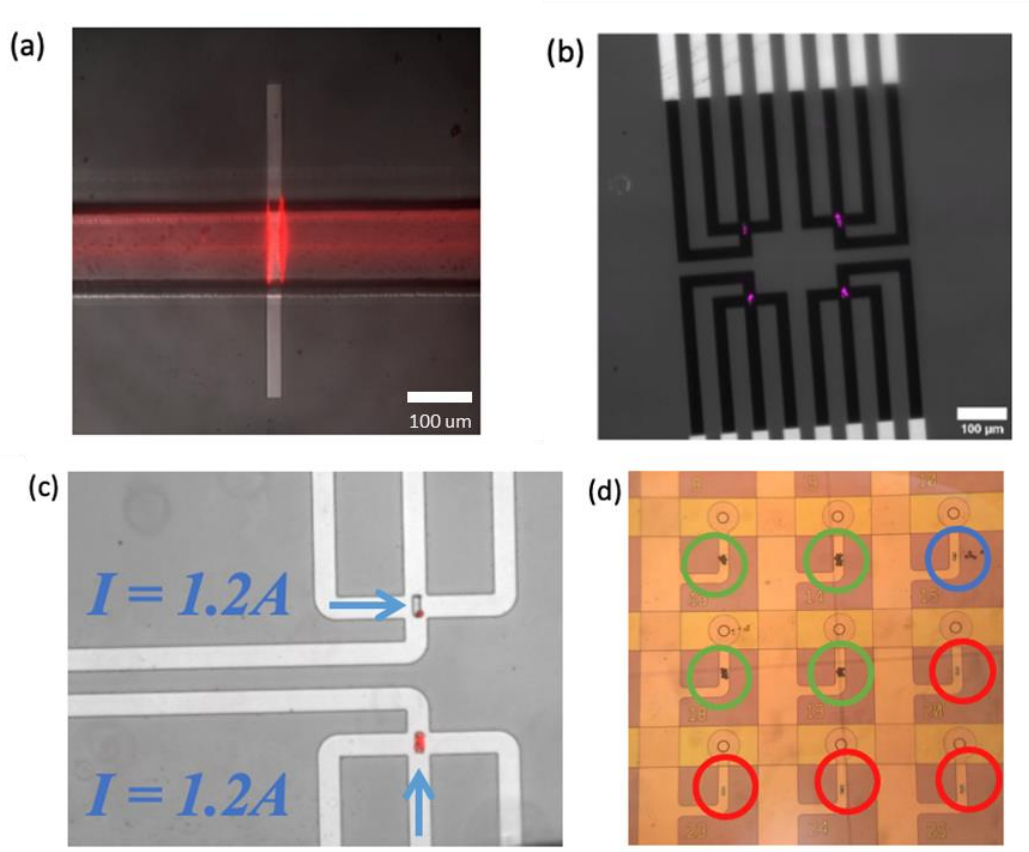

Figure 4-1 Different iterations of cell capture and release devices. (a) First generation device where we had a long nickel bar beneath a microfluidic channel and magnetized it in the short axis to observe bead capture at the poles (the left and right edges of the magnet). (b) Second generation device where the goal was to both miniaturize the capture site and implement a magnetic switching mechanism known as spin-orbit torque. (c) The third-generation device where the generation of

oersted fields replaced SOT to magnetize and demagnetize the device. (d) The fourth and final version of our platform, where the goal was to array these individually addressable capture sites.

The development of our single-cell capture and release platform presented in Chapter 2 required many iterations over the last five years. I first set out to design a platform that could achieve high-throughput magnetic single-cell capture and deterministic release in October 2018. The project began by placing a large nickel film within a microfluidic channel and observing how it would capture superparamagnetic beads. From there, we worked on miniaturizing the film to achieve single-cell capture. Next, we worked on different methods of magnetizing and demagnetizing the capture sites, and finally, we produced a working array of individually addressable capture sites. We went through many iterations, including many materials, geometries, switching methods, etc. Finally, through careful design and occasional trial and error, in June 2022, we successfully designed a device that could capture an array of single cells and deterministically release any desired cell for downstream applications. As described in chapter 2, our finalized platform is comprised of three main components: (1) a PDMS microfluidic channel to guide the flow of cells, (2) a 5x5 element array of thin (120 nm) 7 μm x 21 μm rectangular iron magnetic capture sites, and (3) a network of copper wires used to magnetize and demagnetize individual capture sites. Each component in this design is a product of the many iterations and modeling efforts conducted during the earlier stages of the project. Once this design was finalized, we modeled each component to verify that it could theoretically achieve the goals of single-cell capture and release. Upon completing these verifications, we built the device. First, we tested its ability to magnetize and demagnetize individual capture sites by measuring the magnetic states of the capture sites using MFM. Once we had successfully achieved magnetization and demagnetization of any capture site in the array, we attempted to capture and release superparamagnetic beads. This experiment was successful. We saw capture

at each of the 25 capture sites and were able to release the beads from each capture site one by one. Finally, we experimentally demonstrated the ability of this device to capture and release individual cells. These experiments were more difficult since they required us to first label the cells with superparamagnetic beads, which was a complex process. However, in the end, these experiments were also successful. We observed the magnetic capture of individual T cells at discrete capture sites, and upon the application of a demagnetizing current, we observed single-cell release. It took almost five years, but ultimately we achieved the goal we set for ourselves in 2018. There is still much work to be done if this device is ever to reach commercialization. The most critical challenge to overcome is drastically increasing the number of capture sites. Our device has 25 sites, but thousands of individually addressable capture sites are needed for industrial applications. The main challenge here is the wiring geometry required to deliver current to only specific capture sites. For this, a person familiar with integrated circuits or similar disciplines would be required. Additionally, an optimization of the capture site geometry is necessary to limit the number of captured cells to one per capture site. In the current design, the capture sites are too big, allowing enough surface area for multiple cells to be captured at one capture site. These are just some examples of improvements that are necessary if one desires to commercialize this platform. I believe this technology provides the user with a highly scalable and automatable platform for the capture and deterministic release of individual cells. I hope someone in the future can improve our design and use it for more impactful applications.

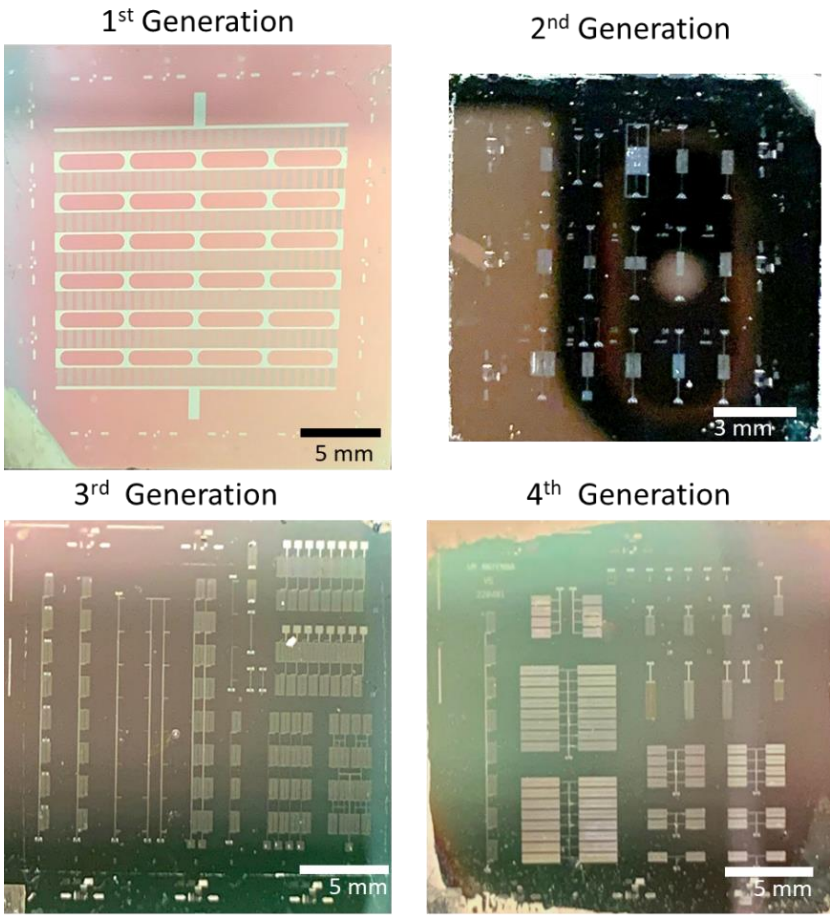

Figure 4-2 Different generations of our Multiferroic Antenna. The first generation was the antenna array design made by our predecessor Jinzhao Hu. The second generation was made to study the behavior of a single antenna element. The third generation was our first attempt at arraying these single antennas. Finally, the fourth generation is an attempt at both arraying and increasing the amount of magnetic volume per antenna array.

Developing our 400 MHz multiferroic antenna was also a long and arduous process. The development of this technology began in 2015 but failed for many years due to multiple issues, including fabrication, problems with vendors, poor modeling results, etc. I joined this project in 2019 upon the graduation of the member of my lab who had started the project. Even though he made many significant advances, my predecessor could not successfully fabricate his proposed design of a multiferroic antenna, and those antennas he did fabricate did not show any noticeable radiation. To address these issues, I was tasked with optimizing the multiferroic antenna

fabrication and finding ways to improve the design. Alongside my colleague Ruoda Zheng, who was tasked with making reliable FEM models to improve the antenna design, I set out to make this antenna work by the time I graduated. Over the next three years, the antenna design went through many iterations. We began with our predecessor's design but soon realized its shortcomings. Guided by Ruoda's modeling results and my fabrication optimization, we changed practically all the materials over the next few years and improved the antenna's design. Finally, in 2022 we ended up with the design discussed in chapter 3. This device is built upon a silicon substrate. Upon this substrate is deposited a continuous platinum bottom electrode film. Above this film is deposited a 1um film of piezoelectric AlN. Above the AlN, we have two sets of interdigitated bars. The first set is the top aluminum electrodes, used for inducing an electric field through the thickness of the AlN and causing it to deform. The other interdigitated bars are the magnetic bars between each pair of aluminum electrodes. These are placed here to experience the maximum amount of strain which in turn causes the maximum amount of magnetization change. This change in magnetization will result in an emitted electromagnetic field that can be sensed at a distance. To remove the clamping effects that the silicon substrate would have on the AlN film and thus maximize the strain it experienced, we also removed all of the silicon immediately beneath the antenna device. This resulted in a freestanding membrane supported at its edges. The performance of this design was carefully verified and optimized by my colleague Ruoda Zheng. Once the design was finalized, I optimized the fabrication process, the details of which are carefully outlined in Chapter 3. With a successfully fabricated multiferroic antenna, we proceeded to perform some material and device characterization to ensure that all of its components were working as expected. Once this was completed, the antenna was sent out to the University of Texas at Dallas, where our colleagues would test its

resonant behavior and its radiation performance. These tests were successful. We observed that the antenna was resonating at around 400 MHz, and at this frequency, the antenna would also radiate a detectable magnetic signal. After many years developing this antenna, we ultimately achieved what we set out to achieve, fabricating a resonant multiferroic antenna that emits a detectable magnetic signal. Although this was a significant success, there are still a lot of improvements that can be made if this technology is to be further developed. First, as seen in chapter 3, the emitted magnetic signal requires the magnetic sensor to be extremely close to our antenna. This is because our device does not emit a powerful signal since we have a minimal amount of magnetic material per antenna. To increase the signal, we must find a way of significantly increasing the magnetic volume per device. One way to do this, an approach we attempted but were unsuccessful in, is to connect multiple antennas in an array. This multiplies the amount of magnetic material by the number of antennas in the array. The difficulty with this approach is finding a good way of simultaneously inputting a signal to all of the antennas in the antenna array. Using wires between each antenna also adds resistive losses and impedance matching issues, which are very difficult to resolve. Second, the magnetic material we used was not perfect. FeGaB should theoretically perform much better than our material did. This was due to issues with the deposition system we used. However, if this material composition and magnetic properties can be optimized, this would significantly increase the radiation performance of our device. In addition to these two issues, other design and material improvements can be made. Finally, this device was designed to use in implantable devices, so further testing under more realistic conditions that match the environment within the body or other lossy media is needed.

In conclusion, we successfully designed/fabricated/tested a proof-of-concept high throughput magnetic single-cell capture and release device. In addition, we improved the design and fabrication process of a 400 MHz multiferroic antenna, showing favorable mechanical resonance response and electromagnetic radiation. Further work should be conducted to commercialize these products. Nevertheless, we have successfully set the foundation for two technologies that, if carefully developed, can revolutionize their respective industries. I hope future students can learn from the work presented in this dissertation and avoid the mistakes I experienced.

Chapter 5. References

[1] B. D. Cullity and C. D. Graham, *Introduction to Magnetic Materials*, Second Edition. Wiley, 2009.

[2] "Ferromagnetism." http://hyperphysics.phy-astr.gsu.edu/hbase/Solids/ferro.html (accessed Feb. 06, 2023).

[3] G. Zhao, X. Zhang, and F. Morvan, "Theory for the Coercivity and Its Mechanisms in Nanostructured Permanent Magnetic Materials," *Reviews in Nanoscience and Nanotechnology*, vol. 4, no. 1, pp. 1–25, May 2015, doi: 10.1166/RNN.2015.1063.

[4] J. E. Miltat and M. J. Donahue, "Numerical Micromagnetics: Finite Difference Methods," *Handbook of Magnetism and Advanced Magnetic Materials*, Dec. 2007, doi: 10.1002/9780470022184.HMM202.

[5] T. L. Gilbert, "A Lagrangian formulation of the gyromagnetic equation of the magnetization field," *Physical Review*, vol. 100, 1955.

[6] "Definition of magnetic resonance imaging - NCI Dictionary of Cancer Terms - NCI." https://www.cancer.gov/publications/dictionaries/cancer-terms/def/magnetic-resonance-imaging (accessed Feb. 06, 2023).

[7] O. M. Lemine, "Magnetic Hyperthermia Therapy Using Hybrid Magnetic Nanostructures," *Hybrid Nanostructures for Cancer Theranostics*, pp. 125–138, Jan. 2019, doi: 10.1016/B978-0-12-813906-6.00007-X.

[8] M. Mitolo and R. Araneo, “A Brief History of Electromagnetism [History],” *IEEE Industry Applications Magazine*, vol. 25, no. 2, pp. 7–11, Mar. 2019, doi: 10.1109/MIAS.2018.2884753.

[9] M. A. Riley, A. D. Walmsley, J. D. Speight, and I. R. Harris, “Magnets in medicine,” *Materials Science and Technology*, vol. 18, no. 1, pp. 1–12, 2002, doi: 10.1179/026708301125000140.

[10] D. D. Stueber, J. Villanova, I. Aponte, Z. Xiao, and V. L. Colvin, “Magnetic Nanoparticles in Biology and Medicine: Past, Present, and Future Trends,” *Pharmaceutics*, vol. 13, no. 7, p. 943, Jun. 2021, doi: 10.3390/pharmaceutics13070943.

[11] J. D.-D. development research and undefined 2006, “Magnetic nanoparticles for drug delivery,” *Wiley Online Library*, vol. 67, no. 1, pp. 55–60, Jan. 2006, doi: 10.1002/ddr.20067.

[12] G. S. P. Mok, B. M. W. Tsui, and F. J. Beekman, “Magnetic particle hyperthermia—a promising tumour therapy?,” *iopscience.iop.org*, vol. 25, p. 452001, 2014, doi: 10.1088/0957-4484/25/45/452001.

[13] V. v. Mody, A. Cox, S. Shah, A. Singh, W. Bevins, and H. Parihar, “Magnetic nanoparticle drug delivery systems for targeting tumor,” *Applied Nanoscience (Switzerland)*, vol. 4, no. 4, pp. 385–392, Apr. 2014, doi: 10.1007/S13204-013-0216-Y.

[14] M. Zborowski, J. J. Chalmers, and W. G. Lowrie, “Magnetic Cell Manipulation and Sorting,” pp. 15–55, 2017, doi: 10.1007/978-3-319-44139-9_2.

[15] D. Delmonte, “Combined magnetic, electric, ferroelectric and magnetoelectric characterization of novel multiferroic perovskites obtained by high pressure/temperature synthesis,” Universita degli studi di Parma, 2015.

[16] N. Setter *et al.*, “Ferroelectric thin films: Review of materials, properties, and applications,” *J Appl Phys*, vol. 100, no. 5, p. 051606, Sep. 2006, doi: 10.1063/1.2336999.

[17] S. M. Karga and G. Hao, “An Atlas of Piezoelectric Energy Harvesters in Oceanic Applications,” *Sensors 2022, Vol. 22, Page 1949*, vol. 22, no. 5, p. 1949, Mar. 2022, doi: 10.3390/S22051949.

[18] W. P. Mason, “Piezoelectricity, its history and applications,” *J Acoust Soc Am*, vol. 70, no. 6, p. 1561, Aug. 1998, doi: 10.1121/1.387221.

[19] M. S. Vijaya, “Piezoelectric Materials and Devices: Applications in Engineering and Medical ... - M. S. Vijaya - Google Books,” *Taylor & Francis Group*, 2013, Accessed: Feb. 07, 2023. [Online]. Available: https://books.google.com/books/about/Piezoelectric_Materials_and_Devices.html?id=TWC8Ow422hwC

[20] M. T. Chorsi *et al.*, “Piezoelectric Biomaterials for Sensors and Actuators,” *Advanced Materials*, vol. 31, no. 1, p. 1802084, Jan. 2019, doi: 10.1002/ADMA.201802084.

[21] Q. Zhou, K. H. Lam, H. Zheng, W. Qiu, and K. K. Shung, “Piezoelectric single crystals for ultrasonic transducers in biomedical applications,” *Prog Mater Sci*, vol. 66, p. 87, Oct. 2014, doi: 10.1016/J.PMATSCI.2014.06.001.

[22] B. Shi, Z. Li, Y. Fan, B. Shi, Y. Fan, and Z. Li, “Implantable Energy-Harvesting Devices,” *Advanced Materials*, vol. 30, no. 44, p. 1801511, Nov. 2018, doi: 10.1002/ADMA.201801511.

[23] Z. You, L. Wei, M. Zhang, F. Yang, and X. Wang, “Hermetic and Bioresorbable Packaging Materials for MEMS Implantable Pressure Sensors: A Review,” *IEEE Sens J*, vol. 22, no. 24, pp. 23633–23648, Dec. 2022, doi: 10.1109/JSEN.2022.3214337.

[24] Y. Honjol *et al.*, “Current view and prospect: Implantable pressure sensors for health and surgical care,” *Med Devices Sens*, vol. 3, no. 3, p. e10068, Jun. 2020, doi: 10.1002/MDS3.10068.

[25] W. M. Wilson and N. L. Cruden, “Advances in coronary stent technology: current expectations and new developments,” *Research Reports in Clinical Cardiology*, vol. 4, pp. 85–96, Jul. 2013, doi: 10.2147/RRCC.S34408.

[26] D. Stoeckel, “Nitinol medical devices and implants,” *http://dx.doi.org/10.3109/13645700009063054*, vol. 9, no. 2, pp. 81–88, 2009, doi: 10.3109/13645700009063054.

[27] D. Stoeckel, A. Pelton, and T. Duerig, “Self-expanding Nitinol stents: Material and design considerations,” *Eur Radiol*, vol. 14, no. 2, pp. 292–301, Feb. 2004, doi: 10.1007/S00330-003-2022-5/FIGURES/22.

[28] N. A. Spaldin and M. Fiebig, “The renaissance of magnetoelectric multiferroics,” *Science (1979)*, vol. 309, no. 5733, pp. 391–392, Jul. 2005, doi:

10.1126/SCIENCE.1113357/ASSET/C52584F2-8B9D-421C-913B-817AFB4A5FEA/ASSETS/GRAPHIC/391-2.GIF.

[29] C. Lu, M. Wu, L. Lin, and J. M. Liu, “Single-phase multiferroics: new materials, phenomena, and physics,” *Natl Sci Rev*, vol. 6, no. 4, pp. 653–668, Jul. 2019, doi: 10.1093/NSR/NWZ091.

[30] C. W. Nan, M. I. Bichurin, S. Dong, D. Viehland, and G. Srinivasan, “Multiferroic magnetoelectric composites: Historical perspective, status, and future directions,” *J Appl Phys*, vol. 103, no. 3, p. 031101, Feb. 2008, doi: 10.1063/1.2836410.

[31] H. Lin *et al.*, “NEMS magnetoelectric antennas for biomedical application,” *IMBioc 2018 - 2018 IEEE/MTT-S International Microwave Biomedical Conference*, pp. 13–15, Aug. 2018, doi: 10.1109/IMBIOC.2018.8428867.

[32] C. Tu *et al.*, “Mechanical-Resonance-Enhanced Thin-Film Magnetoelectric Heterostructures for Magnetometers, Mechanical Antennas, Tunable RF Inductors, and Filters,” *Materials 2019, Vol. 12, Page 2259*, vol. 12, no. 14, p. 2259, Jul. 2019, doi: 10.3390/MA12142259.

[33] C. Wang *et al.*, “Wide-band multiferroic quartz MEMS antennae,” *J Phys Conf Ser*, vol. 1407, no. 1, p. 012026, Nov. 2019, doi: 10.1088/1742-6596/1407/1/012026.

[34] R. Khojah *et al.*, “Single-Domain Multiferroic Array-Addressable Terfenol-D (SMArT) Micromagnets for Programmable Single-Cell Capture and Release,” *Advanced Materials*, vol. 33, no. 20, May 2021, doi: 10.1002/adma.202006651.

[35] C. Wyatt Shields Iv, C. D. Reyes, and G. P. López, “Microfluidic cell sorting: A review of the advances in the separation of cells from debulking to rare cell isolation,” *Lab on a Chip*, vol. 15, no. 5. Royal Society of Chemistry, pp. 1230–1249, Mar. 07, 2015. doi: 10.1039/c4lc01246a.

[36] D. Mattanovich and N. Borth, “Applications of cell sorting in biotechnology,” *Microbial Cell Factories*, vol. 5. Mar. 21, 2006. doi: 10.1186/1475-2859-5-12.

[37] W. A. Bonner, H. R. Hulett, R. G. Sweet, and L. A. Herzenberg, “Fluorescence activated cell sorting,” *Review of Scientific Instruments*, vol. 43, no. 3, pp. 404–409, 1972, doi: 10.1063/1.1685647.

[38] C. Wyatt Shields Iv, C. D. Reyes, and G. P. López, “Microfluidic cell sorting: A review of the advances in the separation of cells from debulking to rare cell isolation,” *Lab on a Chip*, vol. 15, no. 5. Royal Society of Chemistry, pp. 1230–1249, Mar. 07, 2015. doi: 10.1039/c4lc01246a.

[39] S. Miltenyi, W. Muller, W. Weichel, and A. Radbruch, “High Gradient Magnetic Cell Separation with MACS1,” Wiley-Liss, Inc, 1990.

[40] S. J. Altschuler and L. F. Wu, “Cellular Heterogeneity: Do Differences Make a Difference?,” *Cell*, vol. 141, no. 4. Elsevier B.V., pp. 559–563, 2010. doi: 10.1016/j.cell.2010.04.033.

[41] J. Zhao, “Cell Individuality: A Basic Multicellular Phenomenon and its Role in the Pathogenesis of Disease,” 1995.

[42] T. Luo, L. Fan, R. Zhu, and D. Sun, “Microfluidic single-cell manipulation and analysis: Methods and applications,” *Micromachines*, vol. 10, no. 2. MDPI AG, Feb. 01, 2019. doi: 10.3390/mi10020104.

[43] Y. Deng, Y. Guo, and B. Xu, “Recent development of microfluidic technology for cell trapping in single cell analysis: A review,” *Processes*, vol. 8, no. 10. MDPI AG, pp. 1–31, Oct. 01, 2020. doi: 10.3390/pr8101253.

[44] S. Lindström and H. Andersson-Svahn, “Overview of single-cell analyses: Microdevices and applications,” *Lab on a Chip*, vol. 10, no. 24. Royal Society of Chemistry, pp. 3363–3372, Dec. 21, 2010. doi: 10.1039/c0lc00150c.

[45] R. Wollman and N. Stuurman, “High throughput microscopy: From raw images to discoveries,” *J Cell Sci*, vol. 120, no. 21, pp. 3715–3722, Nov. 2007, doi: 10.1242/jcs.013623.

[46] J. R. Rettig and A. Folch, “Large-scale single-cell trapping and imaging using microwell arrays,” *Anal Chem*, vol. 77, no. 17, pp. 5628–5634, Sep. 2005, doi: 10.1021/ac0505977.

[47] D. K. Wood *et al.*, “Single cell trapping and DNA damage analysis using microwell arrays,” *Proceedings of the National Academy of Sciences (PNAS)*, vol. 107, no. 22, 2010, doi: 10.1073/pnas.1004056107/-/DCSupplemental.

[48] R. S. Kane, S. Takayama, E. Ostuni, D. E. Ingber, and G. M. Whitesides, “Patterning proteins and cells using soft lithography,” 1999.

[49] C. S. Chen, M. Mrksich, S. Huang, G. M. Whitesides, and D. E. Ingber, “Geometric Control of Cell Life and Death,” *Science (1979)*, vol. 276, no. 5317, May 1997, doi: 10.1126/science.276.5317.1425.

[50] X. Li, W. Chen, G. Liu, W. Lu, and J. Fu, “Continuous-flow microfluidic blood cell sorting for unprocessed whole blood using surface-micromachined microfiltration membranes,” *Lab Chip*, vol. 14, no. 14, pp. 2565–2575, Jul. 2014, doi: 10.1039/c4lc00350k.

[51] A. Dalili, E. Samiei, and M. Hoorfar, “A review of sorting, separation and isolation of cells and microbeads for biomedical applications: microfluidic approaches,” *Analyst*, vol. 144, no. 1. Royal Society of Chemistry, pp. 87–113, Jan. 07, 2019. doi: 10.1039/c8an01061g.

[52] H. M. Ji, V. Samper, Y. Chen, C. K. Heng, T. M. Lim, and L. Yobas, “Silicon-based microfilters for whole blood cell separation,” *Biomed Microdevices*, vol. 10, no. 2, pp. 251–257, Apr. 2008, doi: 10.1007/s10544-007-9131-x.

[53] H. Lange, P. Taillandier, and J. P. Riba, “Effect of high shear stress on microbial viability,” *Journal of Chemical Technology and Biotechnology*, vol. 76, no. 5, pp. 501–505, May 2001, doi: 10.1002/jctb.401.

[54] V. Narayanamurthy, S. Nagarajan, A. Y. Firus Khan, F. Samsuri, and T. M. Sridhar, “Microfluidic hydrodynamic trapping for single cell analysis: Mechanisms, methods and applications,” *Analytical Methods*, vol. 9, no. 25. Royal Society of Chemistry, pp. 3751–3772, Jul. 07, 2017. doi: 10.1039/c7ay00656j.

[55] D. di Carlo, L. Y. Wu, and L. P. Lee, “Dynamic single cell culture array,” *Lab Chip*, vol. 6, no. 11, pp. 1445–1449, 2006, doi: 10.1039/b605937f.

[56] A. M. Skelley, O. Kirak, H. Suh, R. Jaenisch, and J. Voldman, “Microfluidic control of cell pairing and fusion,” *Nat Methods*, vol. 6, no. 2, pp. 147–152, 2009, doi: 10.1038/nmeth.1290.

[57] D. Hümmer, F. Kurth, N. Naredi-Rainer, and P. S. Dittrich, “Single cells in confined volumes: microchambers and microdroplets,” *Lab on a Chip*, vol. 16, no. 3. Royal Society of Chemistry, pp. 447–458, Feb. 07, 2016. doi: 10.1039/c5lc01314c.

[58] J. Clausell-Tormos *et al.*, “Droplet-Based Microfluidic Platforms for the Encapsulation and Screening of Mammalian Cells and Multicellular Organisms,” *Chem Biol*, vol. 15, no. 5, pp. 427–437, May 2008, doi: 10.1016/j.chembiol.2008.04.004.

[59] A. Huebner, S. Sharma, M. Srisa-Art, F. Hollfelder, J. B. Edel, and A. J. DeMello, “Microdroplets: A sea of applications?,” *Lab on a Chip*, vol. 8, no. 8. Royal Society of Chemistry, pp. 1244–1254, 2008. doi: 10.1039/b806405a.

[60] T. Luo, L. Fan, R. Zhu, and D. Sun, “Microfluidic single-cell manipulation and analysis: Methods and applications,” *Micromachines*, vol. 10, no. 2. MDPI AG, Feb. 01, 2019. doi: 10.3390/mi10020104.

[61] A. Ashkin, “Acceleration and Trapping of Particles by Radiation Pressure,” *Phys Rev Lett*, vol. 24, no. 4, 1970.

[62] H. Zhang and K. K. Liu, “Optical tweezers for single cells,” *Journal of the Royal Society Interface*, vol. 5, no. 24. Royal Society, pp. 671–690, Jul. 06, 2008. doi: 10.1098/rsif.2008.0052.

[63] T. A. Nieminen, N. du Preez-Wilkinson, A. B. Stilgoe, V. L. Y. Loke, A. A. M. Bui, and H. Rubinsztein-Dunlop, “Optical tweezers: Theory and modelling,” *J Quant Spectrosc Radiat Transf*, vol. 146, pp. 59–80, 2014, doi: 10.1016/j.jqsrt.2014.04.003.

[64] C. T. Lim, M. Dao, S. Suresh, C. H. Sow, and K. T. Chew, “Large deformation of living cells using laser traps,” *Acta Mater*, vol. 52, no. 7, pp. 1837–1845, Apr. 2004, doi: 10.1016/j.actamat.2003.12.028.

[65] A. Keloth, O. Anderson, D. Risbridger, and L. Paterson, “Single cell isolation using optical tweezers,” *Micromachines (Basel)*, vol. 9, no. 9, 2018, doi: 10.3390/mi9090434.

[66] A. J. Dickinson, P. M. Armistead, and N. L. Allbritton, “Automated capillary electrophoresis system for fast single-cell analysis,” *Anal Chem*, vol. 85, no. 9, pp. 4797–4804, May 2013, doi: 10.1021/ac4005887.

[67] Y. Sun, C. S. Lim, A. Q. Liu, T. C. Ayi, and P. H. Yap, “Design, simulation and experiment of electroosmotic microfluidic chip for cell sorting,” *Sens Actuators A Phys*, vol. 133, no. 2 SPEC. ISS., pp. 340–348, Feb. 2007, doi: 10.1016/j.sna.2006.06.047.

[68] T. Z. Jubery, S. K. Srivastava, and P. Dutta, “Dielectrophoretic separation of bioparticles in microdevices: A review,” *Electrophoresis*, vol. 35, no. 5. Wiley-VCH Verlag, pp. 691–713, 2014. doi: 10.1002/elps.201300424.

[69] B. M. Taff and J. Voldman, “A scalable addressable positive-dielectrophoretic cell-sorting array,” *Anal Chem*, vol. 77, no. 24, pp. 7976–7983, Dec. 2005, doi: 10.1021/ac0513616.

[70] M. P. Hughes, “Fifty years of dielectrophoretic cell separation technology,” *Biomicrofluidics*, vol. 10, no. 3, May 2016, doi: 10.1063/1.4954841.

[71] G. Pucihar, T. Kotnik, M. Kandušer, and D. Miklavčič, “The influence of medium conductivity on electropermeabilization and survival of cells in vitro,” *Bioelectrochemistry*, vol. 54, no. 2, pp. 107–115, 2001, doi: 10.1016/S1567-5394(01)00117-7.

[72] P. Y. Chiou, A. T. Ohta, and M. C. Wu, “Massively parallel manipulation of single cells and microparticles using optical images,” *Nature*, vol. 436, no. 7049, pp. 370–372, Jul. 2005, doi: 10.1038/nature03831.

[73] A. Ozcelik and T. J. Huang, “Acoustic Tweezers for Single-Cell Manipulation,” in *Handbook of Single-Cell Technologies*, Springer Singapore, 2022, pp. 1051–1077. doi: 10.1007/978-981-10-8953-4_40.

[74] X. Ding *et al.*, “Cell separation using tilted-angle standing surface acoustic waves,” *Proc Natl Acad Sci U S A*, vol. 111, no. 36, pp. 12992–12997, 2014, doi: 10.1073/pnas.1413325111.

[75] F. Guo *et al.*, “Three-dimensional manipulation of single cells using surface acoustic waves,” *Proc Natl Acad Sci U S A*, vol. 113, no. 6, pp. 1522–1527, Feb. 2016, doi: 10.1073/pnas.1524813113.

[76] A. Thiel, A. Scheffold, and A. Radbruch, “Immunomagnetic cell sorting-pushing the limits,” 1998.

[77] S. Miltenyi, W. Muller, W. Weichel, and A. Radbruch, “High Gradient Magnetic Cell Separation With MACS,” Wiley-Liss, Inc, 1990.

[78] M. A. M. Gijs, “Magnetic bead handling on-chip: New opportunities for analytical applications,” *Microfluidics and Nanofluidics*, vol. 1, no. 1. pp. 22–40, Nov. 2004. doi: 10.1007/s10404-004-0010-y.

[79] Y. Y. Huang *et al.*, “Screening and Molecular Analysis of Single Circulating Tumor Cells Using Micromagnet Array,” *Sci Rep*, vol. 5, Nov. 2015, doi: 10.1038/srep16047.

[80] L. Wu *et al.*, “Beyond Capture: Circulating Tumor Cell Release and Single-Cell Analysis,” *Small Methods*, vol. 3, no. 5. John Wiley and Sons Inc., May 01, 2019. doi: 10.1002/smtd.201800544.

[81] S. Rafiq, C. S. Hackett, and R. J. Brentjens, “Engineering strategies to overcome the current roadblocks in CAR T cell therapy,” *Nature Reviews Clinical Oncology*, vol. 17, no. 3. Nature Research, pp. 147–167, Mar. 01, 2020. doi: 10.1038/s41571-019-0297-y.

[82] H. Chai, Y. Feng, F. Liang, and W. Wang, “A microfluidic device enabling deterministic single cell trapping and release,” *Lab Chip*, vol. 21, no. 13, pp. 2486–2494, Jul. 2021, doi: 10.1039/d1lc00302j.

[83] S. G. Parker *et al.*, “A photoelectrochemical platform for the capture and release of rare single cells,” *Nat Commun*, vol. 9, no. 1, Dec. 2018, doi: 10.1038/s41467-018-04701-y.

[84] E. Reátegui *et al.*, “Tunable nanostructured coating for the capture and selective release of viable circulating tumor cells,” *Advanced Materials*, vol. 27, no. 9, pp. 1593–1599, Mar. 2015, doi: 10.1002/adma.201404677.

[85] B. M. Taff and J. Voldman, “A scalable addressable positive-dielectrophoretic cell-sorting array,” *Anal Chem*, vol. 77, no. 24, pp. 7976–7983, Dec. 2005, doi: 10.1021/ac0513616.

[86] M. Du, D. Kavanagh, Z. Zhang, and N. Kalia, “Designing Microfluidic Devices to Sort Haematopoietic Stem Cells Based on Their Mechanical Properties,” *Stem Cells Int*, vol. 2019, 2019, doi: 10.1155/2019/8540706.

[87] M. Soliman *et al.*, “Review on Medical Implantable Antenna Technology and Imminent Research Challenges,” 2021, doi: 10.3390/s21093163.

[88] F. Martin, P. Muralt, M.-A. Dubois, and A. Pezous, “ Thickness dependence of the properties of highly c -axis textured AlN thin films ,” *Journal of Vacuum Science & Technology A: Vacuum, Surfaces, and Films*, vol. 22, no. 2, pp. 361–365, Mar. 2004, doi: 10.1116/1.1649343.